Solar Powered Membrane Distillation For Seawater Desalination

by

Amanda Jane Hughes

A thesis submitted in fulfilment of the requirements
for the degree of Doctor of Philosophy
to
Heriot Watt University

April, 2015

Abstract

This thesis presents an investigation into the performance of a Membrane Distillation (MD) system used for seawater desalination. The research is focused on the effects of intermittent use of the MD module when powered with a solar energy collector. The aim is to assess the feasibility of directly powering an MD unit with a fluctuating input from a solar collector.

An investigation into the effect of temperature on the microstructure of the membrane was carried out. In a series of experiments, samples of PTFE membrane were imaged while heated from 17°C to temperatures between 60°C and 80°C. It was found that the membrane pore size increased with increases in temperature. When heated to 80°C the pore diameter increased by 44%.

Intermittent use of the system would cause the temperature of the MD module to fluctuate, therefore altering the membrane microstructure. An investigation was carried out to determine the influence of intermittent MD operation on the flux and conductivity of the distillate. The system was tested after overnight shutdown periods and was also tested with short term 'on/off' periods of between 5 and 20 minutes, simulating the intermittent output from a concentrated solar collector.

It was found that as the module was heated, the distillate flux produced increased, while the distillate conductivity decreased. Conversely, when the module cooled, the flux decreased and the quality of the distillate worsened. This was the result of the dependancy of membrane pore size on temperature.

Acknowledgements

I wish to extend my gratitude to Professor Tapas Mallick, for making this PhD possible and for contributing many great ideas along the way. Special thanks to my supervisor Dr Tadhg O'Donovan for invaluable guidance and support throughout the project. Your influence is undeniable, I am now a complete perfectionist who will always 'start with the numbers'.

I am also incredibly grateful for the help I received from the mechanical workshop technicians, particularly Richard Kinsella and Ian Harrower. Your wealth of knowledge and experience are the greatest resource the department has.

I would like to thank my colleagues and friends for all of the advice dispensed during coffee breaks over the years. I would like to give special thanks to Jonny Morton, Gurdrun Kocher, Nabin Sarmah, Sean Macdougall, Dorothy Hardy, Artur Ulrich, Dan Rylatt, Dalila Capao, Marius Dewar, Ourania Dimou, Gregor Sneddon and Alan Faulkner-Jones. It is thanks to you that I have thoroughly enjoyed my time spent at Heriot Watt.

My heartfelt thanks go to my wonderful boyfriend, Neil, for putting up with me during the dreaded writting-up stage, and for always making me laugh. Your love and support means the world to me.

Lastly, but by no means least, I would like to give extra special thanks to my amazing family for all of their support. To my Mum and Dad, I could not possibly have gotten through this challenging process without you. You are the best parents anyone could wish for.

Contents

List of Figures

List of Tables

Nomenclature

Symbol	Description	Units
A_a	Area of concentrator aperture	m^2
A_m	Area of membrane	m^2
A_p	Total are of pores	m^2
A_r	Area of concentrator receiver	m^2
c	Speed of light	m/s
C_r	Concentration ratio	$-$
C_p	Specific heat capacity	J/kgK
d_p	Equivalent pore diameter	μm
D_{flow}	Distillate flow rate	l/hr
D_{flux}	Distillate flux	l/m^2hr
E	Photon energy	eV
EC	Electrical conductivity	$\mu S/cm$
f_{dist}	Distillate output	kg
G	Conductance	S
h	Heat transfer coefficient	W/m^2K
hc	Planck's constant	$eV.s$
k_c	Cell constant of conductivity probe	cm
k_{vapour}	Thermal conductivity of vapour	W/mK
$k_{membrane}$	Thermal conductivity of membrane material	W/mK

L	Latent heat of vaporisation	kg/mol
L_o	Length of membrane sample	μm
$\dot{m}$	Mass flow rate	kg/s
M	Molecular weight of vapour	kg/mol
N_{vap}	Molecular flux of water vapour	$-$
P	Pressure	atm
Q	Heat flux	W/m^2
R	Universal gas constant	$m^3Pa/mol.K$
r_p	Average pore radius	m
r_{max}	Maximum pore radius	m
T	Temperature	°C
V	Volume	m^3
v	Velocity	m/s

Greek

symbol	**Description**	**Units**
α	Linear thermal expansion coefficient	K^{-1}
γ	Surface tension	N/m
$\delta_{membrane}$	Thickness of the membrane	m
δ_{airgap}	Thickness of the airgap	m
δ_{film}	Thickness of the film	m
η	Efficiency	%
θ	Angle	°
λ	Wavelength	m
μ	Viscosity	kg/ms
ρ	Density	kg/m^3
τ	Tortuosity of the membrane	$-$
ϕ	Porosity of the membrane	$-$

Symbol	Description
$cold, in$	Inlet of the cold channel of MD unit
$cold, out$	outlet of the cold channel of MD unit
hot, in	Inlet of the hot channel of MD unit
hot, out	outlet if the hot channel of MD unit

Chapter 1

Introduction

This thesis presents an investigation into the effects intermittent operation of Membrane Distillation (MD) when combined with a solar energy system to produce a single, standalone system, for use in decentralised locations. The solar energy system in question is a Concentrated Photovoltaic/Thermal collector (CPV/T). The output from a CPV/T system would fluctuate throughout the day and the system would only operate during daylight hours. It would therefore experience both short term and long term intermittent operation.

A CPV/T system would consist of a parabolic dish concentrator with 2-axis tracking and a combined photovoltaic and thermal receiver, which is placed at the focal point of the dish to collect solar radiation. A proportion of the solar energy spectrum is

absorbed by the PV cells and converted into electrical current. The remainder of the spectrum is converted into heat energy in the cells, which is extracted by the thermal collector placed directly beneath, making it a highly efficient system. This system is ideal for use with an MD unit as the electricity can be used to power the pumps required, while the thermal energy collected can be harnessed to heat the feed solution to the desired temperature for desalination - thus creating a single standalone system that can run autonomously.

1.1 Motivation

The need for safe and reliable water treatments systems in remote locations is considerable. It is estimated that 750 million people around the world lack access to safe water; this amounts to approximately one in nine people. [1]. The World Health Organisation (WHO) estimates that almost a billion people worldwide do not have access to an improved water source, putting them at risk of contracting water born diseases or coming into contact with chemical contaminants. Examples of improved water sources, as defined by WHO, include household connections, public standpipes and protected wells. However, even these sources of water can still pose a risk [2]. In India, for example, groundwater from 60% of the land has salinity levels above the taste threshold ($> 500mg/l$); 11% of the land has groundwater salinity of above 1920mg/l which is deemed unfit for consumption [3, 4]. In the early 2000's, areas such as West Bengal and Bangladesh reported a pandemic of heavy metal poisoning due to arsenic contaminants in the groundwater [5]. The result is that in many places, protected groundwater no longer provides a safe drinking source. The majority of those without access to protected water sources are those living in remote communities. Therefore, there is a pressing need to provide safe drinking water, be that from seawater or groundwater sources, on site at a village level.

Often those living in remote communities or deprived areas of developing countries do not have access to grid electricity. The use of renewable energy, therefore, has

become a popular choice when powering a water purification system in remote areas. Solar energy systems are of particular interest, given that solar resources are often abundant in arid areas where water shortage is most prevalent.

1.2 Background

The majority of research into solar powered water purification systems for remote applications has centred around the combination of Photovoltaics (PV) and Reverse Osmosis (RO) and this technology is now commercially available [6, 7]. However, in recent years interest in MD has increased rapidly, due in part to better membrane fabrication techniques and improved flux [8]. Manufacturers are now able to make thinner membranes, with a thickness as low as 50 μm and higher porosity values, of up to 80%, are achievable. Both of these developments lead to a significant improvement in the distillate flux produced during the MD process [9]. As a result several manufacturers began to explore the commercial value of MD membranes, including Gore and Associates [10]. The popularity of MD technology has also grown steadily amongst academic researchers, as reflected in the increased number of MD publications [8].

Winter el al [11] detailed the design and construction of full scale spiral wound membrane distillation modules with a total membrane surface area of 5 - 14 m^2. These modules were capable of producing distillate flow rates of up to 25 l/h, with conductivity consistently below 3.5 μS/cm throughout all experiments, even with feed conductivity of up to 120, 000 μS/cm. In 2010 and 2011, three autonomous solar and waste heat powered MD plants were developed by Fraunhofer ISE, each of which was designed to produce 5000 l/day of distillate when operated with an inlet feed temperature of 80°C and feed flow rate of 4800 l/h. Schwantes et al [12] detail the performance of these plants. Each plant contains thermal storage and a control system that buffers the temperature fluctuations from the solar source, to provide a constant feed inlet temperature to the MD module. Extra heat accumulated in storage over the course of

the day is then used to extend the hours of operation into the evening, once the sun has set. However even with storage and control systems in place, the system must be shut down for a period over night allowing the module to cool.

Several research groups have reported high distillate conductivity immediately after the system started up, the conductivity then rapidly decreased during the first hour of operation [11, 13, 14]. When testing a small single loop solar MD system, Banat el al [13] reported an initial distillate conductivity of 1000 μS/cm, which then rapidly decreased to 40 μS/cm within one hour. Though this phenomenon is well documented amongst MD researchers, to date the effects of intermittent use of MD modules have not been fully characterised, nor has their cause been explained.

1.3 Research objectives

This thesis investigates the effect of temperature on the structure of the membranes used in MD, and consequently the effect of temperature on a membrane distillation system when operated intermittently. Of particular interest in this study was the intermittent operation of an MD system when directly coupled with a CPV/T energy system.

An analysis of the microstructure of hydrophobic membranes used in the MD process was carried out at room temperature, with the use of a Scanning Electron Microscope (SEM). The images were analysed and characteristics such as membrane porosity were determined. The samples were heated inside of the SEM chamber and images were taken over a 80 minute period. The aim of these experiments was to assess the changes in the membrane's microstructure when heated and determine the rate at which the material changed.

A small lab scale MD unit was designed and build at Heriot Watt University. A series of experiments were carried out to determine the steady state performance of the unit. Experiments were then conducted to establish how the changes in microstructure of the membrane when heated would effect the performance of an MD system. Firstly,

long term intermittency was investigated and the effect of leaving the system off overnight was explored. The system was operated with constant input parameters such as feed temperature and feed flow, while distillate flux and conductivity produced from the module were observed during the first 1.5 hours of operation. The experiment was repeated several times with different feed temperatures, ranging from 60 - 80°C. By altering the feed temperature used in each experiment, it was possible to investigate the effect of heating the module at different rates.

The lab scale MD unit was tested with fluctuating feed temperature, similar to that expected from a CPV/T Energy system. The energy input from a CPV/T system is expected to have ′on/off′ characteristics. This fluctuating feed temperature was simulated with the use of a heated water bath. The temperature of the feed solution entering the hot channel was cycled between 80°C and ambient temperature for intervals of between 5 and 20 minutes. Therefore, the effects of short term intermittent operation of the MD module were investigated, with the aim of determining if an MD system could be directly coupled with a CPV/T energy collector.

Chapter 2

Solar powered membrane distillation

Water is one of the most abundant substances on earth, yet most of this resource is inaccessible or unfit for drinking. The sea holds 97% of the worlds total water supply; this seawater has high salt content in the range of 10,000ppm-45,000ppm, far greater than safe levels for consumption. The majority of the remaining 2.5% is frozen water found in glaciers, with just 0.5% of the earths water is found in lakes, rivers and aquifers, [15].

This fresh water is no longer sufficient to meet our needs. The demand for safe drinking water is greater than ever, as the world experiences a rapid increase in

population and developing countries continue to push towards industrialisation. By the turn of the 21st century, fresh water shortages had become an international crisis. In 2008, the United Nations put forward a report outlining its Millennium Development Goals. One of their targets was to halve the number of people living without sustainable access to safe drinking water [16]. This target was met in 2010, however their most recent publication estimates that over 748 million people do not have access to improved drinking water [1]. Figure 2.1 [1] shows the percentage of the population who have access to improved drinking water in 2012.

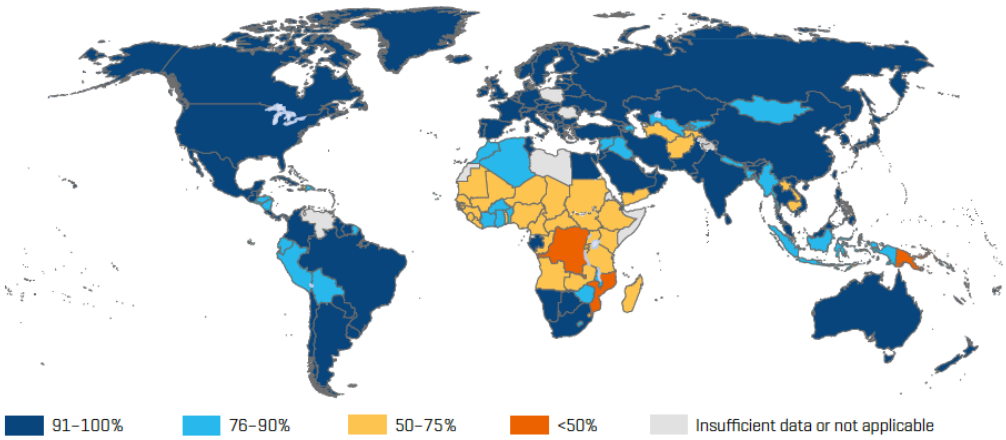

Figure 2.1: Percentage of the population with access to improved water

The majority of those without access to safe drinking water are living in rural communities. This presents a major logistical problem, as those living in rural areas often do not have access to electricity, making it difficult to find the energy required to purify water. It is clear that there is a great need for water treatment systems that can be deployed in remote locations. Solar powered MD systems are well suited to this application. The advantages of this technology are discussed in the following chapter. The progress made and the challenges encountered in this area of research are also discussed.

2.1 Membrane distillation

Desalination technology can be divided into two categories, thermal and membrane desalination. A thermal process known as Multistage Flash, (MSF), accounts for over 60% of all desalination worldwide [17]. An overview of some desalination processes are shown in figure 2.2. Multiple-Effect Distillation, (MED), and solar stills are also commonly used thermal desalination processes.

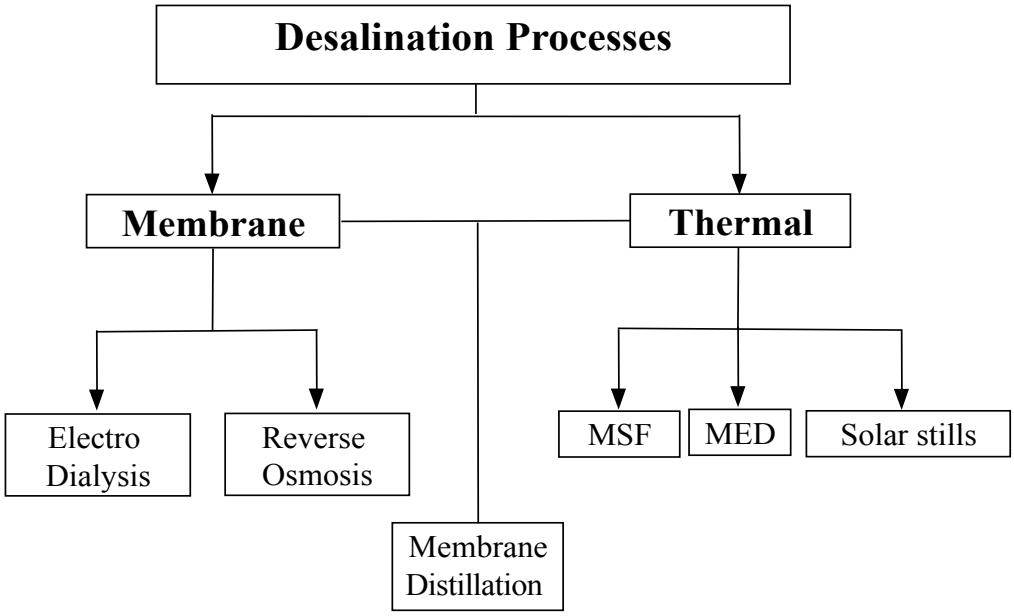

Figure 2.2: Desalination technology overview

Reverse osmosis and electro dialysis are common desalination processes that incorporate a membrane. Membrane distillation, however, is a combination of thermal distillation and membrane technology. The feed solution is heated to create vapour, as in all thermal desalination processes, however the an MD module also incorporates hydrophobic membrane which acts a barrier between saline liquid and pure water vapour. MD is a promising technology, however it is still in the research and development phase.

2.1.1 The MD process

Membrane distillation is a thermally driven desalination process were only vapour molecules are transported through the pores of a hydrophobic membrane. The membrane acts as a barrier to the saline solution, resulting in a liquid-vapour interface at the entrance of each pore [9]. Pure water vapour can pass through the pores and is condensed on the other side [8]. The driving force for vapour diffusion in membrane distillation is the pressure difference across the membrane interfaces.

There are advantages to the MD process when compared with conventional membrane technology such as Reverse Osmosis (RO). Firstly, theoretically MD is capably of 100% rejection of ions, macromolecules and non-volatile substances. Though in practice this is difficult to achieve, MD researchers have demonstrated much higher levels of ionic rejection than has been seen from RO, Micro-filtration (MF) and Ultrafiltration (UF) [9].

MD can be operated at atmospheric pressure, as it is a thermally driven process. This results in lower equipment and operating costs when compared to RO and other high pressure driven membrane processes, as a smaller pump with lower energy requirements can be used. The lower operating pressure also means that there is less mechanical stress on the membranes.

Another advantage of MD is the minimal role the membrane will play in the separation process compared with RO, UF and MF. The membrane acts as barrier for the vapour-liquid interface, it does not chemically distinguish between the components in the solution nor does it act like a sieve. This increases the choice of membrane materials available, the most commonly chosen are often highly resistance to chemicals and which have relatively large pore sizes to reduce fouling.

An advantage of MD, as with all membrane technology, when compared with thermal distillation processes is reduced plant size. Conventional distillation requires a large vapour space, where as membrane modules can have a spiral wound or hollow tube confirmation, which reduces their size [9].

MD requires relatively low temperatures, typically within the range of 60°C - 80°C, although temperatures as low as 30°C have been proven to work. This allows MD technology to be effectively combined with low grade, waste or alternative energy sources such as solar collectors [18]. Small scale MD systems powered by solar energy have been developed and tested. These systems have proven that the combined technology can be competitive with reverse osmosis, when applied in remote areas [19].

However, MD has encountered problems that have hindered its progress and prevented it from being implemented commercially. The main issue is low permeate flux produced by the MD process when compared to membrane technologies like RO [8].

Other issues include membrane wetting, preventing the high retention rates expected from the process. It is essential to the separation process that the membrane does not become wet and only vapour and non-condensable gases enter the pores. Materials such as polypropylene (PP), polyethylene (PE), polytetrafluoroethylene (PTFE), and polyvinylidene fluoride (PVDF) are commonly used, as these materials have high surface energies [20]. However 100% retention of salts has not been experimentally achieved. Winter el al [11] demonstrated a high retention of up to 99.997% in lab conditions, in the field however the modules commonly experience problems with leakages, which lower the salt retention to around 97%.

2.1.2 Mass transfer

A liquid vapour interface is formed on the surface of the membrane. The vapour pressure gradient across the membrane is the driving force for mass transfer through the pores. This process of convection and diffusion through the pores is described by a combination of Knudsen diffusion and Poiseuille flow [18]. The total flux through the membrane is expressed as:

$$N_{membrane} = \frac{1}{RT_{ave,membrane}} \left(\frac{1}{D_{kn}} + \frac{1}{D_{st}} \right)^{-1} \frac{\Delta P_{membrane}}{\delta_{membrane}} \tag{2.1}$$

Where $T_{ave,membrane}$ is the average temperature between both sides of the membrane, $\Delta P_{membrane}$ is the vapour pressure difference between both sides of the membrane and D_{kn} is the coefficient of Knudsen diffusion, expressed as [21]:

$$D_{kn} = \frac{2\phi r_p}{3\tau} \left(\frac{8RT_{ave,membrane}}{\pi M} \right)^{\frac{1}{2}} . \tag{2.2}$$

Where r_p is the average pore radius, ϕ is the porosity of the membrane, τ is the tortuosity of the membrane pores. M is the molecular weight of vapour.

D_{st} is the diffusion coefficient of the stagnant air in the pores, expressed as:

$$D_{st} = \frac{D\phi P}{\tau P_{ln}} , \tag{2.3}$$

where D is the diffusion coefficient for vapour in air and P_{ln} is the logarithmic mean of the partial air pressure on either side of the membrane .

Energy must be supplied for the phase change to occur, changing the liquid into a vapour. Only these vapour molecules are then able to pass through the hydrophobic membrane. The high surface tension of the polymeric membrane prevents water molecules from entering the pores. A liquid/vapour interface is formed at the entrance of the membrane pores, this creates a trans-membrane vapour pressure difference which it the driving force behind membrane distillation. In this way the membrane is used to separate the pure distillate from the retained concentrate solution.

2.1.3 Heat transfer

Heat transfer across the membrane is governed by two main mechanisms, conduction through the membrane material and vapour within the pores and the transport of latent heat with the vapour flux N_{vap} [8]. The heat flux across the membrane is given as [22]:

$$Q_{membrane} = N_{vap}L + h_{membrane}(T_{hot,mem} - T_{mem,air}) \ , \tag{2.4}$$

where N_{vap} is the vapour flux, L is the latent heat of vaporisation, and $h_{membrane}$ is the heat transfer coefficient of the membrane. The heat transfer coefficient of the membrane, $h_{membrane}$, can be calculated by considering conduction through both the membrane material and the air within the pores of the membrane. This is expressed as:

$$h_{membrane} = \frac{(\phi k_{vapour}) + ((1-\epsilon)k_{membrane})}{\delta_{membrane}} \ , \tag{2.5}$$

where ϕ is the porosity of the membrane, $\delta_{membrane}$ is the thickness of the membrane, k_{vapour} is the thermal conductivity of the vapour and $k_{membrane}$ is the thermal conductivity of the membrane.

2.1.4 Parameters affecting the MD process

There are several operating parameters that can have a significant effect on the performance of an MD system. The temperature, flow rate and concentration of the feed solution are the predominant factors that must be taken into account. The relationship between feed temperature and distillate flux is well established. There is an exponential increase in distillate flux with increase in feed temperature [23, 11].

An increase in the feed flow rate results in the higher values of distillate flux, the relationship between the two is linear. Increased feed velocity and feed stirring rate will lead to an increase in the heat transfer coefficient on the feed side of the membrane. Thus reducing the temperature and concentration polarisation effects [24]. Both temperature and concentration polarisation decrease the distillate flux, therefore reducing these boundary layers is beneficial to the flux.

Another of the main advantages of MD is its capability to treat feed solutions

with high concentration. Other membrane processes, particularly those that are pressure driven such as RO, can suffer significant decrease in distillate flux at high feed concentration. MD on the other hand, can be used to desalinate seawater with high salt concentrations while still maintain high flux. This has been demonstrated in various MD publications [9, 11, 25, 26].

The structure of the membranes used in the process also play a significant role in the performance of the system. The vapour flux through the membrane during the MD process is largely dependant of factors such as pore size, membrane thickness and tortuosity of the pores (a factor describing the curvature along the path length of the pore). The molar flux through a pore is defined as [9];

$$N_{vap} \propto \frac{r^a \epsilon}{\delta_m \tau} \ , \tag{2.6}$$

where N is the molar flux of water vapour, and r is the mean pore size, the factor a is equal to 1 or 2 for Knudsen diffusion or viscous flow, respectively. δ_m is the membrane thickness, τ is the membrane tortuosity and ϵ is the membrane porosity. Therefore, higher porosity and greater pore size will lead to an increase in diffusion across the pore.

However, when selecting the optimum pore size it is also important to consider that the pores are small enough to prevent liquid from entering them, this is a phenomenon known as membrane wetting. The Liquid Entry Pressure, (LEP) of a pore is defined as [9]:

$$LEP = \frac{-2B\gamma Cos(\theta)}{r_{max}} \ , \tag{2.7}$$

where γ is the surface tension of the liquid, θ is the contact angle between the liquid and the membrane surface and r_{max} is the maximum pore radius in the membrane, this is the pore most likely for liquid to enter. B is a geometric factor that is determined by the pores structure. Therefore, the greater the pore size the lower the LEP value.

2.1.5 Membrane configurations

There are several configurations for a membrane distillation system; the concentrated water on the feed side is always in direct contact with the membrane as this is essential to establish the vapour pressure difference. However there are different configurations for the permeate side, as shown in figure 2.3.

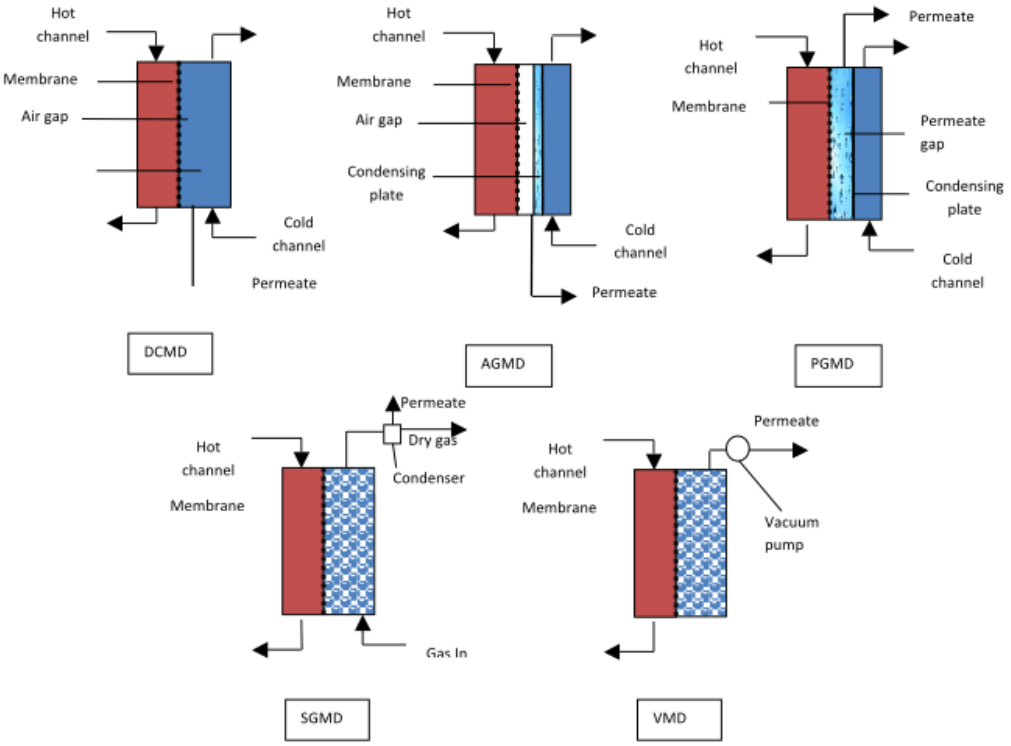

Figure 2.3: Schematic diagram of membrane configurations, direct contact, air gap, permeate gap, sweeping gas and vacuum

The majority of research in this field is conducted with Direct contact membrane distillation (DCMD) configuration [8]. In this instance both sides of the membrane are in direct contact with a liquid stream. Heated liquid will flow through the evaporation channel on the left hand side of the membrane, while cooled permeate is circulated on the right side of the membrane. The main advantage of this set-up is there is only a very small gas gap between the membrane surface in contact with the condensation side

of the membrane and the condensation stream itself and this gap only exists because of the nature of the hydrophobic membrane. As a result of this, the membrane surface is cooled to a temperature very close to that of the condensation stream, providing a high temperature drop across the membrane. This creates a high driving force for mass transfer. However there is a significant amount of heat loss in this configuration as the membrane is the only barrier for the transfer of heat.

Air Gap MD (AGMD) is also a popular choice with researchers. With an AGMD configuration stagnant air gap is found between the membrane and a condensation surface. In this case, the evaporated volatile molecules cross both the membrane pores and the air gap to finally condense over a cold surface inside the membrane module. This substantially reduces the heat loss through the membrane due to the thermal insulation of the air gap. This gives lower specific energy consumption but can reduce the flux [25]. Figure 2.3 also shows a configuration known as Permeate Gap MD (PGMD). This configuration is similar to AGMD, however the gap between the membrane and the cooling sheet is allowed to fill with permeate, which is then collected from the top of the module.

Alternatively a vacuum may be applied in the permeate side of the membrane module by means of a vacuum pump. The applied vacuum pressure is lower than the saturation pressure of volatile molecules to be separated from the feed solution; this is known as Vacuum MD. In this case, condensation occurs outside of the membrane module. Although this set-up can achieve lower thermal energy consumption, the introduction of a vacuum pump increases the electrical consumption, [23].

The least common configuration in MD is Sweeping Gas. In this instance cold inert gas sweeps the permeate side of the membrane carrying the vapour molecules and condensation takes place outside the membrane module. The turbulence achieved by this circulating gas increases the mass transfer across the membrane giving a higher specific vapour flux, [27].

The majority of membrane distillation research has centred on the DCMD

configuration. This is largely due to the relative simplicity of the system, as opposed to SGMD or VMD. It is also significant to point out that desalination of water is the most common application of the DCMD research.

2.1.6 Development of membrane distillation

The first large scale desalination plants for municipal drinking water emerged in the Middle East during the 1950's. However it was not until the 1960's that membranes were first used in the process [28]. The first MD patent application was granted in 1966 to B. R. Bodell [29], he proposed using silicone membranes as a barrier to liquid that allows vapour to pass through. In 1967, Weyl [30] was granted a patent, he suggested placing the feed solution and the distillate in direct contact with the membrane. A maximum distillate flux of 1 l/m^{2}h was reported from the direct contact system. This distillate flux fell fair short of the capabilities of RO membranes system at the time, and hence the technologies popularity dwindled in lates 1960's.

However during the early 1980's several advancements in the membrane manufacturing process brought about renewed interested in MD. Manufacturers were able to make a thinner membrane, with a thickness as low as 50 μ m. Also much higher porosity values, of up to 80%, were achieved. Both of these developments led to a significant improvement in the distillate flux produced during the MD process [9]. Since this time the popularity of MD technology has grown steadily amongst academic researchers. However MD has not yet enjoyed commercial success.

2.2 Solar energy collectors

The peak solar energy incident on the earths surface is roughly 1000 KW/m^2, with wavelengths ranging from 0.3 - 2.5 μm [31]. There are two categories of solar energy collectors, thermal and photovoltaic, both derive their energy directly from solar radiation.

2.2.1 Thermal collectors

A solar thermal collector is a device which absorbs solar radiation; the heat is then transferred to a working fluid that flows through the device. The heated fluid can be used directly or collected in a thermal storage tank for use during cloudy days or at night. An ideal thermal collector should absorb the entire radiation incident on its surface, convert it into thermal energy and pass this energy to the working fluid with minimal losses. Collectors can make use of several different heat transfer fluids, such as water, anti-freeze and air. Water has better heat transfer properties than air, but can cause serious damage to the system if it is allowed to freeze [32].

2.2.2 Photovoltaics

Photovoltaic devices convert solar radiation into electricity by utilising the photovoltaic effect, first discovered by Edmund Becquerel [33]. Becquerel discovered that an electric voltage is created when two electrodes placed in a conducting solution are illuminated. Over one hundred years passed by before this principle was put into action. In 1954 the first doped semiconductor silicon solar cell was created at Bell Laboratories, [34]. A depletion region forms instantaneously when a p-n junction is made. Consider the junction in steady state condition or thermal equilibrium, i.e. the properties of the system do not vary in time. This occurs at the instance the junction is formed. The concentration of electrons is greater in the n-type semiconductor when compared to the p-type region, conversely the p-type has an excess of holes compared to the n-type region. In this situation the electrons and holes will redistribute themselves into regions with lower concentrations. Therefore when n-doped and p-doped pieces of semiconductor are placed together to form a junction, electrons migrate into the p-side and holes migrate into the n-side, forming a region at the junction that is depleted of majority carriers. The fixed donor and acceptor impurity ions that exist in this depletion zone are no longer balanced by the free charges; this creates an internal electric field with a direction that opposes any further flow of free charges. When the electric

field is sufficient to arrest further transfer of holes and electrons, the depletion region has reached its equilibrium dimensions. When the junction is illuminated, photons of energy are given to the donor and acceptor ions, creating electron and hole pairs. Hence the equilibrium of the p-n junction is unbalanced. With a sufficient quantity of minority carriers, electrons in the p-type region and holes in the n-type region, the potential energy barrier is lowered and current will flow.

Each semiconductor has a band gap energy, this is the energy difference between the valance band and conduction band, therefore the energy needed to free an electron. The solar spectrum, previous discussed in terms of wavelength, can also be described in terms of photon energy, E. A photon of energy is defined as follows [35];

$$E = \frac{hc.c}{\lambda} \tag{2.8}$$

where c is the speed of light, hc is Planck's constant and λ is the wavelength. Each semiconductor material will absorb a certain photon energy and therefore a specific proportion of the solar spectrum.

The efficiency of a solar cell is defined as the ratio between the electrical output of the cell and the solar energy incident upon its surface. Theory can predict the upper limit of a cells electrical efficiency, which is dependent on the cell material. Silicon is most commonly used, as high quality silicon material was already being manufactured for the micro-electrons market, [36]. In 1961, Shockley and Queisser el al [37] demonstrated the theoretical upper limit of a single p-n junction solar cell with a band gap of 1.1eV is 30%.

In order to improve on this efficiency researchers have recreated multijunction solar cells, with numerous junctions each absorbing a proportion of the solar energy. The current efficiency record is 44.7% for a four junction GaInP/GaAs/GaInAsP/GaInAs concentrated solar cell [38].

2.2.3 Hybrid Photovoltaic/Thermal (PV/T) collector

Only a percentage of the energy that is incident onto the surface of a PV cell will be converted into electricity, the remainder will be absorbed and converted to thermal energy in the cell. This causes the working temperature of the cell to rise. By placing a thermal receiver directly beneath the PV array this thermal energy can be recovered. A fluid passes along the back of the PV array, cooling the cells and collecting useful thermal energy so that it can be used for another purpose. There is also an advantage to keeping the PV array properly cooled, as an increase in the operating temperature reduces its electrical efficiency. For a typical concentrated silicon cell the efficiency can decrease by 0.4% with every 1°C increase above nominal operating temperature [39]. Therefore a combined PV and thermal collector offers the advantage of making use of the waste heat generated within the PV cell, as well as cooling the PV cells and therefore improving their electrical efficiency.

2.2.4 Concentrating systems

Solar concentrators are used to increase the energy incident on a receiver. This is achieved by placing an optical device between the source of radiation and the receiver. Concentrators are found in many different forms; they can be reflective or refractive, continuous or fragmented, cylindrical or parabolic. Receivers are also found in a variety of designs, convex, concave or flat, covered or uncovered [40]. Concentrators can also be categorised as line focusing or point focusing. The geometrical concentration ratio, C, is defined as the area of the aperture, A_a, divided by the area of the receiver, A_r, as follows:

$$C_r = \frac{A_a}{A_r} \tag{2.9}$$

The flux concentration ratio is the average energy flux on the receiver to that on the concentrator, however the flux density can vary over the area of the receiver [31]:

$$C_f = \frac{\Sigma E_r}{\Sigma E_a} \tag{2.10}$$

Under maximum concentration both the sun and the absorber are assumed to be black bodies of equal temperature, therefore there can be no net heat transfer between the two. If we consider the finite angle subtended between the sun and earth, determined by the radius of the sun and its distance from earth, the theoretical limit to concentration is given by [41]:

$$C_{max} = \frac{1}{Sin^2\theta_c} \tag{2.11}$$

where θ_c is the half angle of the cone subtended between the sun and the earth. For a value of $\theta_c = 4.7$ mrad, $C_{max} = 45{,}270$.

The parabolic dish reflector focuses the suns light onto a single focal point, at which a receiver is placed. In order to concentrate the suns light the dish must be directly pointed at the sun, as a result a two-axis tracking system must be used.

The receiver design is an integral part of any collector, the light concentrated by the dish must focus at the receiver were it will be absorbed. The efficiency of the concentrating system is defined by the ratio between the useful energy output, Q_u and the energy incident on the concentrators aperture Q_a:

$$\eta_c = \frac{Q_u}{Q_a} \tag{2.12}$$

The efficiency of the system is largely determined by the amount of heat lost from the receiver to surrounding environment. This heat loss occurs through conduction, Q_{lk}, convection, Q_{lc} and radiation, Q_{lr}. The total heat loss from the receiver, Q_{lt} is given by:

$$Q_l t = Q_{lk} + Q_{lc} + Q_{lr} \tag{2.13}$$

The receiver should be designed in order to reduce the heat loss, the design must take into account the shape of the receiver, the diameter of the aperture, the insulation thickness and characteristics of the surfaces. A cavity receiver typically loses 12% of the energy incident onto its aperture via convection and radiation [42].

The optical efficiency of the system is dependent on several factors including the reflectance of the dish material, the optical properties of the receiver and the geometry of the concentrator. To determine the optical efficiency the various loss mechanisms of the concentrator must be examined. This loss can occur through shading, as the receiver must be placed at the focal point of the dish causing the receiver and its structural support to block sunlight from reaching the dish. This loss can be minimised by ensuring that the aperture of the dish is much larger than the receiver. Imperfections in the dish can cause loss of energy depending on the material and cleanliness, a mirror with silver coating and low-iron glass should give 90 - 94% reflectivity. Roughly 2 - 4% efficiency can be lost during transmission through the transparent cover, typically glass, that protects the receiver from the environment, [43].

2.2.5 Concentrated Photovoltaic and Thermal (CPV/T) energy system

The MD module detailed in this thesis paper is intended for use with a solar concentrated photovoltaic and thermal (CPV/T) energy source. A schematic of the proposed CPV/T system is shown in figure 8.1. The system would consist of a parabolic dish concentrator with 2-axis tracking. Solar radiation that is incident on the aperture of the dish will be reflected and concentrated to a focal point. A combined photovoltaic and thermal receiver is placed at the focal point of the dish to collect the solar radiation. The use of concentrating optics such as a parabolic dish drastically reduces the area of the receiver required, as light is concentrated into a smaller area. Given that the receiver is often the most expensive part of a solar energy system, this can greatly reduce the overall cost [44].

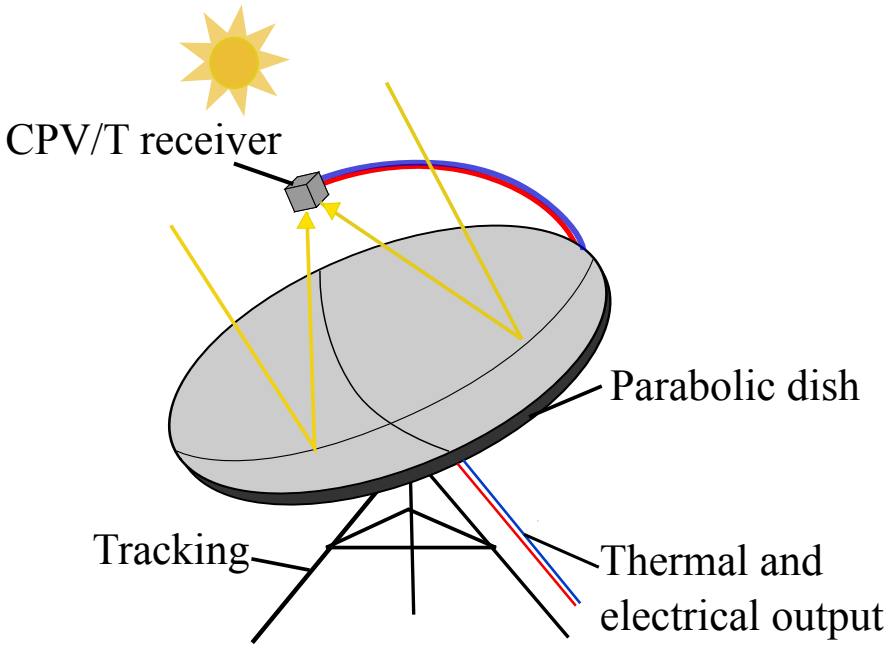

Figure 2.4: Photovoltaic/Thermal receiver with parabolic concentrator

The combined photovoltaic (PV) and thermal receiver placed at the focus of the dish would include an array of triple junction PV cells, with a thermal collector placed directly beneath. The cells proposed for use in the receiver were manufactured by Azure space, and have an electrical conversion efficiency of 36% [45]. The cells are a composite of three layers: Indium gallium phosphide, Indium gallium arsenide, and Germanium. Each material in a junction has a different band gap energy; this is the energy required to free an electron. Each layer of the cell therefore absorbs a different section of the solar energy spectrum. By layering different materials and subsequently absorbing more of the solar spectrum, a higher conversion efficiency is achieved [46].

The output from a CPV/T solar collector is both electricity from the PV cells and thermal energy from the heated fluid in the thermal collector. This system is ideal for use with an MD unit for the purification of seawater. The electricity can be used to power the pumps required to push the fluid through the system, while the thermal energy collected can be used to heat the seawater to the desired temperature for desalination, effectively creating a single standalone system that can run autonomously.

2.2.6 Solar energy fluctuations during cloud cover and the implications for CPV/T

The amount of solar energy available can fluctuate significantly throughout the day, due to intermittent cloud cover. The total solar energy that reaches the earth's surface is know as global radiation, and is a combination of direct and defuse radiation. Direct radiation is light that falls perpendicular to the earths surface, whereas defuse radiation is light that has been scattered through the earths atmosphere. The proportion of direct and defuse light that make up total global radiation can change drastically depending on the presence of cloud cover [47]. During dense cloudily conditions the light incident on the earths surface will be entirely defuse, as clouds cause the light to scatter.

When using high concentrating optics such as the parabolic dish, only light falling perpendicular to the aperture of the dish will be concentrated onto the receiver at the focus. Such variations in global radiation composition pose a more significant issue than they do for flat panel systems which also collect diffusion radiation. Vijayakumar et al [48] investigated short term direct beam radiation during cloudy conditions. The radiation was shown to rapidly reduce to zero for several minute intervals during the day, displaying an on-off behaviour.

Figure 8.2 shows direct beam radiation data collected at a test site on campus at Heriot-Watt University on three separate days. This data was collected using a solar tracker ($Solys2$) and pyrheliometer ($CHP1$) from Kipp and Zonen. Figure 2.5(a) shows direct beam radiation on the 11th of August, 2012. This day was characterised as sunny with cloudy intervals, the figure shows the same 'on' and 'off' behaviour as discussed by Vijayakumar et al [48]. The duration of the fluctuations vary significantly from 1 minute to 20 minutes. These short term energy fluctuations will result in transient operation of the MD unit, when directly coupled with a CPV/T system.

Figure 2.5(b) shows direct beam radiation in the same location on the 1st of June 2012. On this day there was heavy cloud cover in the morning which gave way to long sunny spells in the afternoon. Figure 2.5(c) shows data from the same location on

the 7th of August 2012, a sunny day with very little cloud cover. This data provides an overview the array of fluctuations in direct beam radiation seen across a variety of summer days in Edinburgh, ranging from short term fluctuations of several minutes, to long term fluctuations of several hours. The implications of intermittent MD operation are discussed in greater detail in section 2.4.

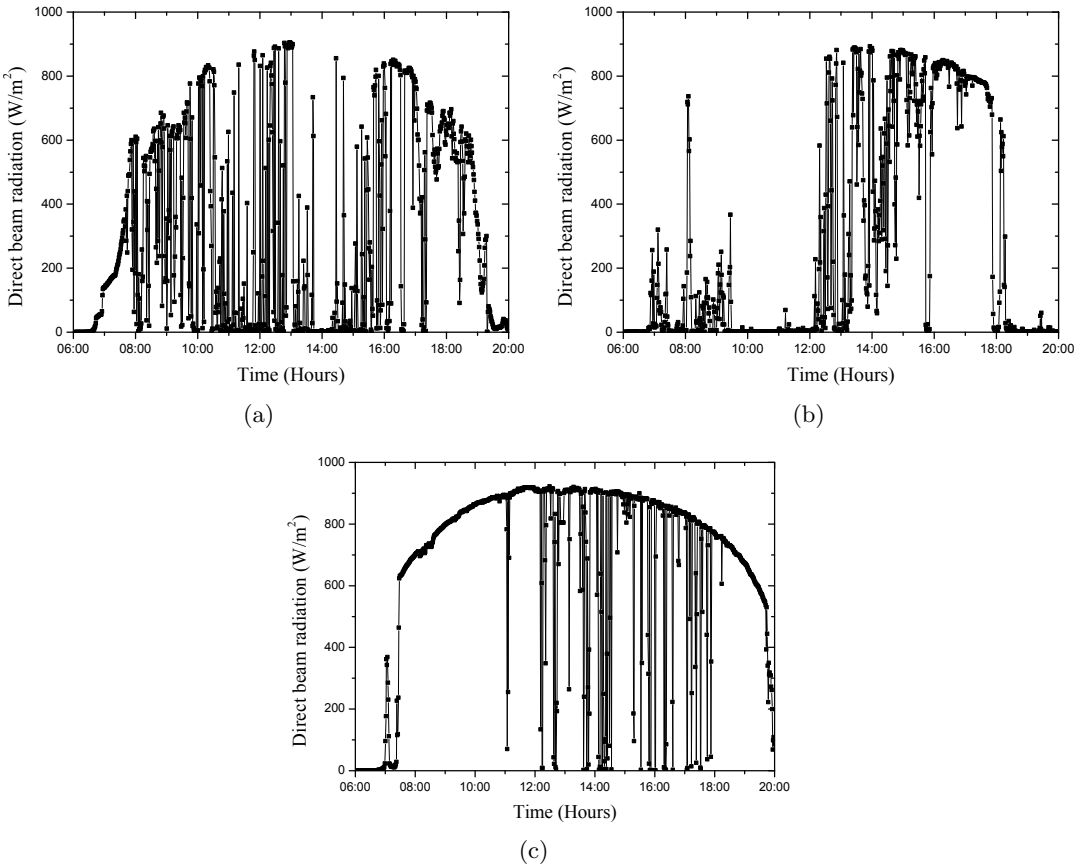

Figure 2.5: Direct beam radiation on a)11/08/12, b) 01/06/12, c) 07/08/12, Edinburgh, UK

2.2.7 Development of Concentrated Photovoltaic/Thermal collectors

The combination of photovoltaic and thermal technology can enable the collector to utilise a greater proportion of the solar spectrum and through effective cooling, increase the efficiency of the solar cell. A PV/T receiver has the potential to be the most efficient device in terms of converting solar radiation into useful energy. The combination of

photovoltaic and thermal technology first emerged in the 1970's. PV/T receivers have a variety of configurations, though they can be commonly divided into categories; flat plate PV/T collectors and concentrating PV/T collectors. This section details the development of the latter category.

Coventry [49] reported on the performance of a PV/T system with parabolic trough concentrators installed at ANU, Australia. The parabolic troughs gave a concentration ratio of 37. The cells used in the PV/T receiver were mono-crystalline silicon cells. In optimum conditions the system had an thermal efficiency of 58% and an electrical efficiency of 11%

When higher concentration ratios are used, the receiver is illuminated by highly concentrated solar irradiance therefore must be designed to remove a large amount of heat from a small area. Dupeyrat et al [50] reported the design and testing of multi-junction solar cells with a miniature heat exchanger containing micro-channels. This receiver was placed at the focal point of parabolic dish with an area of 1.1 m^2. The concentration ratio was 267. The system demonstrated a total efficiency of 79% in optimal conditions ($\eta_{th} = 53\%$, $\eta_{PV} = 26\%$).

Kribus el al [43] detailed the design and manufacture of a PV/T system with a parabolic dish. The parabolic dish consisted of a single piece of formed glass back-coated with silver, with an area of 1 m^2 and a concentration ratio of 500. The receiver was made up of high efficiency triple junction solar cells, and a cooling plate. When the coolant exiting the plate was 58°C the electrical output from the PV cells was 172W and the thermal output was 530W. The electrical efficiency of the PV cells decrease as the cool exit temperature increased, however the loss in electrical energy is recaptured as thermal energy [43]. Therefore the total efficiency of the system remained approximately 80%, regardless of variation in coolant exit temperature.

2.3 Development of solar powered desalination systems

When selecting the appropriate desalination process, again the application must be considered. Cipollina et al. [51] classified the state of development and also the capacity limit of various desalination systems in combination with renewable energy. Membrane based technologies, such as RO and MD, have often been used in combination with renewable energy sources. With their modular design and compactness, there are advantages to using membrane technology for small to medium capacity plants in remote locations [52]. PV powered RO systems are the most developed and widely used of the solar-membrane systems [53, 51]. The implementation of PV-RO systems have been evaluated for remote locations worldwide [54, 55, 56]. A feasibility study for the implementation of a PV powered RO system in rural Jordan was conducted by Gocht et al [57]. Experiments were preformed to establish the affects of fluctuating power supply from the PV on the RO performance. The group proposed the inclusion of batteries to dampen the power fluctuations. The classification of desalination technology in terms of its combination with a renewable energy source is shown in figure 2.6 [51].

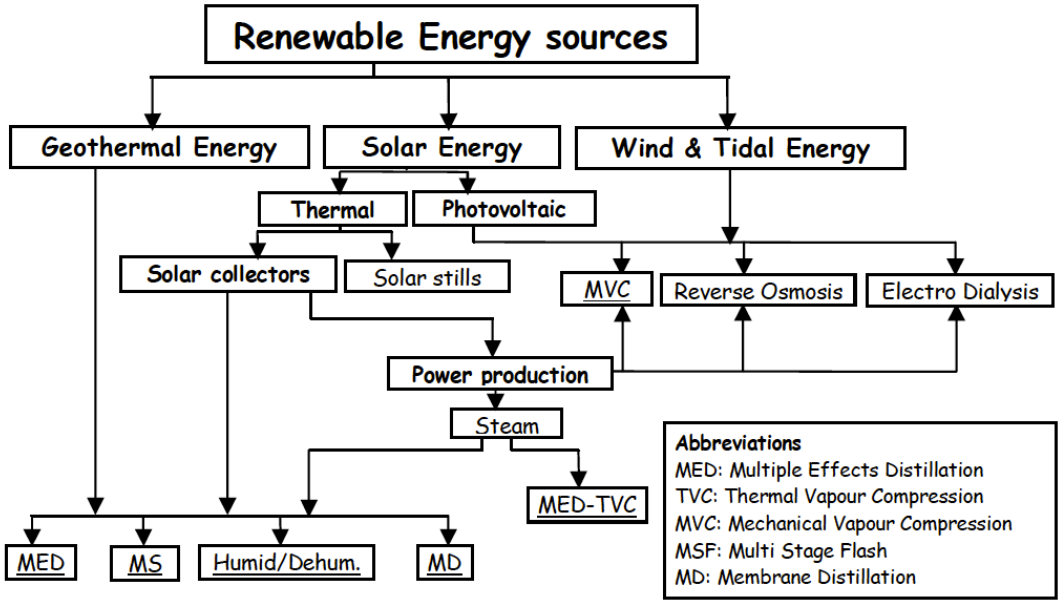

Figure 2.6: Renewable energy desalination technology overview

2.3.1 Solar powered MD

MD systems powered by solar energy have been shown to be economically competitive with RO systems in remote locations [19]. However, to date, there are no large scale MD plants in operation.

Increasingly researchers are looking to MD as a means of desalination. A number of MD projects that focus on incorporating solar energy for seawater desalination have been reported in literature. These systems have a wide variety of configurations, however solar powered MD systems can be categorised in two ways, compact systems and two-loop systems. In a compact system water is pumped directly from the solar collector, where it is heated to an appropriate temperature, into the evaporation channel of an MD module. An example of the compact system configuration is shown in figure 2.7 [18].

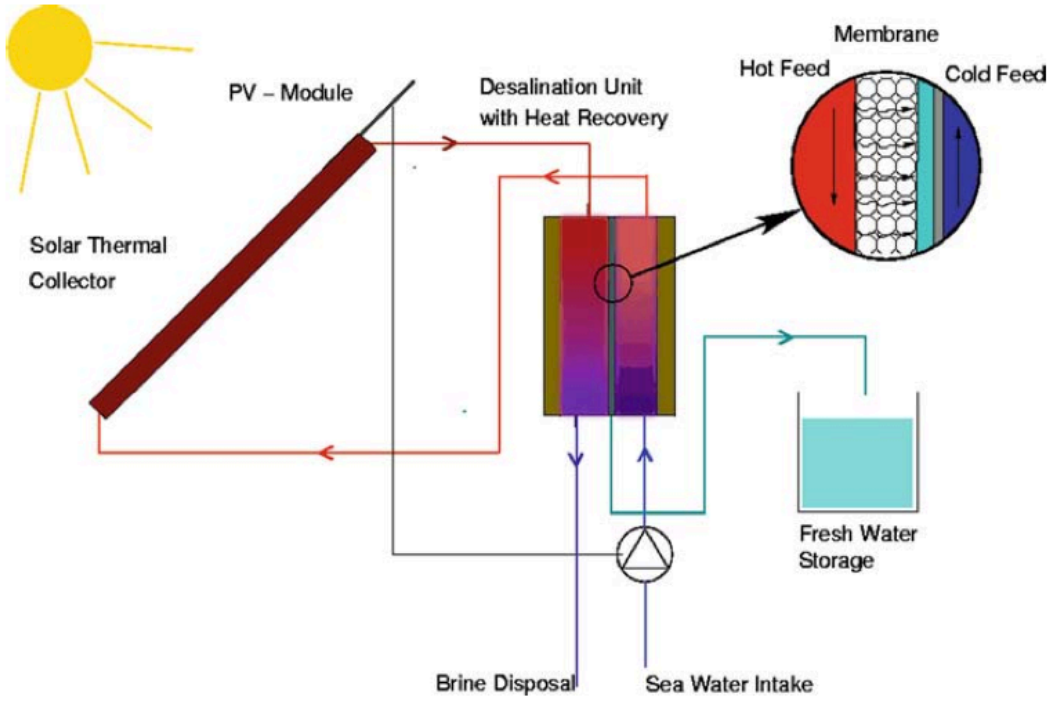

Figure 2.7: Schematic diagram of a compact system MD configuration

This type of system has greater simplicity as it does not include an intermediate heat

exchanger. Though they do not contain heat storage tanks or batteries and therefore can only operate during hours of sunlight and are subject to solar fluctuations. Given that the feed solution will flow directly through the solar collector, the evacuated tubes of the collector must be made of a corrosion resistant alloy.

In 1991 a Solar Powered Membrane Distillation simulation was demonstrated by Hogan el al [19] at the University of New South Wales in Australia. The simulation considered a system consisting of hollow-fibre MD membranes and $3m^2$ flat plate solar collectors. The results show that system would produce $0.05m^3/d$, given the small distillate flux the plant was proposed for domestic applications.

The installation and testing of various compact systems have been reported. Koschikowski et al [58] developed a spiral wound MD module using PTFE membranes with an average pore size of 0.2 μm. The module had a total area of 8 m^2. These MD modules utilise a heat recovery system aimed at lowering the specific energy consumption of the system and thus lowering the cost. Water flows from the storage tank through the condenser channel of the module, heating up as it flows. Heat is transferred from the condensed distillate to the cold feed water in the condenser channel. In this way water is preheated before it reaches the solar collector, usually increasing the temperature by between 5 - 10°C [18]. Ding et al simulated the effect of a heat recovery on the energy consumption of the system and concluded that it is best way to improve the energy efficiency and increase the plant output [59].

The modules were used in a solar powered compact system configuration that also included a 12 m^2 solar thermal collection. The system was tested at Fraunhofer ISE in Freiburg. A PV power supply was not integrated, all electrical components were connected to the grid. When investigating the dynamic behaviour of the system, it was found that the distillate flux followed very closely the changes in the hot inlet temperature of the module. It was concluded that the system could operate without the use of thermal storage, however, the distillate conductivity was not measured during temperature changes at the hot inlet of the module and therefore this effect was not

considered. The result show that the maximum distillate output was 15 l/h, and the total distillate produced was 130 l/day. Koschikowski et al [58] developed a model to simulate the output of this system at various locations. The results show that the system, when located in Eilat, Israel, could produce 28 l/m^{2}d on a clear day in August, which is equal to 3.5 l/m^{2}h assuming 8 hours of operation.

With funding from two EU projects, MEMDIS and SMADES, a further five compact systems have been installed [60]. The main components in the systems include a solar thermal collectors, an MD module developed by Fraunhofer and 500 litre storage tank. Each of the systems was designed to run autonomously with very low maintenance needs. These systems are located in various locations around the world, Pozo Izquuierdo (Grand Canary), Alexandria (Egypt), Irbid (Jordan), Morroco and Tenerinfe (Spain). The results from each system varied depending on the amount of solar irradiance it received.

Banat el al [14] reported on the system in place in Irbid, Jordan. The system uses spiral wound membranes with an effective area of 10 m^2. The water was heated by passing through a corrosion resistant flat plate collector, with an area of 5.73 m^2. A PV module was used to provide electrical power to a DC pump and magnetic valves. The system produced a maximum distillate output of 120 l/d. The lowest distillate conductivity observed was 5 μS/cm. However this value was not stable during the first hour of operation in the morning. This behaviour is discussed further in section 1.4 on transient operation of MD modules.

A two-loop system incorporates a desalination loop using seawater and a solar collector loop with a working fluid such a glycol. An example of the configuration used in a two-loop system is shown in figure 2.8.

The two loops within the system are connected by a heat exchanger. This allows components within the solar collector loop to be made from cheaper materials, as they do not need to be resistant to corrosion from seawater. Two-loop systems often incorporate thermal storage tanks and batteries to extend operation time beyond

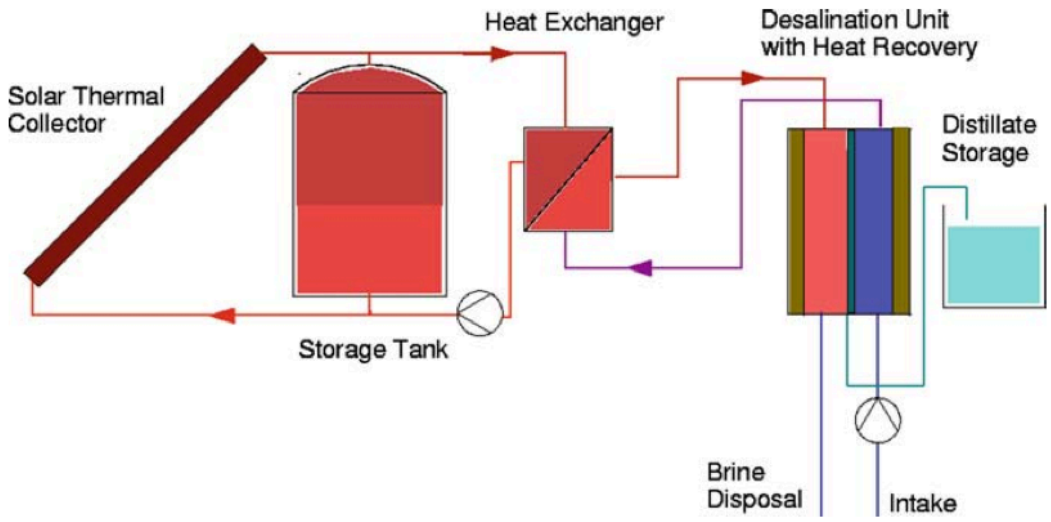

Figure 2.8: Schematic diagram of a two-loop system MD configuration

daylight hours and mitigate solar fluctuations.

Several large two-loop systems have been installed and tested. The first of the two loop systems was installed in 2005 in Aqaba, Jordan and the second in Gran Canaria in 2006. Banat el al reported on results from the first system, known as 'Large SMADES'. This system had two distinct loops. The solar loop consisted of 72 m^2 flat plate collector and a 3 m^3 storage tank which is used to collect surplus heat throughout the day and extend operation into the evening. The inlet temperature of the system was maintained at 80°C and excess heat was diverted to the thermal storage tank. The desalination loop contained 4 MD modules, each with an effective membrane area of 10 m^2. The maximum distillate flux of 1.5 l/m^2h was reported. The use of thermal storage enabled the system to operate for a further 6 hours after sunset, giving a maximum daily output of 792 l/day.

Koschikowski et al [60] reported results from the two-loop system installed in Gran Canaria. This system contained a flat plate solar collector with an area 90 m^2 and a 4 m^3 thermal storage tank. The desalination looped contained 5 MD modules, each with an area of 10 m^2. The results show a peak distillate flux of 1.6 l/m^2h. With the use of

thermal storage the system was able to continue running until 4.30am, giving a total distillate output of 1200 l/day.

In 2010 and 2011, 2 autonomous solar powered MD plants were developed by Fraunhofer ISE and were installed in Namibia and Gran Canaria. Schwantes et al [12] reported on the design and the performance of these plants. The plant in Namibia had a total membrane area of 168 m^2 and 232 m^2 of flat plate solar collectors. The plant in Gran Canaria had a total membrane area of 120 m^2 and 186 m^2 of flat plate solar collectors. The plant in Namibia produced around 2000 l/d of distillate, while the plant in Gran Canaria produced on average 1000 l/day. The aim of this comparative study was assess the impact of parameter such as feed flow rate, salinity, and system design on energy consumption and thermal efficiency of the system.

2.4 Transient operation of membrane distillation systems

When powered entirely by a solar source, an MD module will only be capable of operating for a proportion of the day; this is usually determined by the number of daylight hours. However the are several solar powered pilot MD plans that have aimed to extend the hours of operation. By using a control system and storing excess heat, it has been possible to extend the operation by several hours [12]. However eventually the temperature of the feed gradually decreases as the heat store is depleted and the pump is then switched off; the modules will cool down during this time. Therefore in all cases, the module experiences transient operation.

Transient operation of an MD module is known to cause fluctuations in the distillate output from the system. Several research groups have reported results showing rapidly decreasing distillate conductivity during the first hour of operation after an over-night shut down. Winter et al [11], developed full scale spiral wound MD modules using PTFE membranes. Experiments were conducted to determine the performance of the modules and a range of feed salinity was used in the tests. An experiment was conducted with a feed salinity of 50 μS/cm, the feed temperature of 80°C and feed flow rate of 400 kg/hr;

these were consistent throughout the experiment. However the conductivity distillate produced decreased within the first hour of operation, from 5μS/cm to 0.36μS/cm. After 2 hours the value was stable at 0.19μS/cm.

Two autonomous solar powered MD systems were constructed and tested as part of the SMADES project. A single loop system known as 'compact SMADES' comprised of a spiral wound MD module with membrane area of 10 m^2. PTFE Gore G02 membranes were used, the same as those used in this research. The module was directly connected to a solar thermal panel with an area of 5.73 m^2. When testing the 'compact SMADES', Banat el al [14] reported maximum distillate output of 120 l/d. An initial distillate conductivity of 40 μS/cm was reported, which then decreased to 5 μS/cm within one hour. The second system tested by the project, known as 'large SMADES', consisted of separate solar and MD loops that were connected by a heat exchanger. Although the system configuration was different, similar 10 m^2 MD modules containing the same PTFE membranes were used. Similar behaviour was observed in the conductivity of the distillate flux shortly after the system was switched on in the morning. The initial distillate conductivity was 1000 μS/cm, this value then deceased to 40 μS/cm over the course of roughly one hour [13]. Though this behaviour is discussed there is no explanation given. The system included heat storage which enabled it to continue operating for a further 6 hours. It can been seen from the data presented by Banat el al [13] that the distillate conductivity gradually increases while the system was running in heat store mode, and the temperature of the feed gradually decreased.

These data indicated that the distillate conductivity produced by the module may be temperature dependant, as a rapid decrease in conductivity is seen when the module is heated in the morning and a low increase is seen as the heat store is gradually depleted in the evening. To investigate the possible reasons for this effect, samples of the PTFE membrane were imaged at various temperatures with the use of a Scanning Electron Microscope (SEM) and the images were analysed.

2.5 Image analysis of membrane pore structure

Several research groups have used image analysis techniques to further understand the structure of microporous membrane material. Calvo et al [61] used an SEM to image the surface of a polycarbonate membrane. This image was then analysed to determine the pore size distribution in the membrane. The method yielded values of mean pore size that were in agreement with the nominal data provided by the manufacturer. However it also gave insight into the range of pore sizes in the membrane, resulting in a better understanding of the structure of the membrane which could in turn be used to more accurately predict performance characteristics such as flow rates and retention.

The membranes used in MD are commonly made of polymer material, such as PTFE. This material is consider to be thermally stable within the range of operating temperatures used in MD. However PTFE will expand when heated, and in the context of microporous material such expansion could have a significant effect on the structure of the membrane. Saffarini et al [62] investigated the effects of temperature on the microstructure of PTFE with the use of an SEM with a Peltier heating stage inside of the chamber. Images of the membrane sample were taken as the temperature of the Peltier stage was increased from 25°C and 50°C; upon reaching 50°C the sample was left for 5 minutes and an image was taken again.

The operating temperature range for MD is 30°C to 80°C, however temperatures between 60°C to 80°C are preferable. In this research, the pore size distribution within a membrane sample was investigated at room temperature. The samples were then heated to temperatures between 60°C and 80°C. The temperature of the Peltier stage was set and the sample was left to heat for 90 minutes. This was deemed necessary given that PTFE has low thermal conductivity and therefore would heat up slowly. The sample was imaged every 10 minutes so that the change in structure over time could be monitored.

2.6 Summary

There have been several pilot trials of solar powered MD systems which have aimed to establish the performance of such systems in various configurations. These systems have typically included two separate solar collectors, one thermal array to heat the saline feed solution and one PV array to power the pump and meet any other electrical requirements of the system. However, to date, there has not been a study of an MD system powered by a combined Photovoltaic/Thermal collector with the use of a parabolic concentrator. A single CPV/T collector would be capable of heating the feed and producing the electrical power needed, reducing the cost of materials and improving efficiency.

However a CPV/T system would present challenges of its own, as the output from the system is intermittent. In all cases, a solar powered MD system would not be capable of running continually; the modules are shut down over night allowing them to cool. During the day the output from a CPV/T system fluctuates, resulting in short periods of heating and cooling. Several researchers have noted fluctuating distillate conductivity during intermittent use of an MD module. However this effect has not been fully characterised experimentally. This research presents experimental data from an MD module while subject to fluctuating temperature, ranging from periods of 5 minutes to 12 hours.

Chapter 3

Experimental set up and measurement techniques

This chapter gives details of the experimental rig and measurement techniques used throughout this research. The configuration of the membrane module is described and the properties of the membrane material are discussed. Specifications of all equipment used in the rig are given, including the pump, sensors and data acquisition systems. The rig was designed to enable testing of an MD module's performance during intermittent use, such as applications with an overnight shut down period. It was also tested with short term fluctuations, such as those from a solar energy source. The experimental procedures used to test the performance of the module in these conditions are detailed

here. The procedure for assessing the effects of temperature on the structure of membranes used in the module is also given.

3.1 Membrane System overview

The experimental rig is shown in figure 3.1. Saline feed solution is stored in a 40 litre tank. The feed solution is pumped from the tank into the cold channel of the membrane module by a 505 Watson Marlow peristaltic pump. The feed is preheated as it flows through the cold channel of the module. After exiting the cold channel, the feed solution passes through a heater coil placed inside a water bath, where is it heated to the desired temperature. The feed then enters the hot channel of the module, where it flows along the membrane. A percentage of the feed evaporates at the surface of the membrane and the vapour formed defuses through the membrane pores, where it condenses against the plate that forms one wall of the cold channel. After condensing, the distillate solution flows out of the module where it is collected. The feed solution that remains liquid, and therefore can not pass through the hydrophobic membrane, flows out of the hot channel where it can be collected and recirculated.

Four T-type thermocouples were used to measure temperature at the entrance and exit of the hot and cold channels. A digital manometer manufactured by Omega was used to measure the pressure drop across the module. A conductivity probe measuring from 0-2000 S/cm, was placed in the distillate outlet pipe. The distillate output flowed into a beaker on a weighing scale; the scale logged the weight to a computer via Windows^{TM} HyperTerminal program. The rate of increase in weight was then used to determine the distillate flow rate. Further details of the sensors used in the rig, including their positioning, precision and accuracy, are given in section 3.3.

In this setup, a water bath is used to heat the feed solution and simulate the energy input from a solar source. A GD120 stirred water bath from Grant Instruments was used for this purpose. The GD120 immersion thermostat has a heating range from 5°C to 120°C. A stainless steel heat exchanger coil was placed inside the bath and

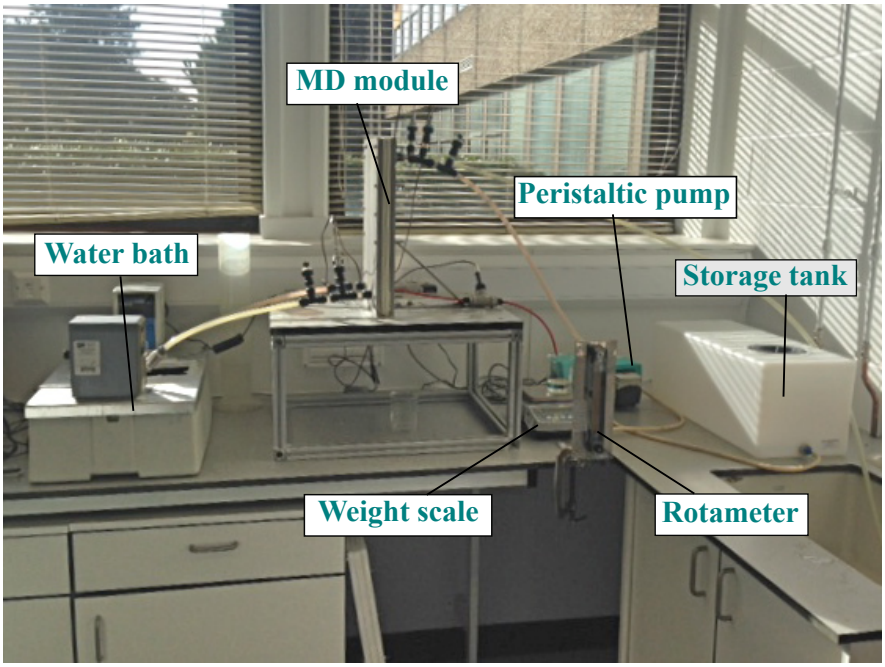

Figure 3.1: Image of the MD system

feed solution was heated as it flowed through the coil. This method is preferred as the feed solution used in the experiments has a high salt concentration. Pumping the feed solution directly into the bath would cause corrosion of the heating elements.

The Watson Marlow peristaltic pump was also chosen to avoid corrosion. It is a positive displacement pump with a rotor and 3 rollers. A platinum silicon tube with a bore size of 8mm and a wall thickness of 1.6mm was placed through the rotor. The tube is compressed by the rollers as the motor turns and fluid is pushed through the tube. The feed solution does not come into contact with the metal components in the pump, preventing corrosion. The RPM of the motor determined the flow rate and this value can be set, however positive displacement pump does not always maintain a constant set flow rate. Over time the tube can become compressed and the flow rate can decrease. To ensure that the flow rate was maintained throughout the course of all experiments a rotor-meter was placed after pump and the flow rate could be checked and maintained.

All of the connecting pipes and fittings within the system are made from plastic to

avoid corrosion from sustained contact with the feed solution of high salt concentration. The connecting pipes are made of nylon and have a bore diameter of 12mm. The fittings used are made of acetal and join with the piping via push connectors.

3.2 Membrane module

3.2.1 PTFE micro-filtration membranes

The membranes used in the system are Gore^{TM} Microflitration Media. The active side of the membrane is made of expanded PTFE. The support layer is made of unwoven polypropylene. Two Gore^{TM} membranes were used this study, G02 and G04. They have an average pore diameter of 0.2 μm and 0.45 μm and a minimum bubble point pressure of 12.8 psi (0.88 bar) and 9.0 psi (0.62 bar) respectively. Further details on the properties of these two membranes are given in table 3.1.

	G02	G04
Pore size (μm)	0.2	0.45
Support material	Woven Polypropylene	Unwoven Polypropylene
Minimum bubble point	12.8 psi (0.88 bar)	9.0 psi (0.62 bar)
Typical thickness (mm)	0.24	0.26

Table 3.1: Properties of the Gore^{TM} membranes

3.2.2 Module configuration

The rig consists primarily of a Membrane Distillation (MD) module, made of polypropylene frames and stainless steel end plates. The MD module has an air-gap configuration and planar geometry similar to a plate heat exchanger. An expanded assembly of the module is shown in figure 3.2. The system includes a heat recovery design aimed at lowering the specific energy consumption of the module. There are three channels: a central distillate channel, with hot and cold feed channels on ether side. A condensing plate made of polypropylene divides the cold channel from the distillate. A hydrophobic membrane is placed between the hot channel and the distillate

channel. Ambient feed solution flows through the cold channel along the condensing plate, heating up as it passes through. This helps to recover heat from the distillate on the other side of the condensing sheet; it also helps the distillate vapour to condense. Therefore the feed is preheated before it reaches the water bath. The preheated feed passes through the stainless steel coil placed inside the water bath, where it is heated further to the desired temperature of up to 80°C. The feed solution then enters the hot channel, where it flows along the membrane.

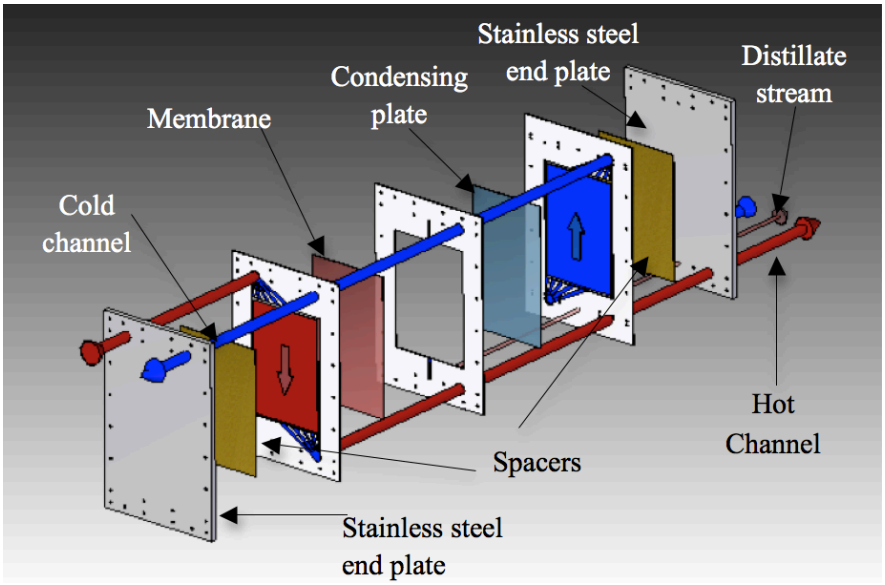

Figure 3.2: Exploded view of the MD module

Once in contact with the membrane, the pure water vapour can pass through the pores and condense in the distillate channel. The membrane used in this module measures 0.25 m x 0.175 m, equating to a surface area of 0.04375 m^2. The condensing plate is made of polypropylene. It has the same dimensions as the membrane and a thickness of 70 μm. The membrane and condensing plate were thermally welded to polypropylene frames, which are 3mm thick. Welding the polypropylene support layer of the membrane to the frame gave a good water-tight seal; the results of which can be seen in figure 3.3. This method was preferred as it was not possible to find an adhesive that was food safe and could withstand the operating temperatures of the system.

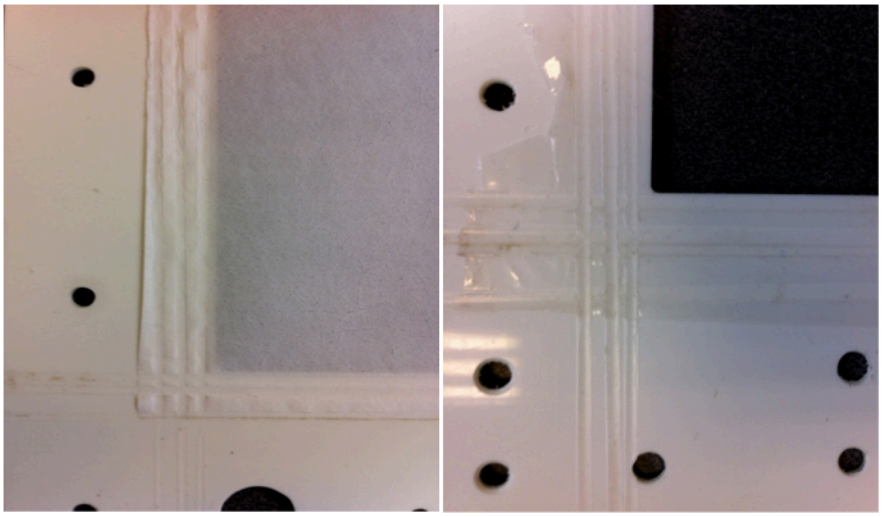

Figure 3.3: Thermal welding of a) the membrane and b) the condensing plate, to polypropylene frames

Spacers were placed inside the channels to ensure that they remain open and to encourage mixing in the feed solution. The spacers used are manufactured by Tenax CN11, which have a total thickness of 3mm, equal to the width of the frame and therefore the channels. Lateral baffles made using 3mm thick solid silicon pieces were placed in the hot and cold feed channels to guide the flow of the feed. Images of the spacers and baffles are shown in figure 3.4.

The outer plates are 3 cm thick and are made from stainless steel; this material was chosen to provide structural support to the frames. In previous bench scale MD units the outer plates were made of polypropylene or perspex. In both cases the plates became warped and distorted after use, causing leaks in the system [63]. A 1mm thick solid silicon sheet was used to form a gasket, creating a water tight seal between all frames and the plates.

3.3 Sensors

Several sensors were used to take measurements throughout the system. Figure 3.5 shows a schematic diagram of the experimental setup used to test the MD module,

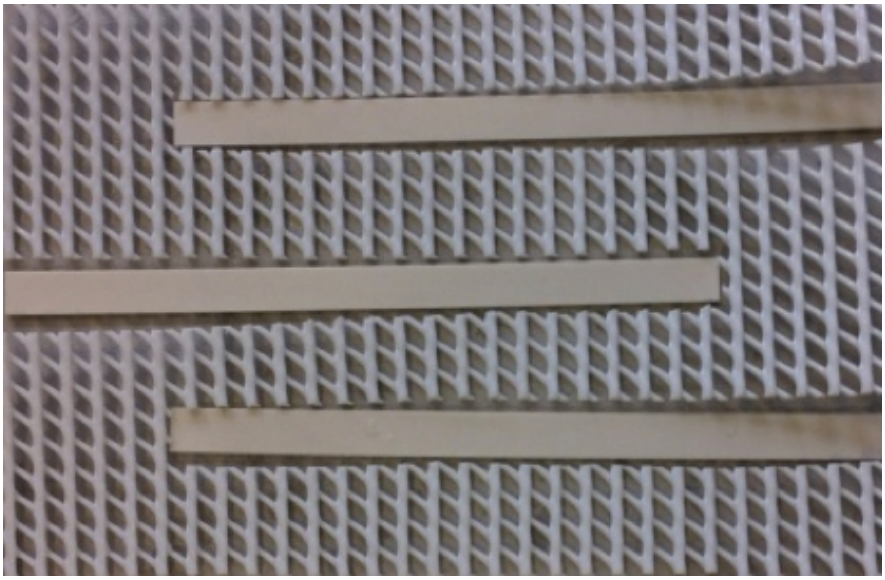

Figure 3.4: Spacers and baffles

including the location of the sensors.

3.3.1 Feed water measurements

Temperature measurements of the feed stream were taken at four points on the rig, before entering and after exiting the cold and hot channels. The measurements were taken using mineral insulated T- type thermocouples with a pot seal, from TC direct. The thermocouples have a stainless steel sheath with a diameter of 3mm and length of 150mm. The T-type thermocouple has a measurement temperature range from 0 - 400 °C.

The feed flow is provided by a 505 Watson Marlow peristaltic pump, capable of providing a flow rate of up to 1.98 l/min. The flow rate can be controlled directly at the pump, by increasing the Revolutions Per Minute (RPM) of the rotor. The RPM could be increased by increments of 5. However the silicon tube inside rotor becomes deformed over time; as a result the flow rate can gradually decrease with usage. Therefore the feed flow rate was monitored and adjusted with a rotameter and valve. The rotameter was manufactured by Omega; its frame is made of stainless steel

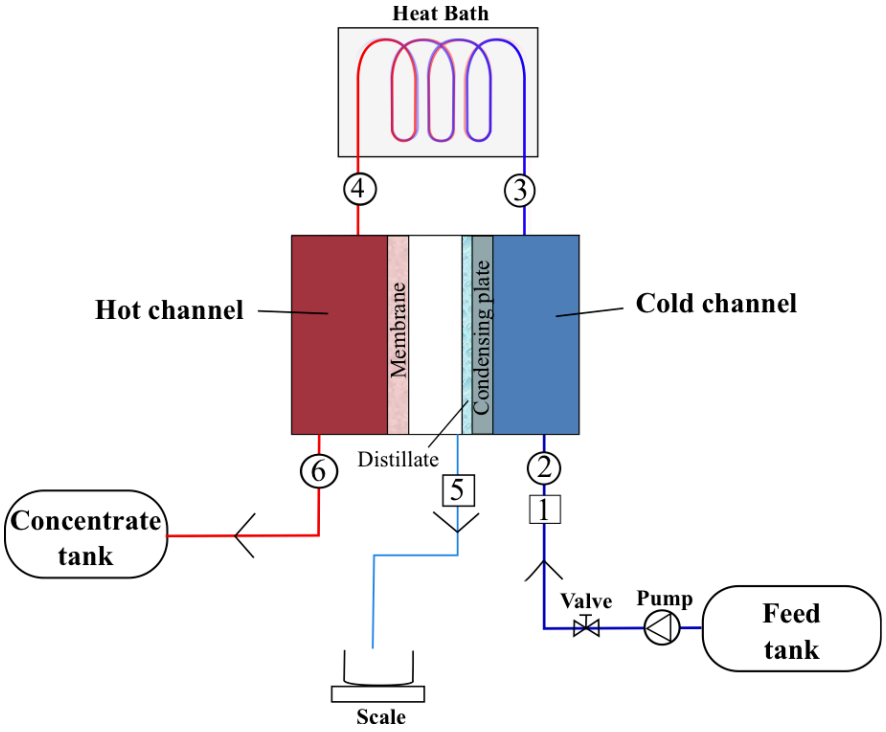

Figure 3.5: Schematic diagram of experimental setup: (1) feed conductivity sensor, (2) T1-cold inlet thermocouple, (3) T2-cold outlet thermocouple, (4) T3-hot inlet thermocouple, (5) distillate conductivity meter, (6) T4- hot outlet thermocouple.

316, with a 150mm scale glass flow tube, carboloy float material, and 6 turn valve. This particular model was chosen as the materials are resistant to corrosion, an important property since it is in direct contact with the feed solution. The maximum operating pressure is 13.8 bar and the maximum temperature is 121 °C. The rotameter has a range of flow rates between 0.19 - 1.95 l/min.

A digital manometer is used to determine the pressure drop across the experimental set up. The pressure drop is a measure of the loss of power in the module due to friction. The pressure of feed solution going into the module at the cold channel inlet was measured by a digital manometer. The feed exiting the module at the hot channel outlet is open to the atmosphere. Therefore the pressure drop is the difference between inlet pressure and atmospheric pressure. The digital manometer used is made by Omega and has a measurement range of 0 - 0.2 bar, with a precision of 0.01 bar.

The conductivity of the feed solution was measured using a hand held conductivity meter from WTW, with a conductivity range from 0-200 mS/cm and a precision of 0.1mS/cm. The value for electrical conductivity, EC, can be converted into a value of salinity (mg/l) using the following equation:

$$Salinity = k * EC \ , \tag{3.1}$$

where k is a conversion factor equal to 0.625, determined by a calibration curve for NaCL in de-ionised water at 13°C.

3.3.2 Distillate measurements

Due to the small area of membrane used inside the bench scale system, the distillate flow rate produced is very low. Therefore a weight scale was used to measure the flow rate. A beaker which collected distillate was placed on the scale directly below the outlet of the membrane module. The value of the weight measured by the scale was logged to a PC via a hyperlink terminal, and the values where then converted into a flow rate. The scale, made by Kern, has a maximum weight capacity of 2500g with a precision of 0.01g and an RS 232 interface.

The electrical conductivity of the distillate was measured using an in-line conductivity probe from Vernier. Data from the probe is sent to the PC via Go!Link USB sensor interface and LoggerLite^{TM} software. The sensor probe is 12mm in open diameter and 150mm in length. The range on the senor can be altered between 3 modes, low (0-200 μS/cm), medium (0-2000 μS/cm) and high (0-20,000 μS/cm). Throughout the duration of the experiments the sensor was used on its medium setting, therefore having a precision of 0.1μS/cm. The eyelet aperture of the sensor must be fully submerged to give an accurate reading, therefore it was placed inside a well fitting where the distillate was able to pool.

The specifications and response times for all of the sensors used to measure the performance of the membrane system are provided in table 3.2.

Measurement	Sensor position	Manufacturer (type)	Model number	Operating range	Accuracy*	Precision	Response time
Flowrate	Feed	Omega (rotameter)	FL-468-C	0.2-1.95 ($lmin^{-1}$)	± 5 %	0.01 l/min	NA
	Distillate	Kern (scale)	PCB	0-2500 (grams)	± 0.2%	0.1g	0.1ms
Conductivity	Feed	WTW (hand held)	LF 318	0-200 ($mScm^{-2}$)	± 0.5%	$0.1 mScm^{-2}$	NA
	Distillate	Vernier	CON-BTA	0-2000 ($\mu\ Scm^{-2}$)	± 2%	0.1 ($\mu\ Scm^{-2}$)	5s
Temperature	Feed/ concentrate	TC Direct	T Type 405-134	0-400 (°C)	± 1%	0.1°C	0.8s
Pressure	Feed	Omega	HHP668	± 0.2 (bar)	± 1.5 %	0.01 bar	NA

Table 3.2: Specification of the sensors used in the experimental rig. *As stated by the manufacturer

3.4 Data acquisition

Feed temperature data from the thermocouples were logged at a rate of 1Hz. The thermocouples were connected to a National Instruments data acquisition card, used to acquire 200 kS/s and at a 16 bit resolution. LabVIEW^{TM} software was used for acquisition of the thermocouple data. The Vernier distillate conductivity probe also logged directly to the PC via loggerlite^{TM} software. The distillate flow rate was measured using a KERN weigh scale, the increase in weigh recorded was converted into a flow rate. The scale was connected to the PC using RS 232, and data were collected using the HyperTerminal.

3.5 Scanning Electron Microscopy and image analysis

Images of the PTFE membrane were taken at Heriot-Watt University centre for Microscopy. An FEI Quanta 3D Scanning Electron Microscope (SEM) was used with a field emission source. A focused beam of electrons is fired at the sample; these electrons interact with the atoms in the sample causing to emit a signal and this signal can be measured to give information about the samples topography. However for the SEM process to work the sample must be electrically conductive [64]. Therefore the PTFE membrane samples were coated with a thin layer of gold before they were imaged. A sputter coater was set to 17 volts and operated for 30 seconds, to give a 5μm coating of gold.

In order to image the membrane samples at high temperature, an Environmental Scanning Electron Microscope ($ESEM$) was used at the Laboratory for In-situ Microscopy and Analysis ($LIMA$) at the University of Oxford. A Carl Zeiss EVO LS15 ESEM equipped with a LaB6 electron source was used. The SEM set up at LIMA is shown in figure 3.6

The SEM is also equipped with a Deben Coolstage, capable of temperatures ranging from -25°C to + 150°C. The temperature display has a resolution of 0.1°C and stability

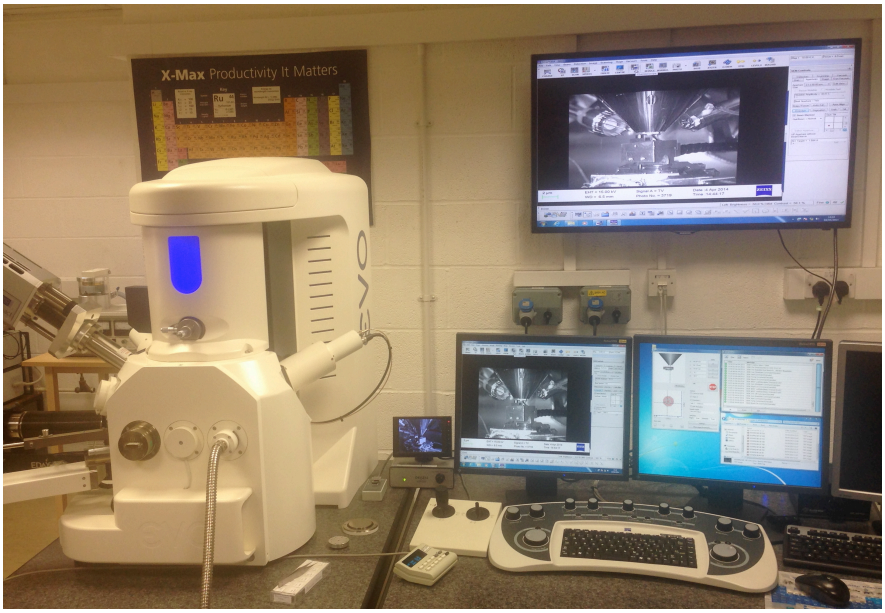

Figure 3.6: SEM equipment set up at LIMA, University of Oxford

of ± 0.2°C. The maximum heating rate is 100°C/min

The images were analysed using ImageJ 1.48 software. The 64-bit ImageJ64 applications was used as it was faster. The threshold function was used to analyse porosity of the membrane. The Wand tracing function and Region Of Interest (*ROI*) manager tool were used to select and measure individual features on the images.

3.6 Experimental procedure

A series of experiments were designed to characterise the performance of the bench scale MD system under steady-state conditions, fluctuating conditions and during intermittent use. These experiments provided a basis for understanding the significance of intermittency and solar fluctuations, while also determining the safe operating conditions for the MD system.

SEM imaging was used to investigate the temperature effect on the structure and pore size of the membrane material. Understanding the process of heating and cooling the material can shed light on the influence of intermittency and solar fluctuations on

the operation of the module. All of the experimental procedures are described in detail below.

3.6.1 Feed water preparation

The salinity of the feed solution remained constant throughout all the experiments described below. Given the small surface area of the membrane and low distillate flow rates the percentage recovery of the system is very low, therefore the concentration of the feed does not change significantly during operation. The feed solution was prepared with high-purity NaCl (>99% NaCl) and de-ionised tap water with a conductivity of 3 μS/cm. A feed concentration of 35 g/l was used, as this typically represents the salinity of seawater and is most commonly used in desalination research. Therefore this allowed for direct comparison with results from other research groups.

3.6.2 Steady state characterisation of MD system

The system was operated for an hour with constant inputs, before the distillate output from the system was stable and the steady state performance of the module could be characterised. This established a baseline for comparison with results from the system during intermittent use and solar fluctuations. It also enabled the experimental results to be validated against a mathematical model that predicted the MD module′s performance. This also established that the system was operating as expected.

The feed solution was prepared as described above at a constant concentration of 35g/l. The feed temperature was varied from 30-80°C, for fixed flow rates. After each temperature increase the system was given an hour to stabilise before measurements were taken. The influence of feed flow rate was investigated between the range of 0.2-1.0 l/min.

3.6.3 Imagining the membranes with a Scanning Electron Microscope (SEM)

A SEM was used to image the PTFE membrane material and investigate its microstructure at room temperature. ImageJ software was used to gain information about the membrane′s properties, such as porosity and pore size distribution.

The sample was then placed on a Peltier heating stage inside the SEM chamber. The initial temperature of the sample and the chamber was 17°C. The temperature of the stage was set using external controls. The stage reached its set temperature in under 20 seconds. The sample was then imaged every 10 minutes over an 80 minute period. The images were analysed to gain an understanding of how the material expanded over time when heated. The samples were tested when heated to temperatures ranging from 60-80°C, as this is the desirable operating range of an MD system.

A lumped system analysis was carried out to understand the rate of heat transferred to the sample by conduction when inside the chamber. This facilitated a greater understanding of the rate at which the material was heated over the course of the 80 minute experiment, allowing the relationship between temperature and pore size to be established.

3.6.4 Intermittent use and start up period

It was observed that during the first hour of operation of an MD unit, after the system had been switched off for an over night period, the distillate output values were not stable. This is despite all the operating parameters remaining constant from the outset. The start up period was therefore investigated further.

A constant feed salinity of 35 g/l was used and the feed flow rate remained at 0.6l/min. The temperature of the feed solution entering the hot channel was kept constant. A range of inlet temperatures from 60 - 80°C were tested.

3.6.5 Controlled fluctuations

Solar irradiance has characteristic short term fluctuations, that occur as a result of intermittent-cloud cover. Such short term fluctuations in solar irradiance will result in fluctuations in the temperature output from a solar collector. The effects of these fluctuations on the performance of the MD module were investigated. The aim was to ascertain the suitability of MD for direct coupling with a solar energy collector.

A square wave temperature function was applied to the feed solution entering the hot channel. This was achieved by removing the heat exchanger coil from inside the heated water bath, and then returning it to the bath periodically. An example of the system temperature response to a square wave function is shown in figure 3.7.

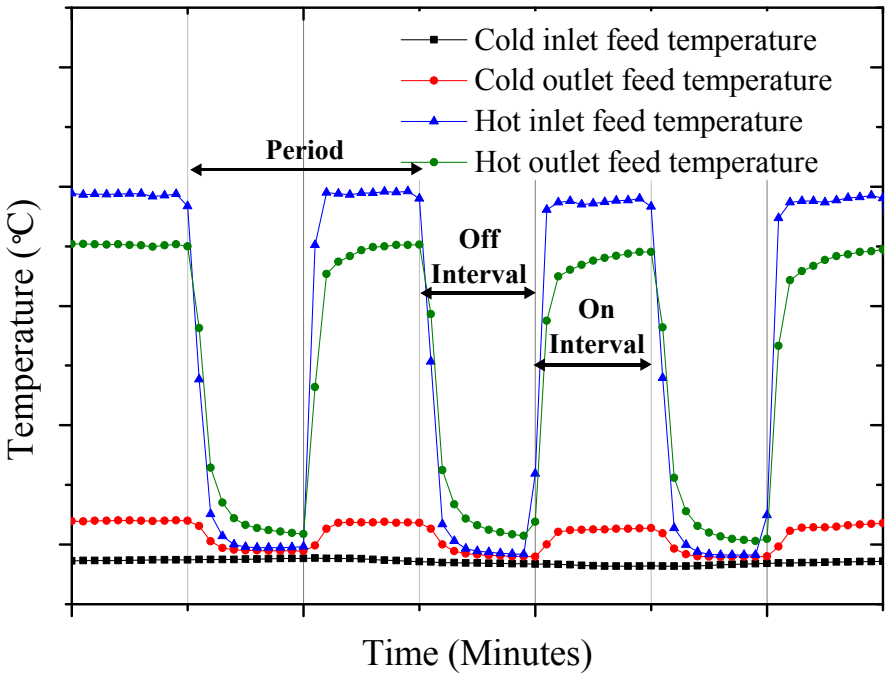

Figure 3.7: Square wave temperature function of the feed solution entering the hot channel of the MD unit

The starting point of an off interval is defined as the time from when the coil is lifted from the bath and the temperature begins to drop; i.e. not when the temperature has reached an ambient value. The wave is not a perfectly square digital input, as the

heat capacitance of the coil itself means the fluid temperature takes time to drop after the coil is removed from the water. An on-interval is the time from placing the coil in the heat bath until it is lifted out again. The period is defined as one full cycle, composed of an off and on interval.

Cycles of on/off intervals of equal duration ranging from 5 minutes to 20 minutes were tested. The temperature of the feed solution entering the hot channel was maintained during an on interval. Inlet temperatures of 60 and 80°C were tested.

3.7 Summary

An overview of the experimental rig is given in this chapter. The properties of the membranes used in the bench scale unit are detailed, as are the design and configuration of the module itself. The sensors in the rig are outlined and their accuracy and precision is given.

The experimental rig facilitates the testing of MD module during intermittent use and with fluctuating energy inputs. Various procedures were untaken in the course of this investigation and a description of the experimental procedure was presented in this chapter.

Chapter 4

Uncertainty in experimental measurements

Experimental error is defined as the difference between a measurement and the true value [65]. However, the true value is rarely known. Instead the term uncertainty is used, this describes a possible value that an error may have [66]. A full account of the uncertainty in all experimental measurements are presented so that the results and trends in the data can be reviewed in context. In this chapter a brief overview of uncertainty analysis is discussed and the methods of calculating uncertainty in the experimental measurements are detailed. Calibration curves for the instrumentation used during the experimental measurements are included.

4.1 Method of calculating uncertainty

An analysis of the error in all experimental measurements made during this study was carried out. The uncertainty, U, in the measurement is reported with a 95% confidence level. Therefore it can be stated that the true value is within ± U of the stated measurement, with 95% certainty. The uncertainty interval is defined as [67]:

$$U = \sqrt{B^2 + P^2} \ , \tag{4.1}$$

where B is the bias limit, a fixed error inherent in any measuring device. P is known as the precision limit, defined as 2 times the standard deviation from the mean value, were the experiment was repeated over 30 times under the same conditions with the same equipment [67].

Standard deviation is defined as [68]:

$$S_N = \sqrt{\frac{1}{N}\sum_{i=1}^{N}(x_i - \overline{x})^2}, \tag{4.2}$$

where $x_1, x_2, ..., x_N$ are the values in the sample, N is the size of the sample and $\overline{x}$ is the mean value of the sample.

When a result, R, is a function of several measurements x_i, it is expressed as follows:

$$R = R(x_1, x_2, ..., x_n) \ , \tag{4.3}$$

The precision error, U_R, of the result R is calculated by combining the uncertainty in the individual measurement by root-sum-square method, as shown in equation 4.4, [69].

$$U_R = \left[\left(\frac{\partial R}{\partial x_1} U_{x_1} \right)^2 + \left(\frac{\partial R}{\partial x_2} U_{x_2} \right)^2 + ... + \left(\frac{\partial R}{\partial x_n} U_{x_n} \right)^2 \right]^{1/2} \ , \tag{4.4}$$

where $\partial R/\partial x_i$ is the sensitivity coefficient for the result R with respect to the measurement x_i.

4.2 Distillate flux measurements

The distillate flux, D_{flux} (l/m^{2}h), is defined as:

$$D_{flux} = D_{flow}/A_m, \tag{4.5}$$

where A_m, (m^2), is the area of the membrane material used inside the module. D_{flow}, (l/h), is the distillate flow rate, defined as:

$$D_{flow} = \Delta m/\Delta t, \tag{4.6}$$

where Δm is the increase in mass, as measured by the scale and Δt is the time interval between mass measurements. Using equation 4.4, uncertainty in the D_{flux} measurement is calculated as follows:

$$\frac{U_{D_{flux}}}{D_{flux}} = \sqrt{\left(\frac{U_w}{w}\right)^2 + \left(\frac{U_h}{h}\right)^2 + \left(\frac{2 * U_m}{m}\right)^2 + \left(\frac{U_t}{t}\right)^2}, \tag{4.7}$$

where w is the measured width of the membrane, h is the measured height of the membrane, and t is the time interval between mass measurements. M is the mass of the distillate, this error term is multiplied by 2 as distillate flow rate is calculated by measuring the difference between 2 mass measurements.

When the feed temperature at the hot channel inlet was 80°C and the feed flow rate was 1 l/min, the distillate flux was 8.51 l/m^{2}h . The average uncertainty in the distillate flux measurement was 4.49%. A breakdown of the measurements used in calculating D_{flux} and their errors is given in table 4.1.

Parameter	Measurement	Error
Height	0.175 m	5 x 10^{-4} m
Width	0.25m	5 x10^{-4} m
Mass	0.003 kg	1 x 10^{-5} kg
Time	0.16	2.8 x 10^{-5} h

Table 4.1: Measurements and error for D_{flux} calculation

4.3 Distillate conductivity measurements

Electrical conductivity of the distillate was measured using an in-line probe made by Vernier. The signal from the probe was logged to a PC via Go!Link USB sensor interface and LoggerLite software. The probe had a sample rate of 1Hz; these values were averaged over 60 seconds.

The conductivity probe measures the solution's ability to conduct a current between two electrodes. The probe measures conductance, the reciprocal of resistance. Conductance, G, is converted to electrical conductivity, EC, using the following equation:

$$EC = G * k_c \ , \tag{4.8}$$

where k_c is the cell constant, defined as the distance between the electrodes divided by the area of the electrode. Conductivity, EC, can be converted into a value of the solutions salinity, in mg/l, with use of equation 3.1. Electrical conductivity is temperature dependent. During transient operation of the MD module the feed temperature varies; this results in a change in the distillate temperature. In this section the conductivity probe in the distillate outlet line is calibrated over a range of temperatures to determine the extent of this effect.

The conductivity probe must be fully submerged in distillate in order to take a measurement, therefore the probe was placed inside a well fitting. This fitting introduces a delay to the response time of the conductivity readings, as the well is diluted. The response time of the probe, while in the fitting, was investigated and the results are reported in this chapter.

4.3.1 Temperature calibration of the conductivity probe

The conductivity of a solution is temperature dependant. At higher temperatures the solution has greater ionic mobility, which leads to an increase in conductivity [70]. For

a fresh water solution the conductivity is expected to rise by 1.2 - 2% for every 1°C increase in the temperature of the solution [71]. However, the temperature effect is also dependant on the concentration of salts in the solution [72].

The probe was therefore calibrated for a range of temperatures to ensure that changes in the distillate electrical conductivity measurements observed during intermittent and transient operation was not due to a change in distillate temperature. Solutions were prepared using de-ionised water and NaCl, with a range of initial conductivity from 50 to 200 μS/cm at 20°C. The conductivity of each solutions was measured at a range of temperatures from 20 to 60°C.

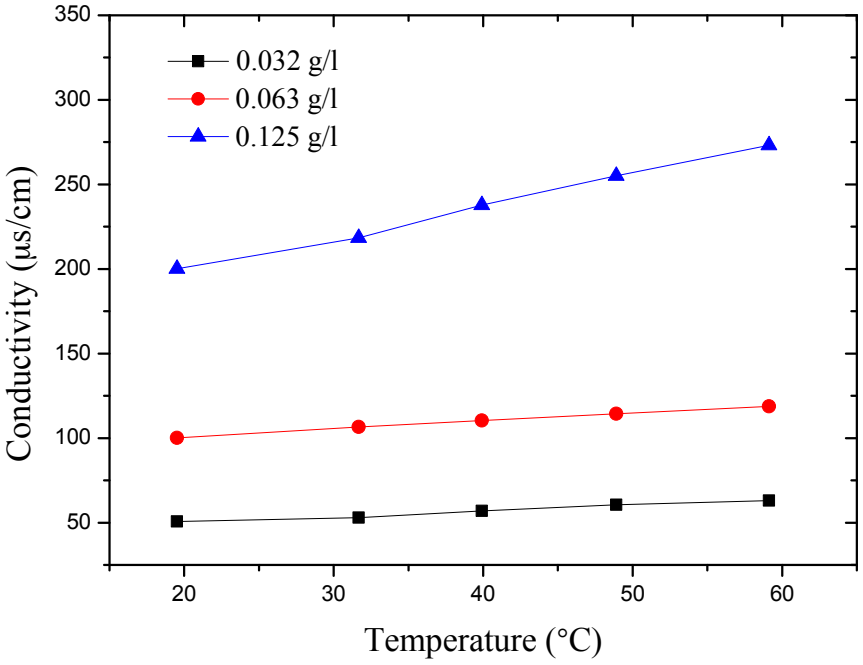

Figure 4.1: Calibration data of the conductivity probe at various temperatures

Three solutions were made with conductivities of 50, 100 and 200 μS/cm at 20°C. This corresponds to a salinity of 0.032, 0.063 and 0.125 g/l, using equation 3.1. Each solution was put in a beaker, which was then placed inside a water bath. The conductivity probe was placed inside the beaker, along with a thermocouple. The

temperature of the water bath was set and time was allowed for the temperature in the beaker to become stable, before a conductivity reading was taken. The temperature of the bath was increased from 20°C to 60 °C and a conductivity measurement was taken for each 10°C increment. The calibration data is shown in figure 4.1. For the solution with an initial conductivity of 100 μS/cm at 20°C, there was a 0.46 μS/cm increase in the conductivity on average for every 1°C temperature increase.

The concentration of NaCl in the solution clearly influences the temperature dependance of the conductivity reading. For the solution with an initial conductivity of 200 μS/cm at 20°C, there was an average increase of 1.8 μS/cm for every 1°C temperature increase. Table 4.2 shows the average increase in conductivity per 1°C for each of the three solutions.

Conductivity at 20°C μS/cm	Δ C per 1°C increase μS/cm °C	Conductivity at 60°C μS/cm
50.7	0.33	63.1
100.2	0.46	118.7
200	1.8	273.2

Table 4.2: Linear coefficients for temperature dependance of conductivity of solutions

The temperature of the distillate is expected to vary during intermittent operation of the MD unit. Figure 4.2 shows the distillate temperature as a function of feed temperature at a constant feed flow rate of 0.6 l/min and constant feed salinity of 35 g/l. The temperature of at the inlet to the cold channel remained at 13.6°C during the experiment.

The minimum distillate temperature observed was 14.1°C, when the feed temperature at the inlet of the hot channel was 40°C. The maximum distillate temperature observed is 16.0°C, when the feed temperature at the inlet of the hot channel was 80°C, the maximum operating temperature of the MD process. This is a range of 1.9°C in distillate temperature. Therefore distillate produced with a conductivity of 200 μS/cm at 14.1°C, would measure 203.4μS/cm at 16.0°C, giving a percentage increase of 1.7%. This error is the result of the greatest change in distillate temperature and the largest

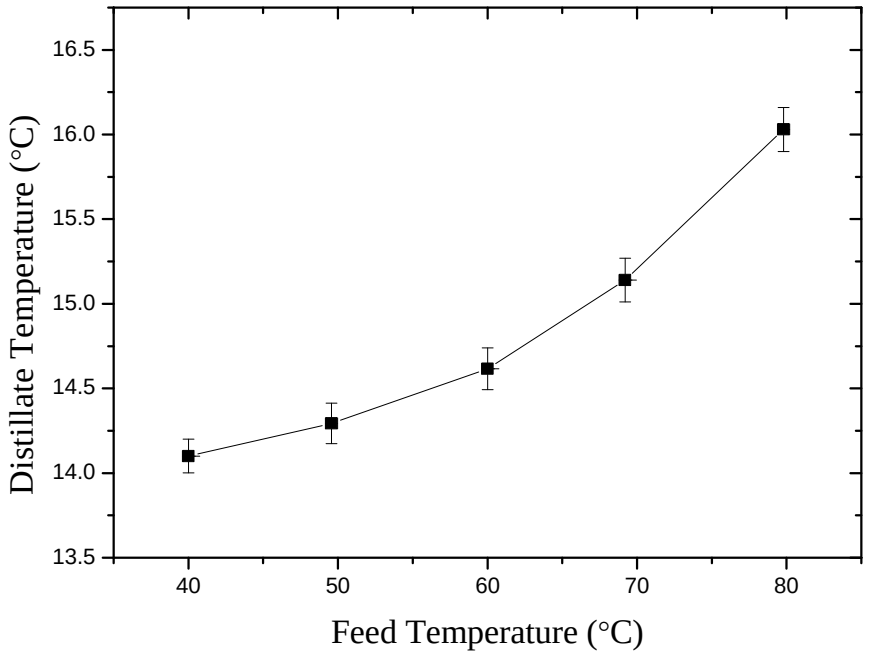

Figure 4.2: Temperature of the distillate against feed temperature

distillate conductivity observed from the system, therefore this error represents the worst case scenario.

4.3.2 Response time calibration

The membrane module used in the experiments is a small lab scale system, with a membrane area of 0.04375 m^2. This relatively small membrane area produces a low distillate flow rate. In order to measure the conductivity of the distillate produced, the eyelet in the probe must be fully submerged. The sensor was therefore placed in a small well fitting with a volume of 18ml. The fitting is shown in figure 4.3.

The distillate pooled in the fitting to allow for a measurement, therefore these measurements are not instantaneous and a delay is introduced due to the necessity to dilute the pool where the sensor is located. In order to ascertain the response time of the measurement a constant flow rate was used and a solution was passed through the

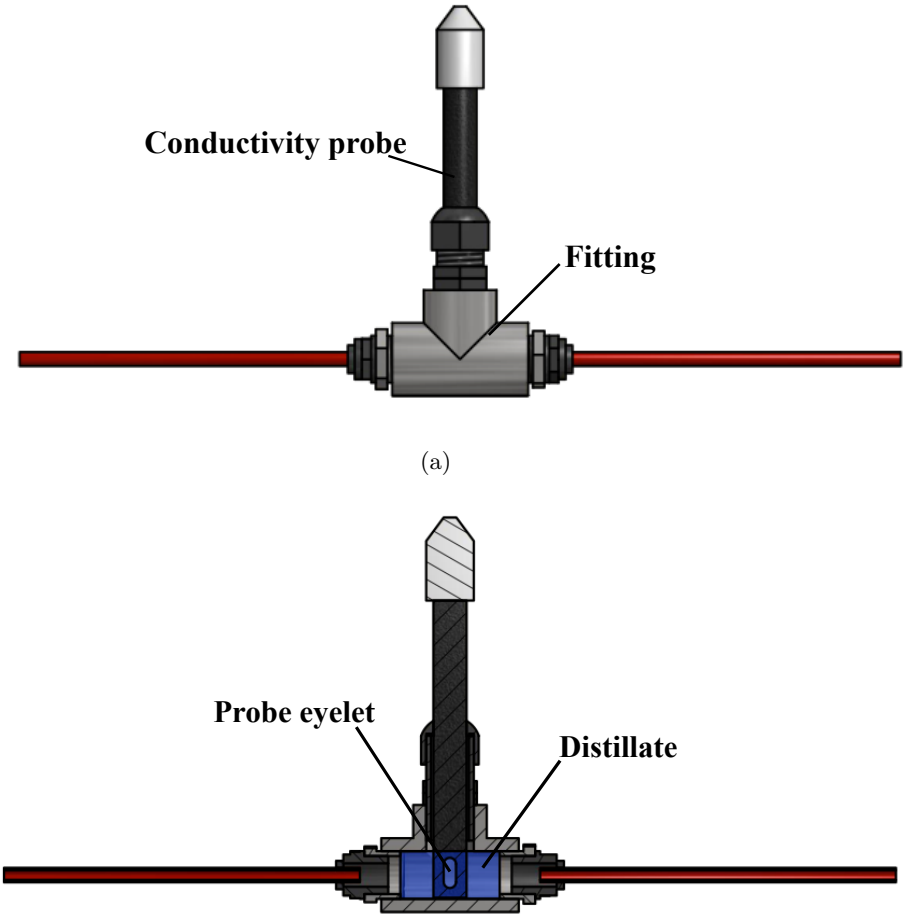

Figure 4.3: a) Diagram of the conductivity probe and well fitting b) cross section view of the probe and fitting

fitting. A step change was then made for a solution with lower conductivity, and the time for the probe measurement to reach the lower conductivity was observed. The constant flow rate used was 0.005 l/m. This is the average distillate flow rate produced when the module is operated at optimum conditions, with feed solution temperature at the inlet of the hot channel of 80°C and a feed flow rate of 0.6 l/min. The initial conductivity of the solutions used ranged from 240 μS/cm to 208 μS/cm. The lower conductivity solution used in each experiment was 205 μS/cm. Figure 4.4 shows time taken for the pool to dilute.

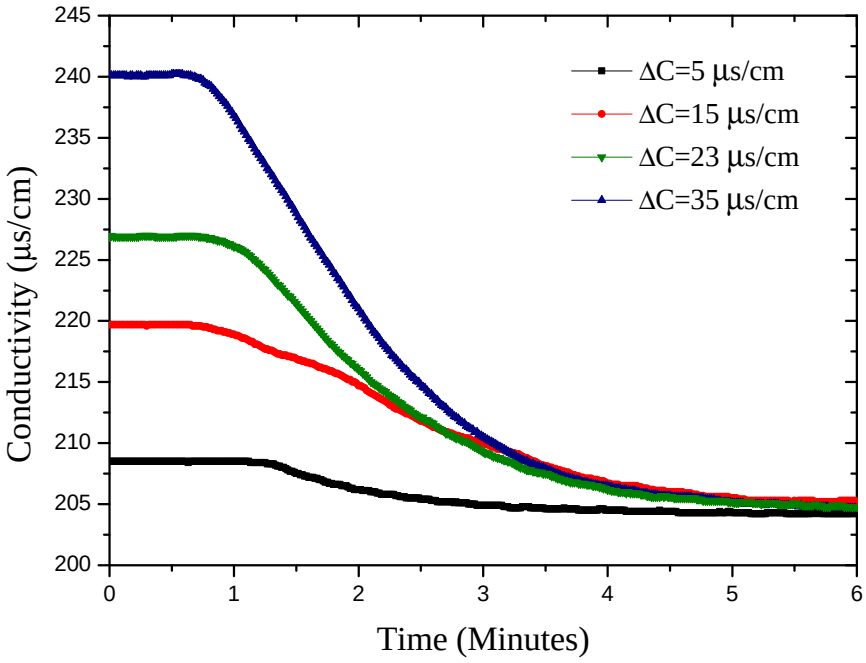

Figure 4.4: Transient response in conductivity measurement, subject to constant flow rate of 0.005l/min, with a step change in inlet concentration

T_{90-10} is the time taken for the measurement to fall from 90% to 10% of the total change in the value. T_{90-10} of the conductivity measurement in these experiments was found to be 156 seconds.

A series of experiments were then performed for a constant initial and final solution conductivity but a range of flow rates. The range of flow rates was varied between 0.003 l/min and 0.006 l/m. A solution with a conductivity of 220 μS/cm was fed through the fitting, until it was full. A solution with a conductivity of 205 μS/cm was then fed through the fitting and the length of time for the conductivity to decrease was observed; the results are shown in figure 4.5. T_{90-10} varied between 150 seconds and 360 seconds.

The response times ascertained from these experiments were used to interpret results for the performance of the MD module during intermittent and transient operation.

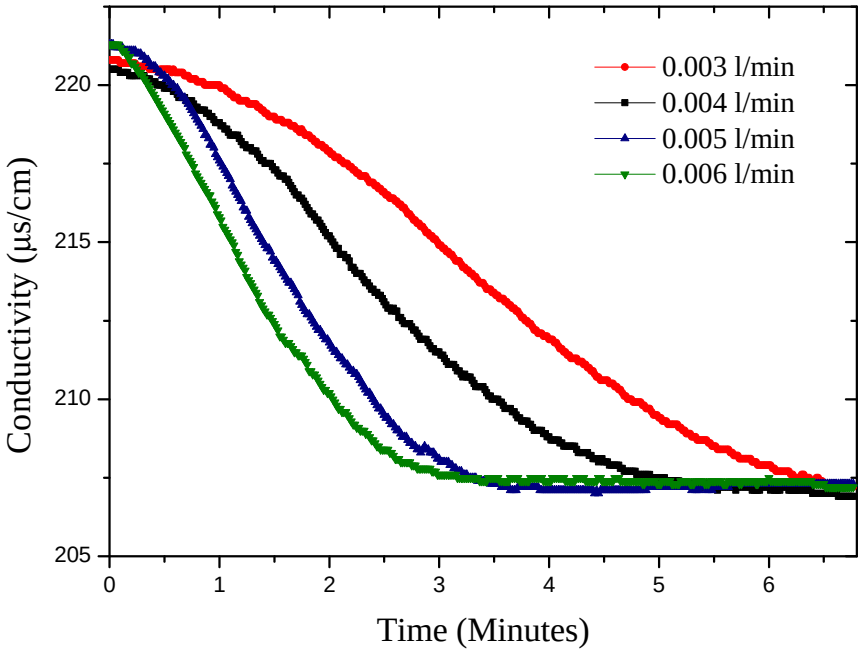

Figure 4.5: Time taken for fitting to dilute, constant C, varying flow rates.

4.4 Temperature measurements

Thermocouples were used to take temperature measurements of the feed stream at various points throughout the rig: the cold channel inlet, the cold channel outlet, the hot channel inlet and the hot channel outlet as shown in figure 3.5. The thermocouples used were manufactured by TC direct and are mineral insulated T-type thermocouples with a pot seal. The T-type thermocouple has a measurement temperature range from 0°C - 400°C. The accuracy stated by the manufacturer is 1%.

To calibrate the thermocouples they were submerged into a water bath. The bath is fitted with a PT1000 platinum resistance temperature detector, RTD, made by Omega. The sensor has high accuracy therefore it was used as a reference to set the bath temperature. The uncertainty in this measurement is 0.1°C at 100°C, as stated by the manufacturer. The temperature of the bath was varied from 20°C to 100°C.

The calibration data for the thermocouple located at the inlet of the cold channel is shown in figure 4.6. The trend line is applied to the calibration data.

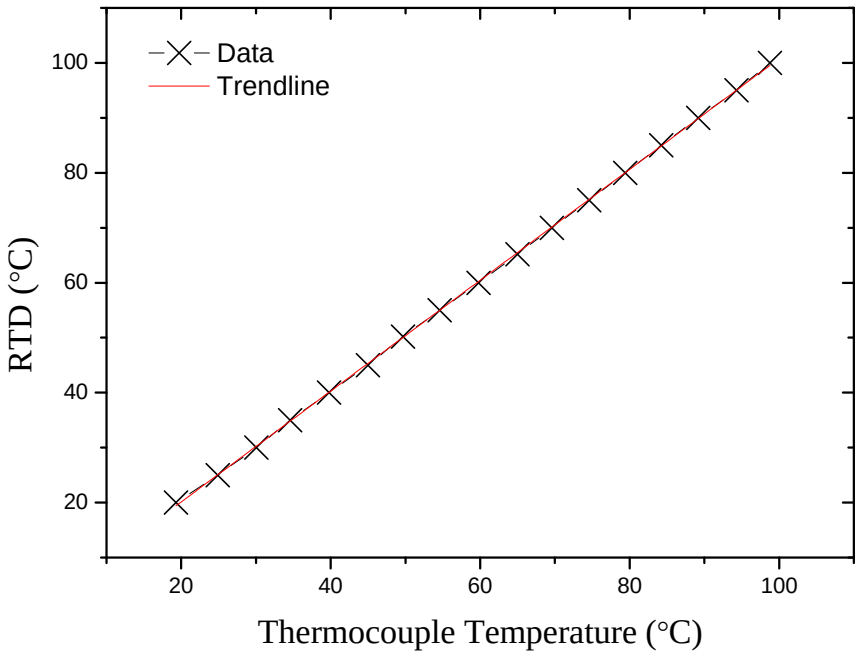

Figure 4.6: Cold channel inlet thermocouple calibration data

When the relationship between two data sets is perfectly linear, the true value of y can be predicted for a known value of x using the following equation:

$$\tilde{y} = A + Bx \ , \tag{4.9}$$

However when a data set does not display a perfect linear relationship the values of A and B are determined as those values which minimise the sum squared deviation of the observed values. This is known as the least-squares fit method and linear fit is known as the regression line, which is defined as [73]:

$$\hat{y} = a + bx \ , \tag{4.10}$$

The values of a and b may not predict the observed value of y, however $\hat{y}$ is an average for all such observed values. A linear regression is fit to the calibration data of the cold channel inlet thermocouple in figure 4.6 and the equation for the regression line is found to be:

$$T_{RTD} = 1.003 T_{cold,in} - 0.065 \ , \tag{4.11}$$

There is an inherent uncertainty in the linear regression line; this is defined as [73]:

$$U_{regression} = \hat{y} - \tilde{y} = S_{xy} t_{N-2;\alpha/2} \left[\frac{1}{N} + \frac{(x_0 - \overline{x})^2}{\sum_{i=1}^{N} (x_i - \overline{x})^2} \right]^{1/2} \ , \tag{4.12}$$

where $t_{N-2;\alpha/2}$ is a factor determined by the Student t Probability Distribution, dependant on the number of samples in the data set and the confidence level predicted. In this instance $t_{N-2;\alpha/2} = 2.110$ for a 95% confidence interval. x_0 is defined as a chosen value within the range of the calibration data. $\overline{x}$ and $\overline{y}$ are the mean of the respective x and y components of the data. The uncertainty in the linear regression is larger for values at the extreme of the data set. Data corresponding to 80°C was used as the arbitrary value of x_0, as this is the maximum operating temperature of the MD process. In this instance $U_{regression}$ was found to be 0.068% within a 95% confidence limit.

The standard deviation, $S_{y|x}$, of the observed values of y_i in the sample about their associated linear regression, $\hat{y}_i$= a + bx, can be calculated as follows,[73]:

$$S_{y|x} = \left[\frac{\sum_{i=1}^{N} (y_i - \hat{y}_i)^2}{N - 2} \right]^{1/2} \tag{4.13}$$

This can be expressed in terms of the mean values, $\overline{x}$ and $\overline{y}$, as follows:

$$S_{y|x} = \left[\frac{1}{N-2} \left(\sum_{i=1}^{N} (y_i - \overline{y})^2 - \frac{\left(\sum_{i=1}^{N} x_i y_i - N\overline{xy} \right)^2}{\sum_{i=1}^{N} (x_i - \overline{x})^2} \right) \right]^{1/2} \tag{4.14}$$

To report this error with a 95% confidence level, the uncertainty in the measurement is the standard deviation times the Student t Distribution factor, $t_{N-2;\alpha/2}$. Therefore $U_{measurement}$ is expressed as [65]:

$$U_{measurement} = t_{N-2;\alpha/2} * S_{y|x} \tag{4.15}$$

Again, for this data set $t_{N-2;\alpha/2} = 2.110$.

The uncertainty in the measurement, $U_{measurement}$ of the calibration data for the thermocouple located at inlet of the cold channel was calculated as 0.206%. The total uncertainty in the thermocouple measurement is defined as:

$$U_{total} = U_{measurement} * U_{regression} \tag{4.16}$$

Therefore the total uncertainty for cold channel inlet thermocouple measurement is ± 0.274%

The total uncertainty was calculated for the remaining three thermocouples, at the cold channel outlet, the hot channel inlet and the hot channel outlet. The calibration data for the three thermocouples is shown in figure 4.7.

A linear regression is fit to the calibration data for the cold channel outlet and is shown in equation 4.17.

$$T_{RTD} = 1.003 T_{cold,out} - 0.234 \tag{4.17}$$

The uncertainty in the linear regression, $U_{regression}$, corresponding to 80°C was found to be 0.075%. The uncertainty in the measurement, $U_{measurement}$ of the

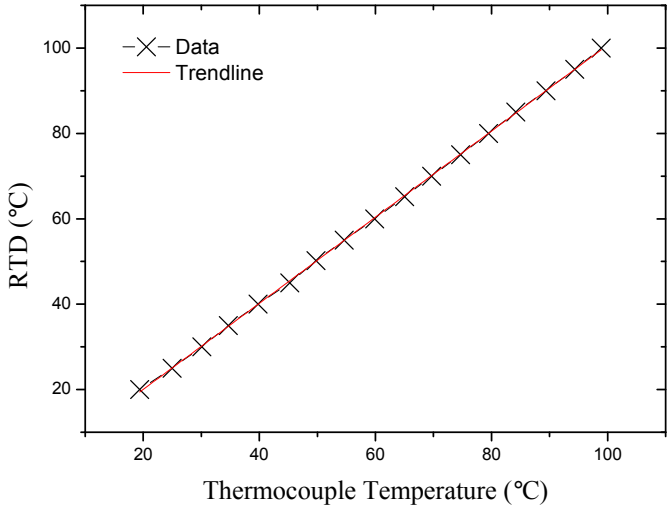

(a) Cold channel outlet thermocouple

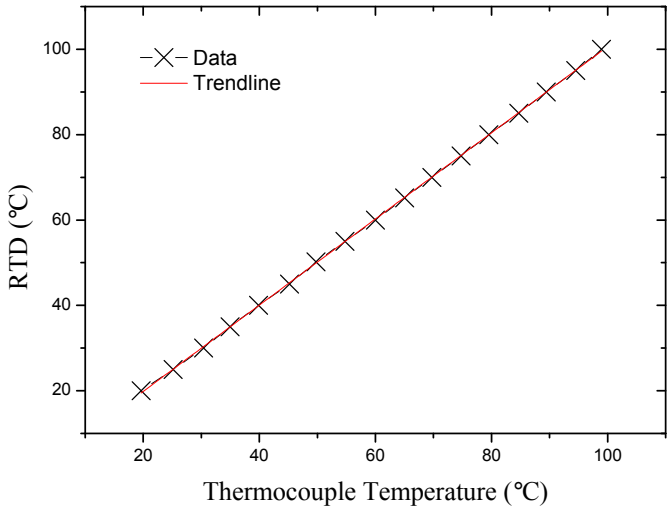

(b) Hot channel inlet thermocouple

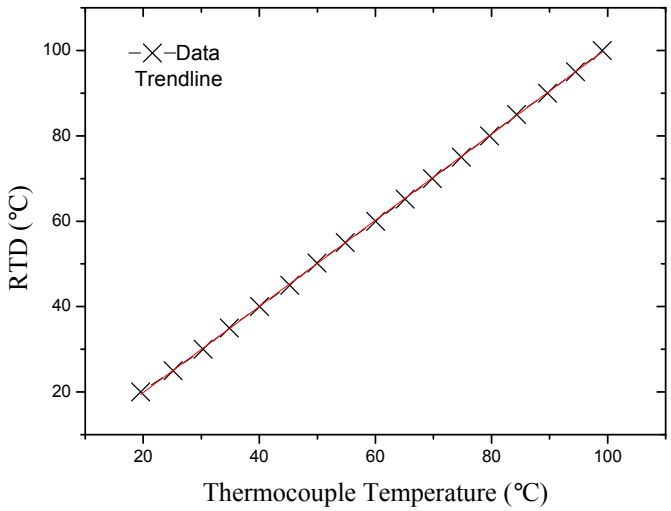

(c) Hot channel outlet thermocouple

Figure 4.7: Calibration data for the cold channel outlet, the hot channel inlet and the hot channel outlet .

calibration data for the thermocouple located at outlet of the cold channel was calculated as 0.227%.

A linear regression was fitted to the calibration data for the hot channel inlet and is shown in equation 4.18. The uncertainty in the linear regression $U_{regression}$, corresponding to 80°C was found to be 0.077%. The uncertainty in the measurement, $U_{measurement}$ was calculated as 0.234%.

$$T_{RTD} = 1.004T_{hot,in} - 0.099 \tag{4.18}$$

Equation 4.19 shows the linear regression fit for the thermocouple at the outlet of the hot channel. The uncertainty in the linear regression, $U_{regression}$, corresponding to 80°C was found to be 0.069%. The uncertainty in the measurement, $U_{measurement}$ of the calibration data for the thermocouple located at outlet of the hot channel was calculated as 0.210%.

$$T_{RTD} = 1.0015T_{hot,out} - 0.162 \tag{4.19}$$

A summary of the uncertainty measurements for all four of the thermocouples in the system are shown in table 4.3.

Temperature Measurement	Regression Uncertainty (%)	Measurement Uncertainty (%)
Cold channel inlet	0.068	0.206
Cold channel outlet	0.075	0.227
Hot channel inlet	0.077	0.234
Hot channel outlet	0.069	0.210

Table 4.3: Uncertainties in the temperature measurements

4.5 Summary

The procedures for calibrating the sensors used in the measurements are discussed. This chapter also outlines the uncertainty in the measurements taken, with 95% confidence. These uncertainty values will be used to interpret the significant of the results presented throughout this thesis.

Chapter 5

Steady state performance of a bench scale membrane distillation system

---

In this chapter the performance of a bench scale MD system is explored while operating under steady state conditions. During these experiments the feed salinity was maintained at a constant level of 35 g/l (a standard salinity used in lab experiments), while the feed temperature and flow rate were varied, to determine their effect on the distillate flux produced by the module. After any changes were made to these parameters, the distillate output was monitored and time was allowed for these

values to stabilise, so that the system could be considered in steady state before any measurements were taken.

An investigation was carried out to determine the effect of membrane pore size on the steady state performance of the module. Two membranes were tested, both manufactured by Gore^{TM}. G02 had an average pore size of 0.2 μm and G04 had an average pore size of 0.45 μm. The influence of pore size on distillate flux and distillate conductivity was examined and the results of this investigation are reported below.

A description of a mathematical model for distillate output from the MD module is given. The model uses a 1-Dimensional energy balance to calculate the temperature profile across the membrane module for various feed flow rates and feed temperatures. From this, mass transfer across the membrane can be predicted. A comparison was made between the experimental data and the output from this model.

5.1 Experimental characterisation of the MD unit performance

Figure 5.1 shows the distillate flux from the module against inlet feed temperature for flow rates from 0.2-1.0 l/min. The distillate output increased as the feed temperature increased, the relationship between the two is exponential. This is due to an exponential increase in the vapour pressure of the feed solution with temperature [8]. This in turn leads to an exponential increase in the transmembrane vapour gradient, which provides the driving force for mass flux across the membrane [9].

At a constant feed flow rate of 0.8 l/min, when the feed temperature increased from 52°C to 78°C the distillate flux increased by 74%. A maximum distillate flux of 7.3 l/m^{2}h was recorded, this corresponded with a feed flow rate of 1.0 l/min and a feed temperature at the hot inlet of 74.7 °C. An increase in distillate flow rate is also seen for higher feed flow rates, however, this parameter does not effect the output to the same extent.

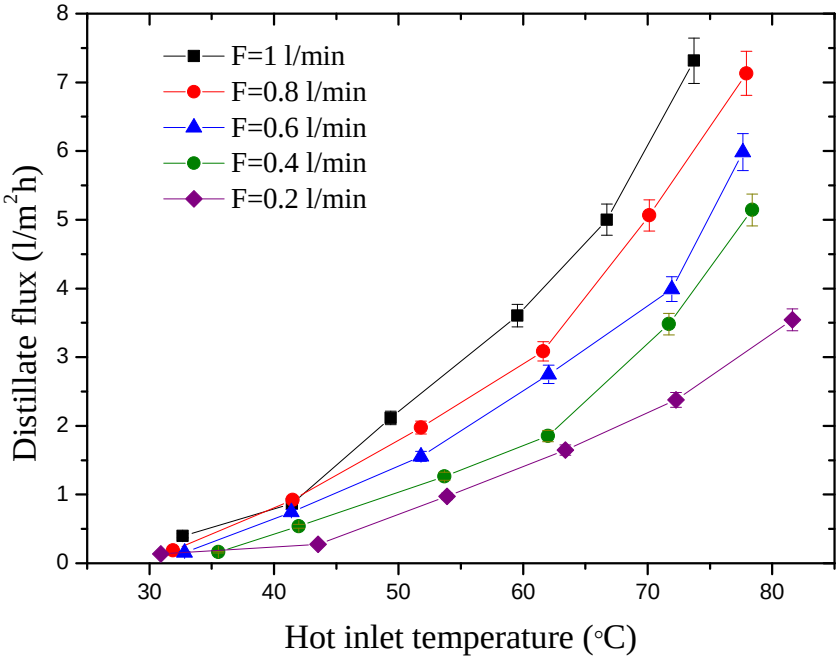

Figure 5.1: Distillate flux against inlet feed temperature in hot channel for a range of flow rates

Figure 5.2 further explored the relationship between feed flow rate and distillate flux. The distillate flux is shown as a function of feed flow rate, for fixed feed temperatures of 60, 70, and 80 °C. The distillate flux shows a linear relationship with feed flow rate, these finding are in agreement with several other MD studies [74, 75, 11, 22]. A maximum distillate flux of 8.5 l/m^{2}h was recorded when the feed flow rate was 1.0 l/min and the feed temperature was 80 °C. At a constant feed temperature of rate of 80°C, when the flow rate was increased by 50% from 0.4 l/min to 0.8 l/min, the distillate flux increased by 29%. Again, the strong dependance of distillate flux on feed temperature is apparent in this figure.

As mentioned earlier, driving force for mass flux in the MD process is the vapour pressure difference across the membrane. The pressure in the channels either side of the membrane is a function of the temperature of the solution in the channel. The

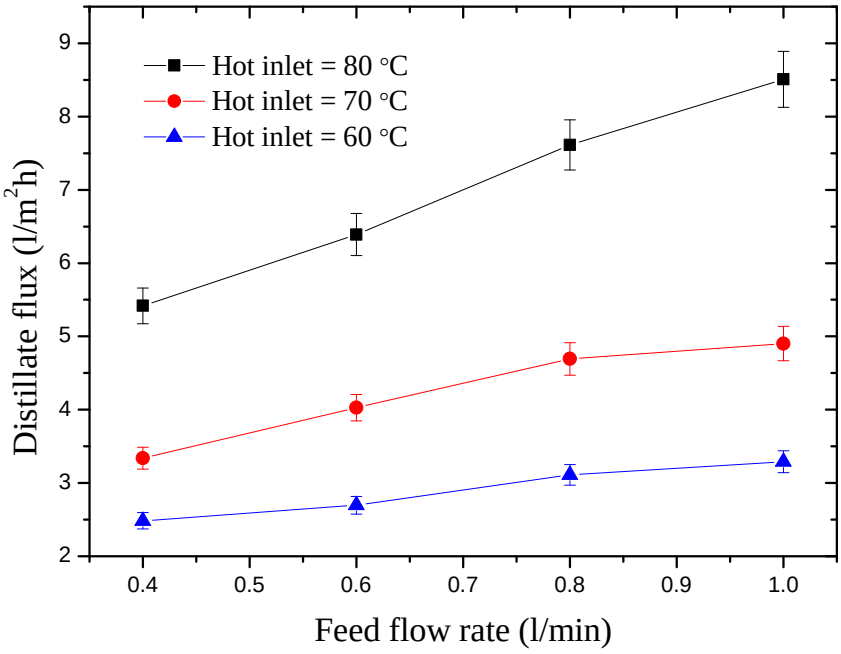

Figure 5.2: Distillate flux against flow rate for a range of inlet temperatures in the hot channel

transmembrane temperature was calculated as follows;

$$\Delta T_{membrane} = \left(\frac{T_{hot,in} + T_{hot,out}}{2}\right) - \left(\frac{T_{cold,in} + T_{cold,out}}{2}\right) , \tag{5.1}$$

where $T_{hot,in}$ and $T_{hot,out}$ are the temperatures at the inlet and outlet of the hot channel and $T_{cold,in}$ and $T_{cold,out}$ are the temperatures at the inlet and outlet of the cold channel. Figure 5.3 shows the temperature difference, $\Delta T_{membrane}$, against the feed flow rate for various feed temperatures. Figure 5.3 shows an increase in the value of $\Delta T_{membrane}$ for higher inlet feed temperatures. The results also shows a slight increase in $\Delta T_{membrane}$ for increased feed flow rate.

From the temperature measurements a value of pressure can be obtained by use of the Antoine Equation, which is expressed as [9]:

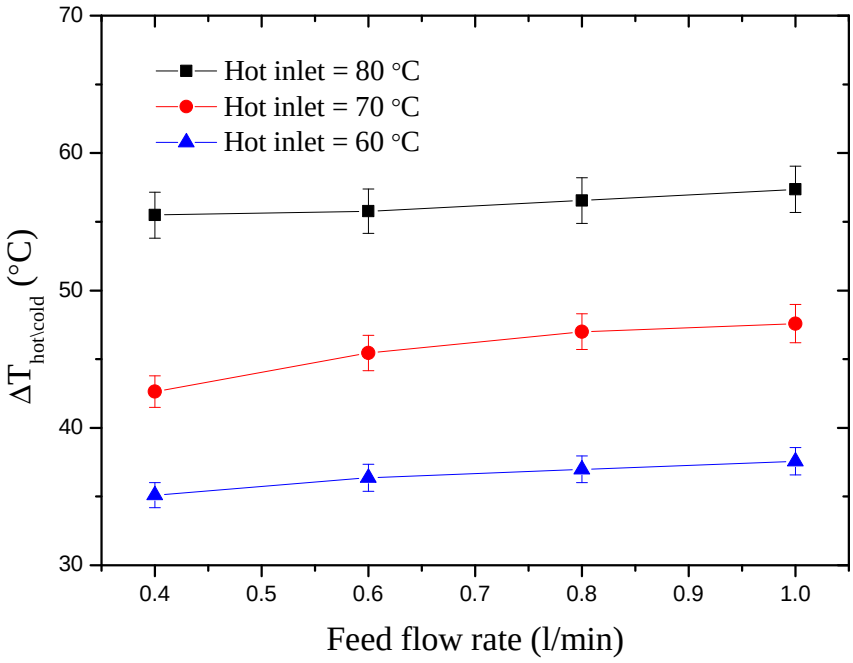

Figure 5.3: Temperature difference across the membrane against flow rate for a range of hot inlet temperatures

$$log_{10}P = A - \frac{B}{C+T} \ , \tag{5.2}$$

where T is temperature (°C). A, B and C are component specific constants, with values of 8.071, 1730.63, 233.426, respectively, for water within the temperature range of 1-100 °C [22]. With this equation the value of pressure was determined at various points throughout the system and a value for the average trans-membrane pressure, $\Delta P_{membrane}$, was calculated.

Figure 5.4 shows the pressure difference across the membrane against feed flow rate for inlet feed temperatures of 60, 70 and 80 °C. As expected it shows an increase in the value of $\Delta P_{membrane}$ for higher inlet feed temperatures. It also shows a slight increase in $\Delta P_{membrane}$ for increased feed flow rate.

The Specific Energy Consumption, SEC, of the module is defined as the thermal

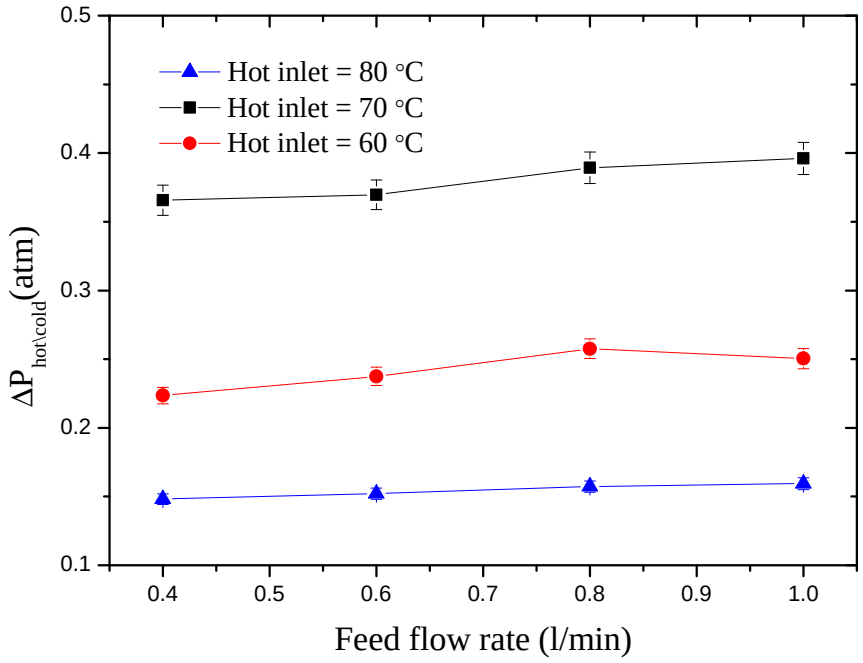

Figure 5.4: Pressure difference across the membrane against flow rate for a range of inlet temperatures of the hot channel

energy consumption of the system (kWh), divided by the distillate flux (kg), and is calculated as follows [11]:

$$SEC = \frac{\dot{m}_{feed} C_p (T_{hot,in} - T_{cold,out})}{f_{dist}} \ , \tag{5.3}$$

where C_p is the specific heat capacity of water, $\dot{m}$ is the mass flow rate of the feed solution, $T_{cold,out}$ is the outlet temperature of the cold channel and $T_{hot,in}$ is the inlet temperature of the hot channel and f_{dist} is the distillate output.

Figure 5.5 shows the SEC of the module as a function of feed flow rate, for feed temperatures of 60, 70 and 80 °C. The SEC increases with higher feed flow rates, therefore the increase in $\dot{m}_{feed}$ is not compensated for by the resulting rise in the f_{dist}. The SEC decreases with an increase in the hot inlet feed temperature, as the rise in thermal energy input and the subsequent increase in the value of $(T_{hot,in} - T_{cold,out})$

is outweighed by the increase in distillate produced. A maximum SEC value of 20 kWh/kg was recorded; this corresponds to the highest flow rate of 1.0 l/min and the lowest inlet feed temperature of 60 °C measured. Conversely, the lowest SEC value observed, 6.8 kWh/kg, was for the for the minimum feed flow rate of 0.4 l/min and the highest inlet feed temperature tested of 80 °C.

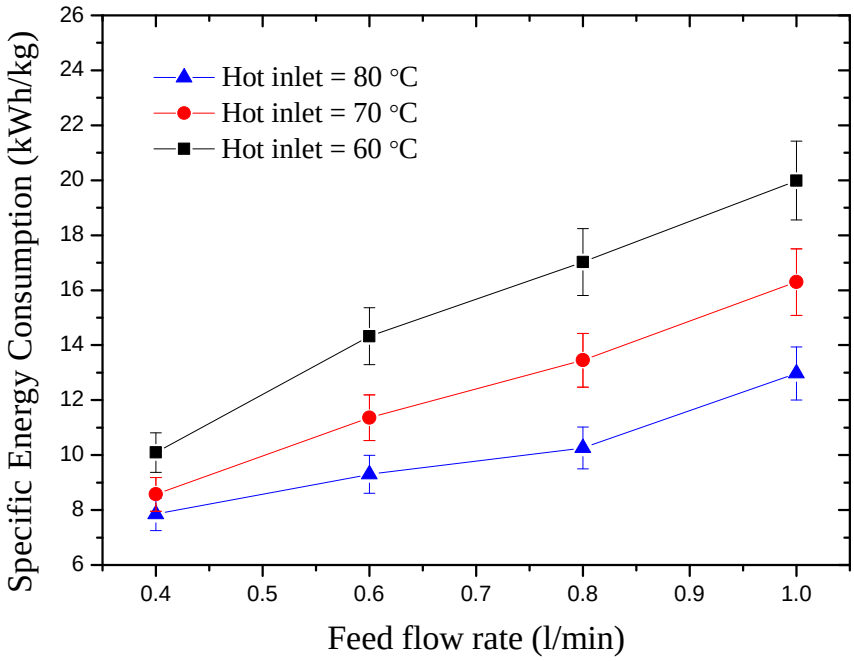

Figure 5.5: Influence of feed flow rate on specific energy consumption for a range of hot inlet temperatures

The SEC of larger MD modules are often lower than the values reported here, this is because they make use of spiral wound or hollow tube membrane configurations. This increases the surface area of membrane within a module and therefore gives a greater distillate yield, making the module more thermally efficient [76]. However higher SEC is to be expected when dealing with small bench scale systems due to the comparably lower membrane surface areas used. The results reported in this chapter are comparable with those reported from similar bench scale systems [22].

Figure 5.6 shows the distillate flux as a function of the vapour pressure difference across the membrane, for feed flow rates of 0.4 l/min - 1.0 l/min. A clear improvement in the distillate output is seen for higher feed flow rates, despite having similar Δ P values. This could be the result of improved mixing within the channels at higher flow rates. It is preferable to have a turbulent flow regime in the channels, as mixing results in higher heat transfer to the membrane surface from the bulk stream, therefore reducing temperature polarisation effect [9, 77].

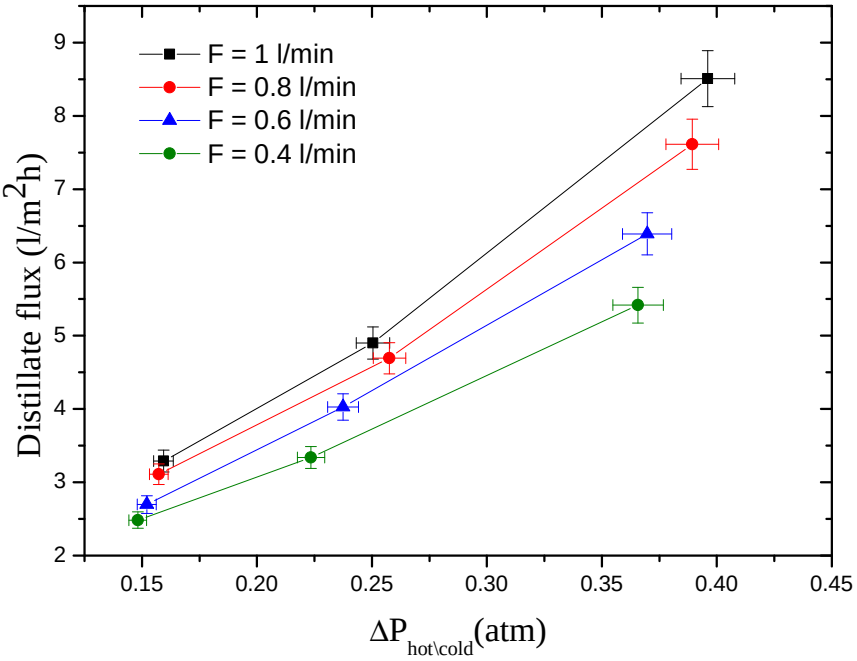

Figure 5.6: Distillate flux against pressure difference across the membrane for a range of feed flow rates

Figure 5.7 shows the conductivity of the distillate produced as a function of feed temperature for the range of feed flow rates tested. The results show an decrease in distillate conductivity with increases in feed temperature. This is believed to be the result of a change in the microstructure of the membrane pores at higher operating temperatures. This theory is explored further in chapter 6.

When the module was operated with a feed flow rate of 0.6 l/min and feed inlet temperature of 80°C, the conductivity recorded was 3.7 μs/cm. Given that the feed solution had a constant conductivity of 54,000μs/cm, this gives a salt retention of 99.994%.

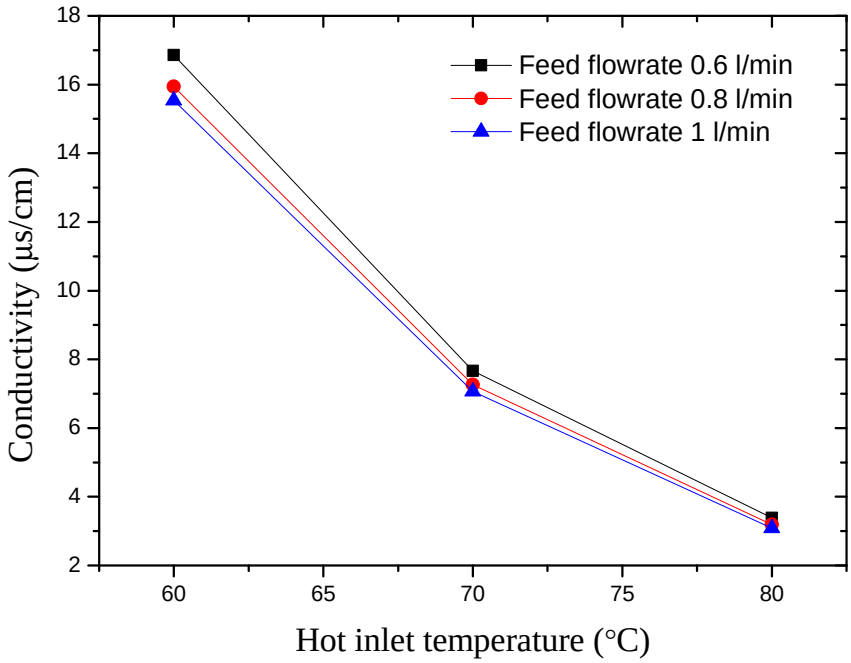

Figure 5.7: Distillate conductivity against feed temperature for a range of feed flow rates

However, it can also be seen from Figure 5.7 that the distillate conductivity is not strongly influenced by flow rate. This suggests that there is no presence of a leak in the system, as higher feed flow rates would increase the hydraulic pressure in the channels, increasing the volume of leaked feed water, this would be apparent in the values of conductivity.

The values for pressure drop across the system are shown in figure 5.8 as a function of feed flow rate. The pressure drop results from the loss of power in the module due to friction, and therefore this value should be kept low. The pressure of feed going into the

module was measured by a digital manometer. The feed then passes through the cold channel, the heating coil and the hot channel. The feed exiting the hot channel is open to the atmosphere. Therefore the pressure drop is the difference between inlet pressure and atmospheric pressure. The pressure drop increases with increased feed flow rate, the relationship between the two is exponential. This is expected as head loss due to friction is dependant on a power law relationship with the fluid velocity [22].

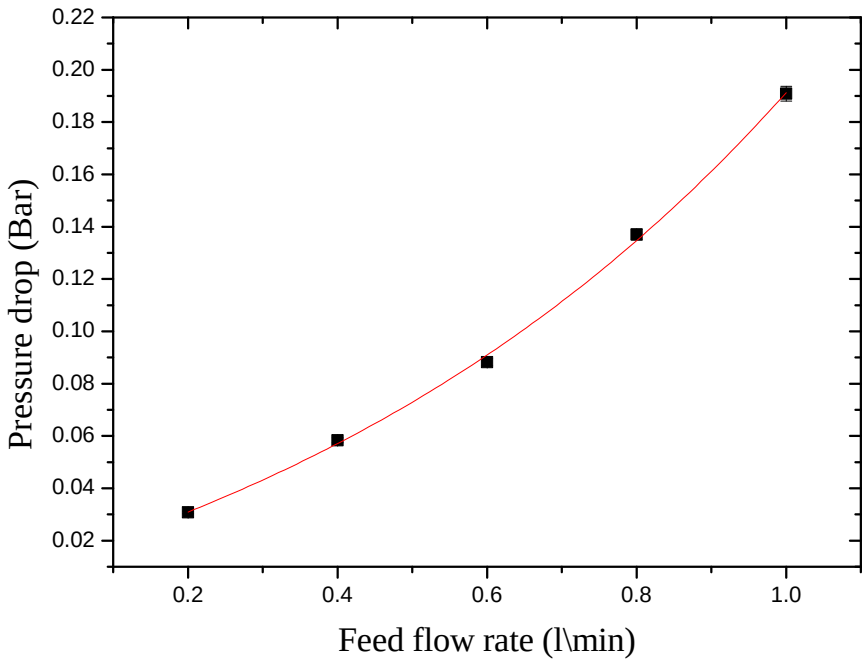

Figure 5.8: Pressure drop across the MD module as a function of feed flow rate

5.2 Effects of membrane pore size

In this section a comparison is made between the performance of two membranes, G02 and G04, both manufactured by Gore^{TM}. G02 has an average pore size of 0.2 μm and G04 has an average pore size of 0.45 μm, as stated by the manufacturer. Further details on the properties of these two membranes are given in table 3.1.

Figure 5.9 shows the distillate flux against feed temperature for the two different membranes, G02 and G04. Both membranes were tested with a feed flow rate of 0.6 l/min. The distillate flux from G04 membrane was consistently larger than the GO2 membrane. When both membranes where operated at 80°C the distillate flux from G04 was 11% higher than G02. This result is in agreement with a similar study conducted by Cath et al [26], when comparing the flux of PTFE membranes with a pore size of 0.22μm and 0.45μm.

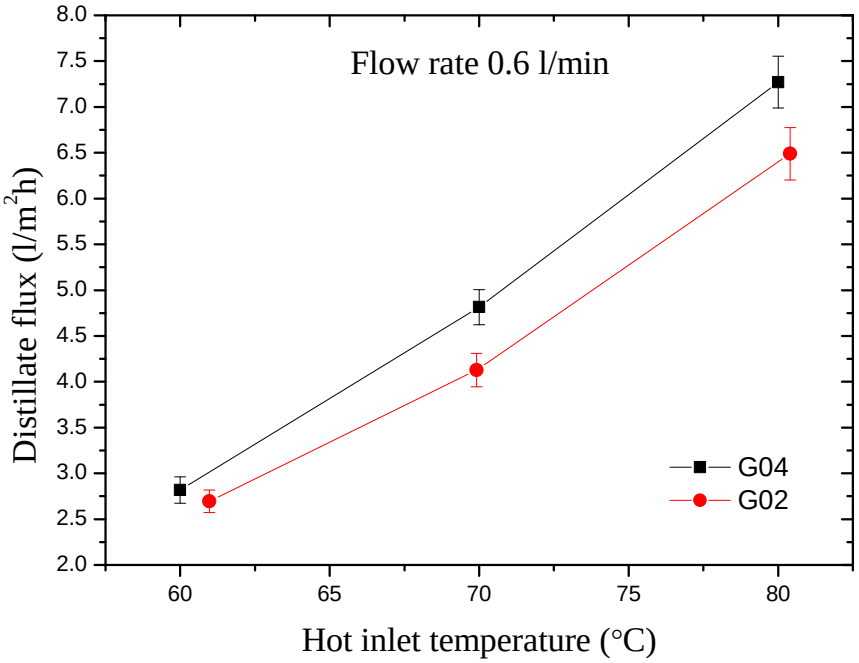

Figure 5.9: Distillate flux against inlet feed temperature for both G02 and G04 membrane

This effect is attributed to the larger mean pore size in the G04 membrane resulting in greater mass transfer. It has been suggested that the mass transfer mechanism shifts from a predominately Knudsen diffusion effect to a Knudsen-Viscous transport process for larger pores. This increases permeability and therefore results in a higher mass flux [9, 78].

Figure 5.10 shows the distillate conductivity as a function of feed temperature, with a feed flow rate of 0.6 l/min for the G04 and G02 membranes. The values of distillate conductivity are higher for the G04 membrane than the G02 membrane. Higher conductivity is expected for the G04 membrane, as larger pores leads to a decrease in Liquid Entry Pressure, LEP, of the membrane [26]. This increases the likelihood of the highly saline feed liquid passing through the pores and entering the distillate.

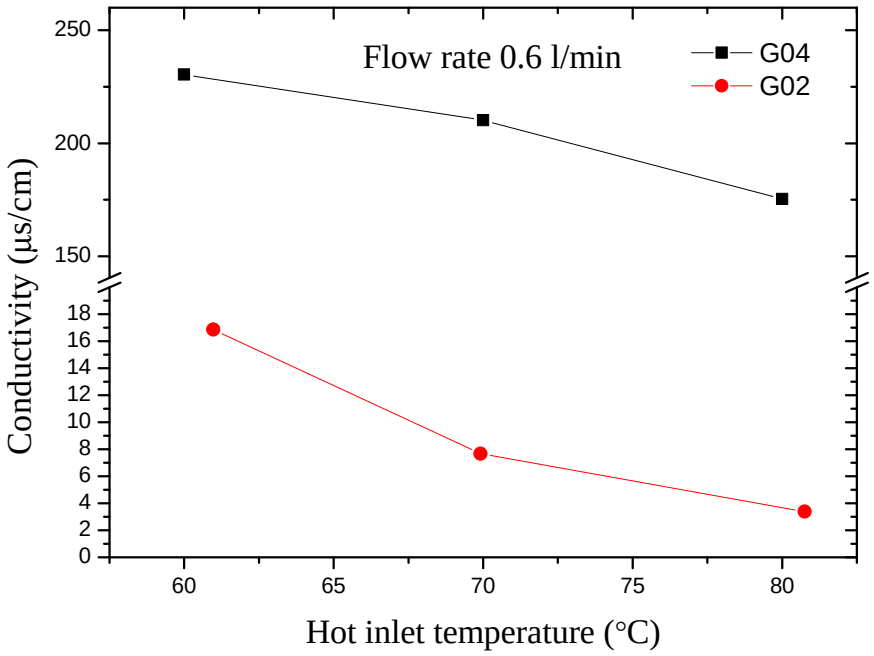

Figure 5.10: Distillate conductivity against inlet feed temperature for a feed flow rate of 0.6l/min, for both G02 and G04 membranes

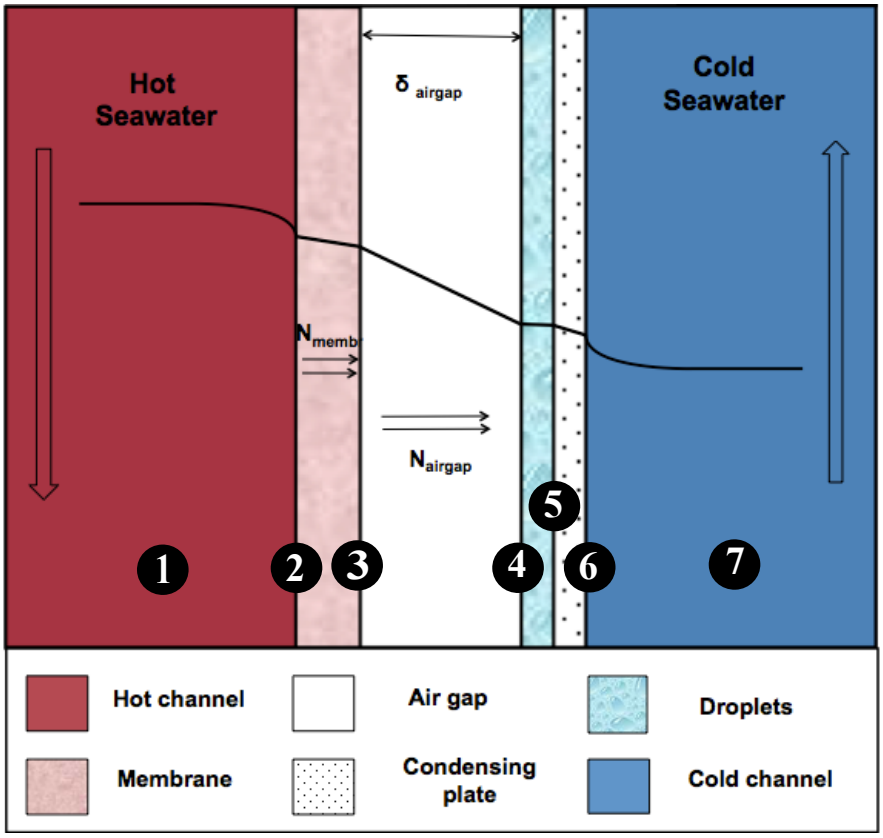

Figure 5.11: Cross sectional profile through the membrane module, showing the temperature gradient through the various layers

5.3 Validating experimental data with a mathematical model

5.3.1 The mathematical model

The schematic diagram in figure 5.11 shows the temperature profile across the many interfaces of the membrane module, if a one dimensional analysis of the heat flux in the direction perpendicular to the surface of the membrane is considered.

There are several stages between the hot and cold channels; the interfaces are numbered in 5.11. Each of these interfaces has a corresponding temperature, these temperatures are named and a full description of their location is given in table 5.1.

The various heat flux rates through these stages were considered and a series of heat

Number	Name	Location
1	$T_{hot,bulk}$	The bulk stream of the hot channel
2	$T_{hot,mem}$	The interface of the hot channel and the membrane
3	$T_{mem,air}$	The interface of the membrane and air gap
4	$T_{air,droplet}$	The interface with the air gap and the droplets
5	$T_{droplet,film}$	The interface of the droplets and the cooling film
6	$T_{film,cold}$	The interface if the cooling film and the cold channel
7	$T_{cold,bulk}$	The bulk stream of the cold channel

Table 5.1: Location and description of the interfaces within the MD module

transfer equations were used to determine the temperature profile across the system; this model was developed by A. Cipollina et al, [22]. With this information it is possible to determine the volume of distillate produced and the mass flux across the membrane, for various operating conditions.

Firstly, we consider the energy available in the bulk cold and hot streams. Assuming that heat loss to the environment is negligible, the heat flux expressed in terms of $\mathrm{W/m^2}$ for the bulk stream of feed in the cold channel and hot channel can be defined as:

$$Q_c = \frac{\dot{m}_{feed} C_p (T_{cold,in} - T_{cold,out})}{A_m} \ , \tag{5.4}$$

and

$$Q_h = \frac{\dot{m}_{feed} C_p (T_{hot,in} - T_{hot,out})}{A_m} \tag{5.5}$$

Where $\mathrm{T}_{cold,in}$ and $\mathrm{T}_{cold,out}$ are the inlet and outlet temperatures for the cold channel and $\mathrm{T}_{hot,in}$ and $\mathrm{T}_{hot,out}$ are inlet and outlet temperatures of the hot channel. $\dot{m}_{feed}$ is the mass flow rate of the feed solution, the distillate flow can be considered

negligible, so this is taken to be the same in both channels. C_p is the specific heat capacity of water, known to be 4.2kJ/kgK.

Heat transfer from the hot bulk stream to the membrane surface, through what is known is the polarisation layer, can be described as:

$$Q_{polarisation,hot} = h_{hot}(T_{hot,bulk} - T_{hot,mem}) \tag{5.6}$$

Where h_{hot} is the heat transfer coefficient between the bulk stream and the membrane surface. A high rate of heat transfer is needed to compensate for the temperature drop caused by the polarisation effect, therefore h_{hot} should be as high as possible.

Heat flux across the membrane is a function of the transport of latent heat with the vapour flux N_{vap} and the conductive heat flow through the membrane and fluid filled pores. The heat flux across the membrane is given as:

$$Q_{membrane} = N_{vap}\lambda + h_{membrane}(T_{hot,mem} - T_{mem,air}) \tag{5.7}$$

where N_{vap} is the vapour flux, λ is the latent heat of vaporisation, and $h_{membrane}$ is the heat transfer coefficient of the membrane. The heat transfer coefficient of the membrane, $h_{membrane}$, can be calculated by considering conduction through both the membrane material and the air within the pores of the membrane, expressed as:

$$h_{membrane} = \frac{(\phi k_{vapour}) + ((1-\phi)k_{membrane})}{\delta_{membrane}} \ , \tag{5.8}$$

where ϕ is the porosity of the membrane, $\delta_{membrane}$ is the thickness of the membrane, k_{vapour} is the thermal conductivity of the vapour and $k_{membrane}$ is the thermal conductivity of the membrane.

Heat flux is transferred across the air gap by latent heat of vaporisation, conduction and convection. However the effects of convective transfer can be considered negligible

for low Reynolds numbers. The heat flux across the air gap is expressed as:

$$Q_{airgap} = N_{vap}\lambda + h_{airgap}(T_{mem,air} - T_{air,droplet}) \tag{5.9}$$

The heat transfer coefficient of the air-gap, h_{airgap}, is expressed as:

$$h_{airgap} = \frac{k_{vapour}}{\delta_{airgap}} \tag{5.10}$$

where δ_{airgap} is the thickness of the air gap.

The heat flux in the condensation of droplets on the cooling film is expressed as:

$$Q_{droplets} = h_{droplets}(T_{air,droplet} - T_{droplet,film}) \tag{5.11}$$

The heat flux through the cooling film is expressed as:

$$Q_{coolingflim} = \frac{h_{film}}{\delta_{film}}(T_{film,cold} - T_{cold,bulk}) \ , \tag{5.12}$$

where δ_{film} is the thickness of the cooling film.

Heat flux from the membrane surface to the cold channel is given as:

$$Q_{polarization,cold} = h_{cold}(T_{droplet,film} - T_{film,cold}) \tag{5.13}$$

The heat transfer coefficients for the polarisation layers in both the hot and cold channels are calculated using the correlation [79]:

$$h = 0.26Re^{0.65}Pr^{0.4}(\frac{k}{D_h}) \tag{5.14}$$

where

$$Re = \frac{\rho v D_h}{\mu} \tag{5.15}$$

and

$$Pr = \frac{C_p \mu}{k} \tag{5.16}$$

Where ρ is the density of the water, μ is the dynamic viscosity of the water, k is the thermal conductivity, C_p is the specific heat capacity of water and v is velocity of water. D_h is the hydraulic diameter, expressed in terms of cross sectional area and wetted perimeter.

Once the temperature profile across the membrane has been calculated the corresponding pressure profile can be determined using the Antoine equation, as shown in equation 5.2. When the temperature and pressure profiles across the membrane are known, the mass flux of distillate can be calculated. The molar flux through the membrane can be described by Knudsen diffusion, Poiseuille flow and air trapped in the pores of the membrane. The total flux through the membrane is expressed as:

$$\begin{aligned} N_{membrane} &= \frac{1}{RT_{ave,membrane}} \left(\frac{1}{D_{kn}} + \frac{1}{D_{st}} \right)^{-1} \frac{\Delta P_{membrane}}{\delta_{membrane}} \\ &= H_{membrane} \Delta P_{membrane} \end{aligned} \tag{5.17}$$

$T_{ave,membrane}$ is the average temperature between both sides of the membrane, $\Delta P_{membrane}$ is the vapour pressure difference between both sides of the membrane. D_{kn} is the coefficient of Knudsen diffusion, expressed as [21]:

$$D_{kn} = \frac{2\phi r_p}{3\tau} \left(\frac{8RT_{ave,membrane}}{\pi M} \right)^{\frac{1}{2}} \tag{5.18}$$

D_{st} is the diffusion coefficient of the stagnant air in the pores, expressed as:

$$D_{st} = \frac{D\phi P}{\tau P_{ln}} \tag{5.19}$$

The molar flux of the vapour through the air-gap can be expressed as:

$$N_{airgap} = \frac{D}{RT_{ave,airgap}} \frac{P}{P_{ln}} \frac{\Delta P_{airgap}}{\delta_{airgap}}$$
$$= H_{airgap} \Delta P_{airgap} \tag{5.20}$$

Therefore the total molar flux of the vapour through both the membrane and the air-gap can be given as:

$$N_{membrane+airgap} = \left(\frac{1}{H_{membrane}} + \frac{1}{H_{airgap}} \right)^{-1} \Delta P_{total} \tag{5.21}$$

The vapour flux, N_{total}, is given by the molecular weight of water multiplied by the molar flux across the membrane and air gap.

5.3.2 Numerical model validation

In the follow section the mathematical model detailed perviously was used to validate the experimental results from the system. Values of cold feed inlet temperature, hot feed inlet temperature and feed flow rate where input into the model. A consistent cold feed inlet temperature of 17.5°C was used throughout the analysis, while the hot feed inlet temperature was varied from 30 - 80°C and feed flow rate range of 0.4 - 1 l/min was used.

Figure 5.12 shows a comparison between results from the model and experimental data for distillate flux versus hot inlet temperature for the range of feed flow rates. The figure shows a good correlation between the experimental data and the model, particularly for the mid-range flow rates.

However for higher flow rates the experimental distillate output was higher than predicted and for lower flow rates the distillate output is lower than predicted, this suggests that there is a systematic error relating to flow rate. Figure 5.6 indicates that feed flow rate has a significant, and perhaps more complex influence on the distillate flux than the model describe. As higher flow rates lead to greater mixing in the channels

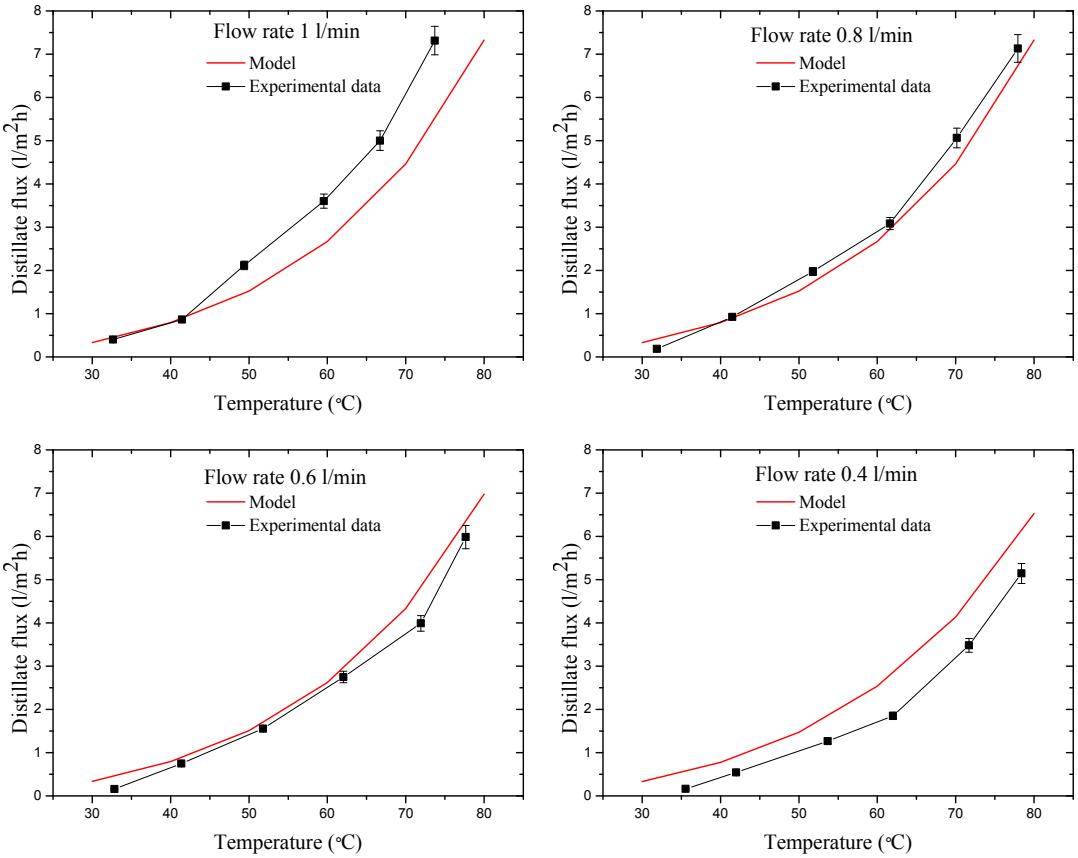

Figure 5.12: Validation of experimental data with mathematical model predictions. Distillate flux versus hot inlet feed temperature for different feed flow rates.

and a reduction of the temperature polarisation layer, leading to an improved distillate output. When calculating the Reynolds and Prandtl the model uses a correlation taken from literature, however further work is required to establish a correlation that is specifically developed for channels containing Tenax spacers used in this module. Several MD specific CFD models have been developed to address this problem [80, 81, 82], however they have not been experimentally validated. Pito el al [83] and Tamburini et al [84] suggested combining the use of Thermochromic Liquid Crystals (TLCs) and digital Image Analysis to determine the local distribution of convective heat transfer coefficients within the channels. It is suggested that to develop the mathematical model further it should incorporate findings from the studies listed above.

It was suggested by Cipollina et al [22], that higher feed flow rates exert a greater

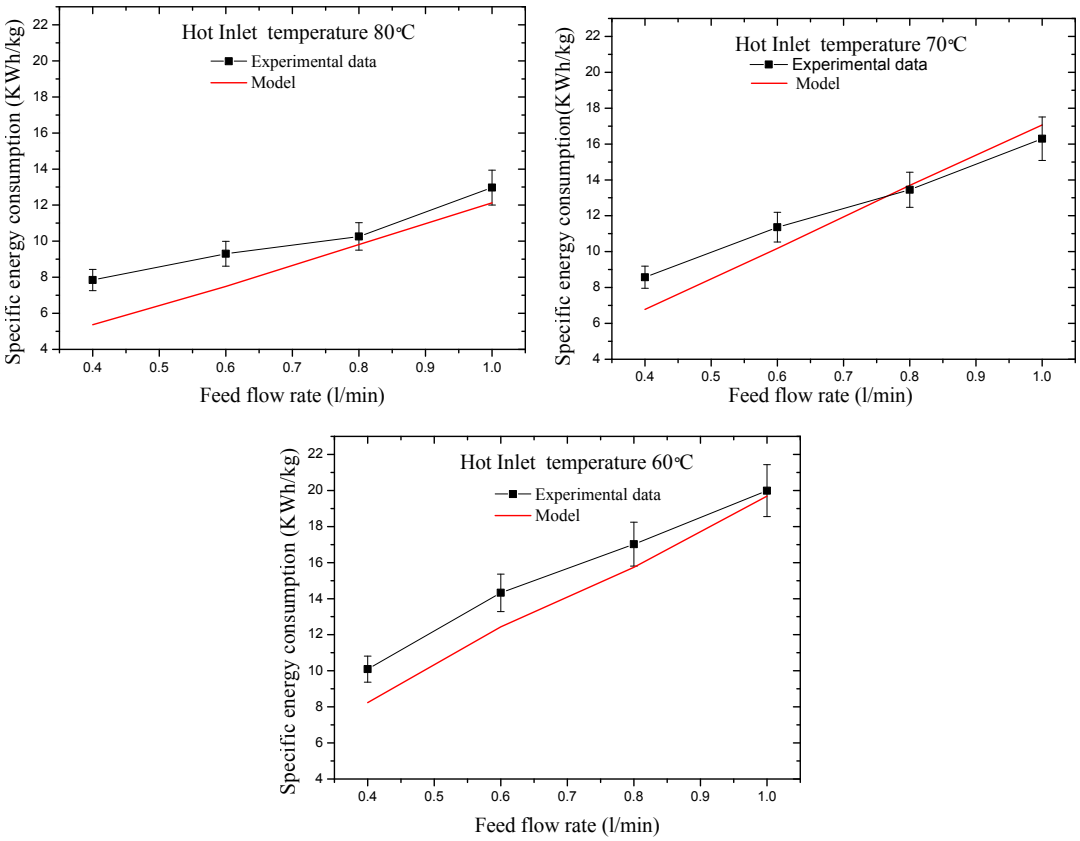

Figure 5.13: Specific energy consumption versus feed flow rates for different hot inlet feed temperature.

hydraulic pressure on the membrane and cooling sheet that separate the channels, causing the width of the air-gap to shrink. A smaller air-gap would result in an increase in distillate flux. This could account for the greater distillate flux seen at high feed flow rates.

The distillate output is below predictions for low flow rates. The disparity between predicted trends and experimental data is larger at higher inlet feed temperatures. However the percentage mismatch is proportional to the total distillate output, when compared across the temperature range.

Figure 5.13 shows a comparison between the experimental data and the model output for Specific Energy Consumption, SEC, over a range of feed flow rates from 0.4 - 1 l/min. SEC, is the thermal energy used to produce a kilogram of distillate, as shown

in equation 5.3. The experimental data is in agreement with the model predictions, particularly for higher flow rates. Although in most cases the system performed less efficiently than expected.

5.4 Conclusions

In this chapter the steady-state performance of the MD system was characterised over the entire feed temperature operating range, from 30 - 80°C, and within the feed flow rate range of 0.2 - 1.0 l/min. In order to establish steady-state conditions the input parameters were set and the system was operated until the output from the module was stable.

An exponential relationship between feed temperature and distillate flux was observed when the feed flow rate was kept constant while the feed inlet temperature was varied. For a constant inlet feed temperature while the feed flow rate was increased, a linear trend was revealed; as feed flow increased so did the distillate output. The distillate flux ranged from 2.2 - 8.5 l/m^{2}h, with the highest value corresponding to the feed temperature of 80 °C and a flow rate of 1.0 l/min. From this we can conclude that inlet feed temperature is a more significant parameter in terms of the distillate yield and should therefore be a priority when designing a system.

The driving force in MD is the vapour pressure difference across the membrane, which is a function of the temperature difference across the membrane. Both of these parameters were explored as a function of feed temperature and flow rate, and it was found that an increase in the feed flow rate yielded only a very slight rise in the driving force across the membrane. This suggests that the influence of feed flow rate on the distillate output is largely the effect it has on mixing and hydrodynamics of the channels, and the subsequent reduction in the temperature and concentration polarisation effects.

A comparison was also made between two PTFE membranes manufactured by Gore^{TM}, G02 and G04, having average pore size of 0.2 and 0.45 μm respectively. It was found that the G04 membranes produced a higher distillate flux than G02 under the

same operating conditions. This was attributed to improved mass transfer through the larger pores. However the G04 membrane produced distillate with a higher conductivity and therefore a worse quality yield. This is expected as the larger pores have a lower LEP, and therefore membrane wetting is more likely to occur. The influence of pore size on the LEP of the membrane and its subsequent effect of the quality of distillate produced are further in the following chapters.

A description of a mathematical model for predicting distillate output was given and then used to draw comparison with experimental data. Results show that the experimental data has a strong correlation with predictions from the model. However the system consistently under-performed at low feed flow rates and over-performed at high feed flow rates. This suggests that the theory used in the model underestimates the significance of feed flow. It is proposed that the model does not take into account mixing in the channel.

It was necessary to establish the performance of the system whilst operating in a stable manner, before it could be characterised under fluctuating conditions. Hence, this chapter outlined the distillate output from the system, in terms of conductivity and flux, under steady-state conditions. However what is yet to be established is how the system performs when the operating with input parameters that are intermittent. To understand the influence of intermittent use, the effects of heating and cooling the module must be investigated. To do so, the microstructure of the membrane was analysed with the use of a scanning electron microscope at various temperatures; the results of which are detailed in the next chapter.

Chapter 6

Temperature effects on membrane microstructure

In this chapter an investigation was undertaken to determine the effects of temperature on the microstructure of the membrane. By characterising changes in the membrane at various temperatures, we can examine the effect of the intermittent use of the membrane module.

The microstructure of G02 Gore^{TM} PTFE membranes is examined at a constant temperature of 17°C with the use of a Scanning Electron Microscope (SEM). The porosity and average pore size of the membrane is determined via image analysis with ImageJ software [85]. The manufacturer's stated values, which are obtained through

the use of capillary flow porometry, are compared against the values found by image analysis techniques.

Heat was applied to the sample with the use of a Deben Peltier stage placed inside the SEM chamber. The temperature of the sample was increased and its structure was observed over a period of 80 minutes. The microstructure of the membrane was examined at temperatures up to 80°C, the maximum operating temperature of the membrane distillation process.

The changes in microstructure of the membrane as a result of the temperature increase will effect the operating performance of the membrane module. The size and structure of the pores determine the mechanism of vapour diffusion across the membrane, and therefore the volume of distillate produced during operation. The pore geometry also influences the Liquid Entry Pressure (LEP) of the membrane and therefore any changes would effect the hydrophobic properties. The influence of change in microstructure of the membrane with temperature on module performance is discussed in this chapter, as are the implications for their intermittent use in a membrane distillation system.

6.1 Membrane microstructure at room temperature (17°C)

An SEM was used to image membrane material manufactured by Gore^{TM}. An FEI Quanta SEM with a field emission source was used to obtain an image of the membrane surface, a schematic diagram of the SEM experimental set up is shown in figure 6.1.

The G02 membrane has an average pore diameter of 0.2μm. Other properties of this membrane can be found in table 3.1. The active layer of the membrane, made from expanded polytetrafluroethylene ($PTFE$), can be seen in figure 6.2(a). Underneath the PTFE is an unwoven polypropylene support layer, shown in figure 6.2(b).

6.1.1 Membrane porosity

The porosity of the membrane, ϕ is defined as [86]:

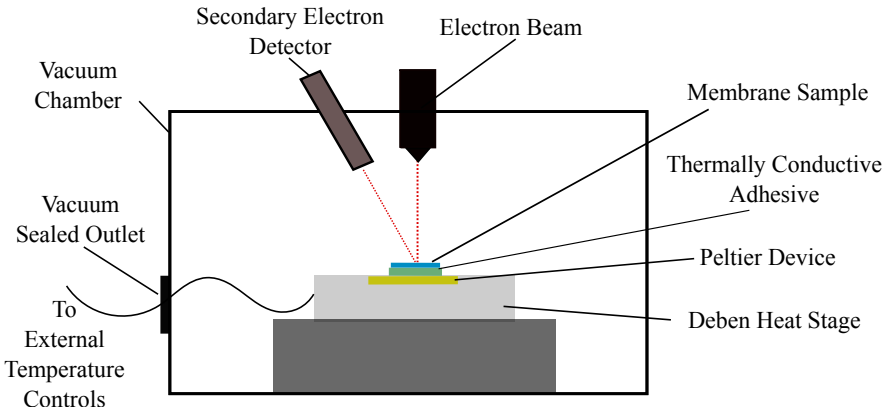

Figure 6.1: Schematic diagram of the experimental setup inside the SEM chamber

$$\phi = 1 - \frac{A_p}{A_m} \ , \tag{6.1}$$

where A_p is the area of the pores and A_t is the total membrane surface area.

The manufacturer, Gore^{TM}, state that the G02 membrane has an active surface with pore diameter of 0.2 μm. The pore size was determined through the use of capillary flow porometry, where a fully wetted sample of the membrane is put in a sealed chamber. Compressed gas flows into the chamber and the pressure gradually increases, until all of the liquid is forced out of the membrane pores. The pressure and flow rates are recorded and used to calculate the pore size. These calculations assume that all pores are circular in cross section and uniform along their length. However as can be seen from 6.2(a), the membrane material is a complex web of interconnecting nodes and fibres, that display little uniformity.

The use of SEM imaging as an alternative method of determining the membrane characteristics was investigated in this research. Values of pore size and porosity were obtained directly from an SEM image. In order to image the membrane with an SEM it is necessary to coat it in a thin layer of gold, so that the material will conduct. A sputter coater was used to add a 5 μm thick coating of gold to the surface of the membrane.

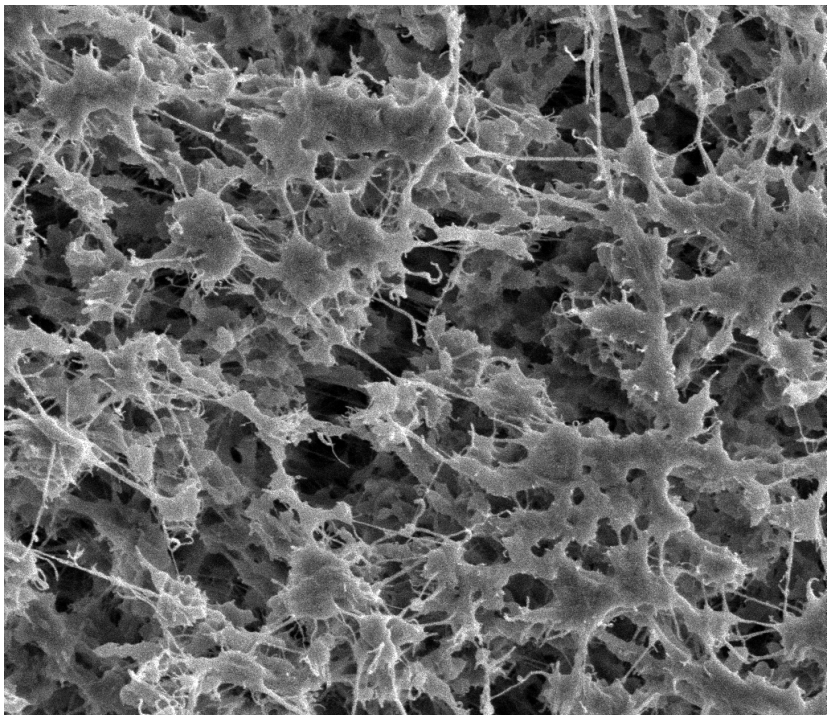

(a)

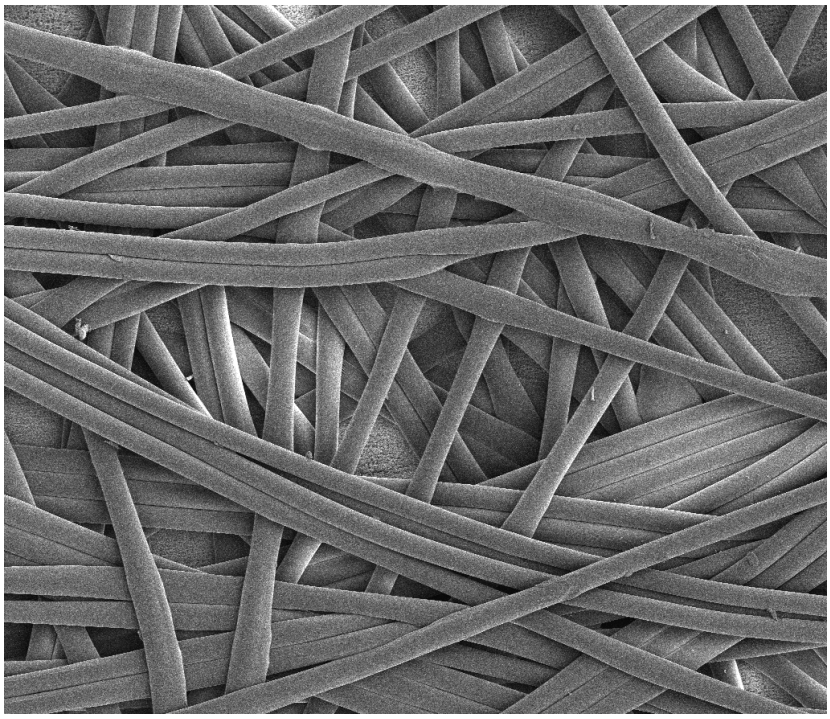

(b)

Figure 6.2: SEM image of a) the active expanded PTFE membrane side and b) polypropylene support layer

The image obtained from the SEM was digitised using ImageJ software and each pixel given a value on a greyscale between 0 - 255; the darkest pixels have a 0 value and the lightest have a value of 255. A threshold of 60 was chosen and the software was used to select pixels with a value above the threshold, selecting the lighter regions in the image. The choice of threshold was done visually, as this value best selected all of the area that appeared to be membrane material. The pixels identified as membrane material were then counted to determine the porosity. Figure 6.3 shows the membrane material after the threshold was set, the lighter pixels are coloured red. A transparency setting of 50% was applied to the red threshold setting, therefore the membrane material is visible behind the highlighted region. The porosity was found to be 84%.

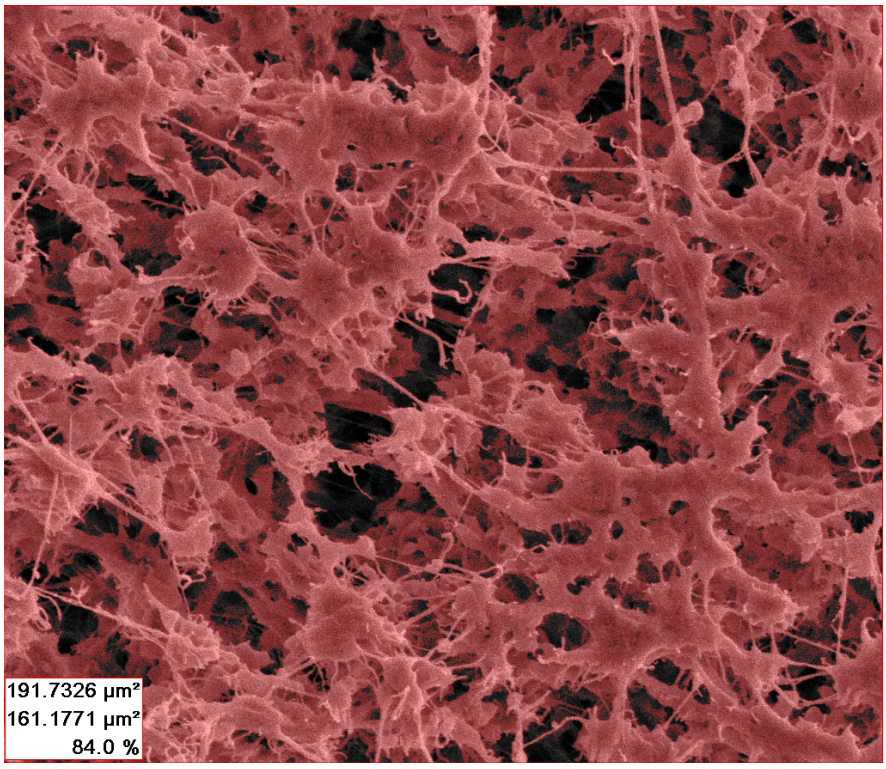

Figure 6.3: PTFE membrane with light membrane areas highlighted in red. Total surface area, total area of the membrane material and porosity are given in the bottom left, respectively

The error in the porosity measurement was established by altering the threshold set on the grey scale by ± 5 of original greyscale threshold value selected. This was

done to ascertain the significance of the judgement made when selecting the threshold by eye. When the threshold was +5 of the original value, at 65, the porosity was 88%. At -5 of the selected value, at 55, the porosity was 79%. This demonstrated that the measurement is subject to human error and highlights the importance of setting the threshold accurately. When considering the margin for error, the value of porosity determine via image analysis is similar to 80% stated in the manufacturers specifications.

In figure 6.4 the membrane image is shown with three different thresholds that were used to establish the error. Figure 6.4(b) shows the threshold at 60, this was the threshold selection that was deemed to be most accurate as the membrane material is highlighted in white, while the porous areas remain black.

Figure 6.4(a) shows the image when the threshold was set at 65; in this instance some of the membrane material has not been selected. Figure 6.4(c) shows the threshold when set at 55; this value was considered too low as some of the dark porous regions have also been selected along with the membrane material.

6.1.2 Average pore size

The software was used to measure the perimeter and the area of each pore within the sample. Although the pores are not circular a value of pore diameter can be found using an equation for the equivalent pore diameter, d_p, which is defined as [87]:

$$d_p = 2\sqrt{\frac{A_p}{\pi}}\ , \tag{6.2}$$

where A_p is the area of the pore.

The software was used to select and measure 145 features in the image, identified as pores. These pores are highlighted in figure 6.5.

There is a large variation in the area and equivalent diameters of the pores in the sample, ranging from 0.12-1.88 μm. The frequency distribution of pore diameters within the sample is shown in figure 6.6. The most frequently occurring pore diameter

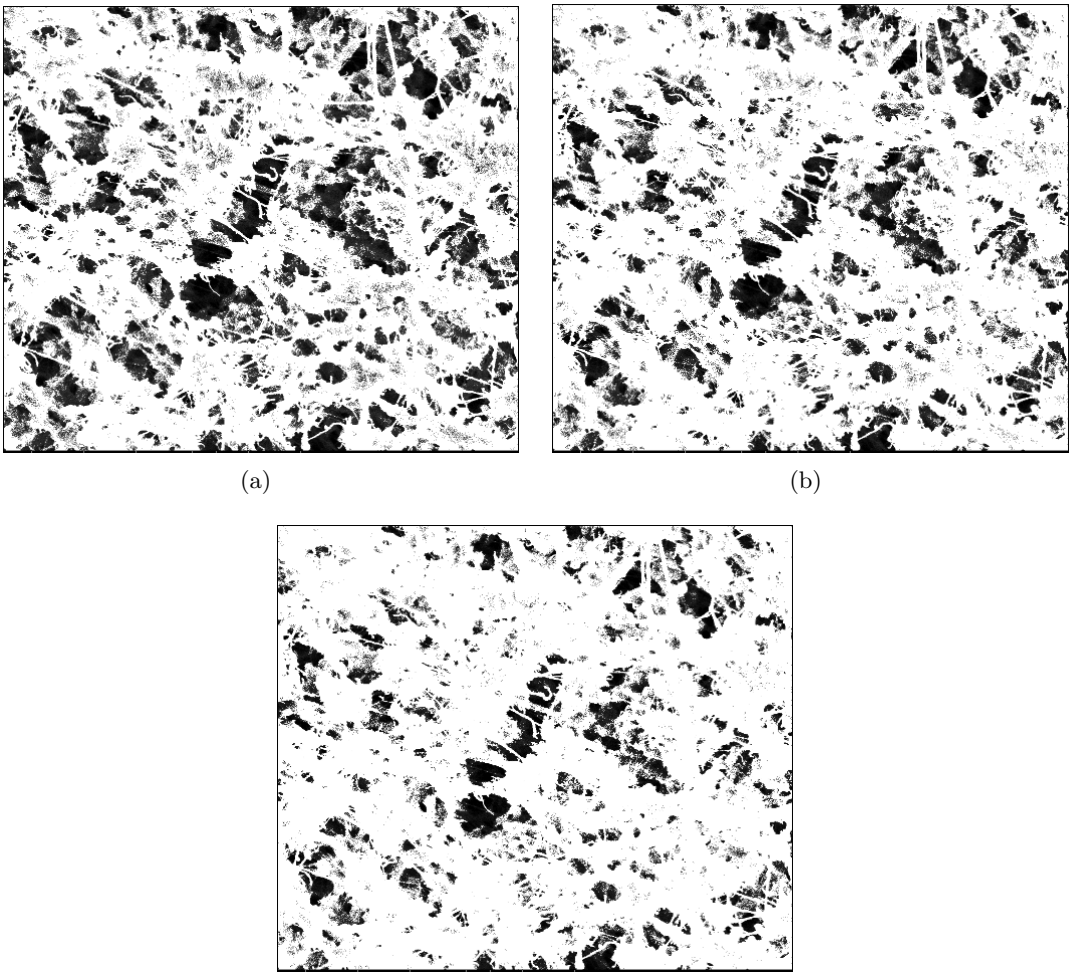

(a) (b)

(c)

Figure 6.4: Images of the membrane with various threshold setting. a) threshold set at 65, b) threshold set at 60, c) threshold set at 55.

within the sample is 0.3 μm. This value is higher than the 0.2 μm average pore size stated by the manufacturer.

Both the values for porosity and pore diameter determined through image analysis are slightly larger than the manufactures specifications. This could be due, in part, to the uneven distribution of pores across the surface of the membrane, as the SEM image in figure 6.7 shows. The image used in the analysis of porosity and pore size, is a magnification of the region in the bottom left of figure 6.7, (indicated as A); this region is particularly porous. Another issue may be that the SEM image gives 2-

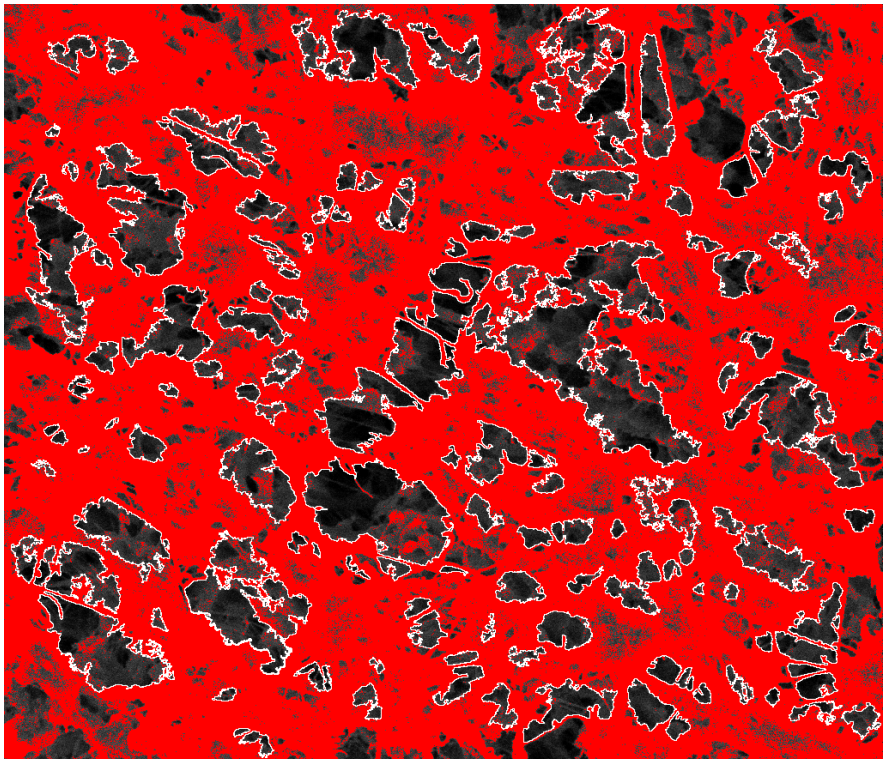

Figure 6.5: PTFE membrane with selected pores perimeter highlighted in white

dimensional projection of the pores, therefore the porosity is based on the top surface of the membrane.

6.2 Membrane microstructure evolution as a function of temperature

The membranes used in these experiments have a complex structure; the pores are formed by interconnecting fibrous strands of PTFE material. The pore size distribution of PTFE membranes are usually assumed to be constant over the typical operating range of the MD process, from 30 - 80°C. However PTFE is a thermoplastic, known to expand when heated. Therefore as the membrane is heated the fibrous strands will expand in all directions and the pore size will change. Pore size influences the performance of the membrane, as it effects factors such as LEP and the likelihood of

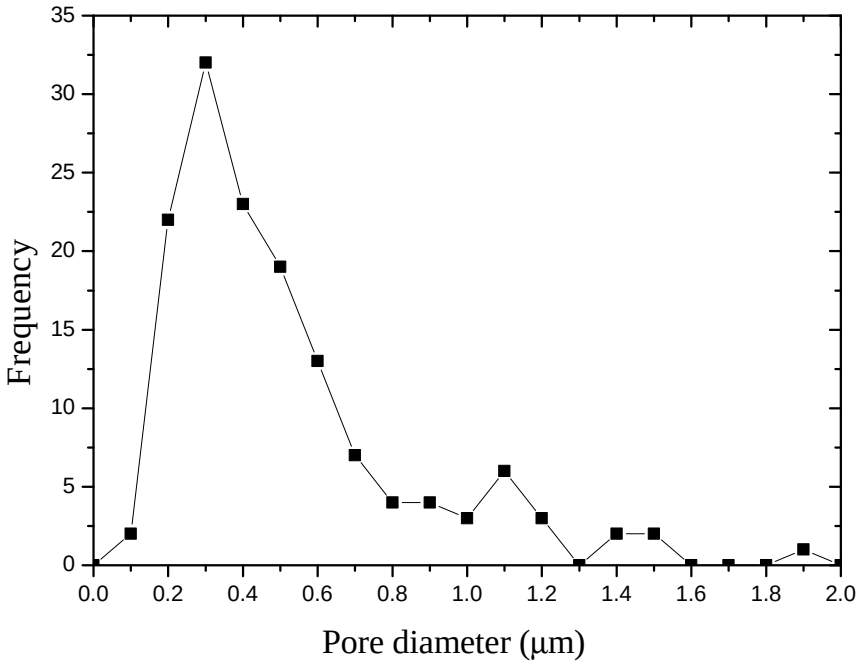

Figure 6.6: Equivalent pore size frequency distribution of the sample

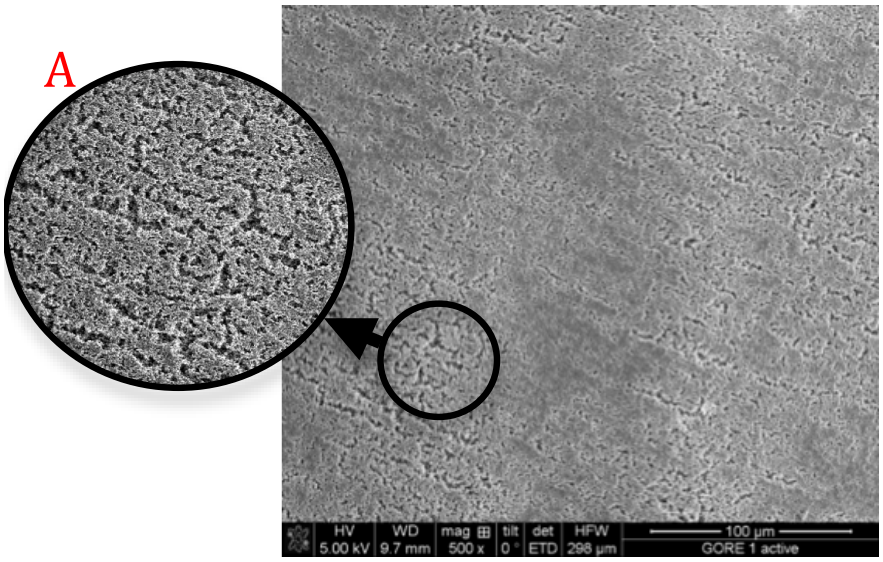

Figure 6.7: PTFE membrane surface at 500x magnification, highly porous region used in the analysis is enlarged and indicated as A.

membrane wetting. It also determines the mechanism of diffusion of vapour across the membrane and hence the volume of distillate produced. This section investigates the thermal expansion of PTFE and its influence on membrane pore size. Furthermore the implications of PTFE expansion on performance of the MD process are discussed.

6.2.1 Thermal expansion of the PTFE membrane material

Polytetrafluoroethylene ($PTFE$) is a synthetic semicrystalline fluoropolymer commonly known as Teflon. The PTFE molecule is highly stable, it has high heat resistance, chemical resistance and it is electrically insulating. Its crystalline melting point is 327°C [88].

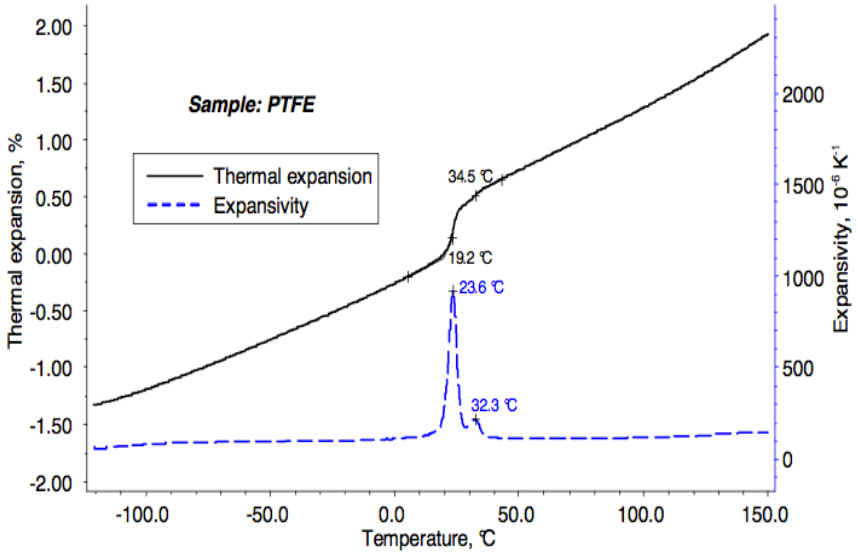

Figure 6.8: Thermal expansion and expansivity of PTFE material

PTFE goes through a crystal-crystal transition at 19.2°C and 34.5°C, when the average distance between molecules in polymer chain increases [89]. This results in a rapid expansion of the material. Blumm et al [90] measured the linear thermal expansion and expansivity of PTFE, shown in figure 6.8 [90]. The linear thermal expansion coefficient is defined by Kirby et al [91] as:

$$\alpha = \frac{1}{L_0}\frac{\delta L}{\delta T} \ , \tag{6.3}$$

where L_0 is the original length of the sample, δL is the increase in length for an increase of δT in temperature. It is seen in figure 6.8 that the thermal expansion coefficient is highly temperature dependant between 20°C and 40°C, peaks are seen at 19.2°C and 34.5°C which correspond to the solid state transitions seen at these temperatures. In these temperature ranges a rapid expansion in the material is seen.

It is important to note that the thermal expansion of PTFE with the operating range of MD is reversible when the material is cooled. The structural change in PTFE that occurs during the crystal-crystal transitions at 19.2°C and 34.5°C is reversible [91]. Therefore as operation of the membrane module begins the material will expand. When the module cools, during an overnight shut down for example, the material will contract again and the process will repeat the next time the module is operated.

A series of experiments were carried out to understand the influence of temperature on the expansion of PTFE material and the size of the pores. A Deben Peltier heating stage was placed inside an SEM chamber and the sample was put directly on the stage. The chamber, Peltier stage and sample all had an initial temperature of 17°C. The temperature of the stage was then set using external controls, the stage reached its set temperature in under 20 seconds. However it is expected that the PTFE sample would take much longer to heat, as it is a less thermally conductive material. The sample was imaged every 10 minutes to determine the expansion of the material and the length of time for it to reach the temperature of the stage. It was assumed that when the material stopped expanding the sample had reached the same temperature as the stage.

In figure 6.9, a fibrous strand of PTFE within the membrane sample was selected and imaged over time time as the sample was heated to 70°C. Figure 6.9(a) shows the sample at its initial temperature of 17°C. The Peltier stage on which the sample was resting was then set to 70°C and reached that temperature in under 20 seconds. An image was taken at ten minute intervals thereafter and the node shows an increase in

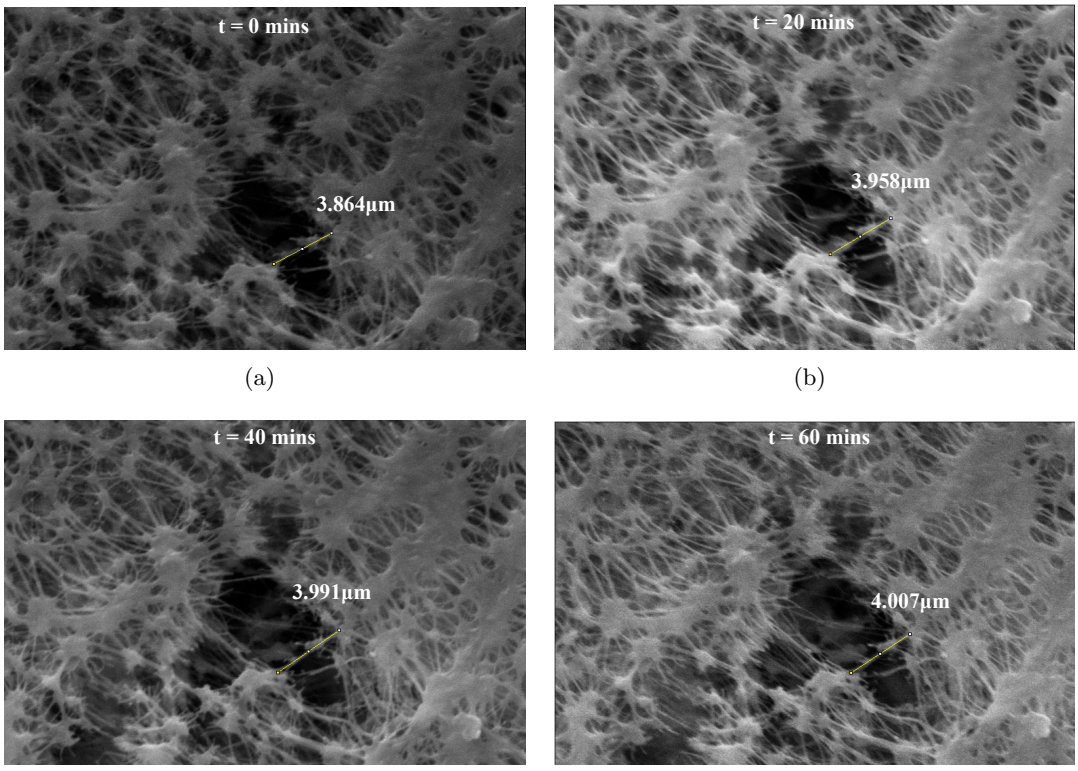

Figure 6.9: SEM images of a PTFE membrane when placed on a heating stages set at 70°C. The images show measurements of a node at time 0, then after 20, 40 and 60 minutes

length over time.

Figure 6.10 shows the length of the node measured on the image at 10 minute intervals, as it was heated. The length of the node increased over time. It is also important to note the presence of an initial rapid expansion in the nodes length, which corresponds to the solid state transition that takes place at 19.2°C. The gradient of the trend decreases between 10 and 20 minutes. It then increases again after 20 minutes, indicating the event of the second solid state transition at 34.5°C. After these transitions the rate of thermal expansion is linear. The specific length expansion of the node has a similar trend to the thermal expansion shown in figure 6.8, with two periods of accelerated expansion, the first being greater than the second.

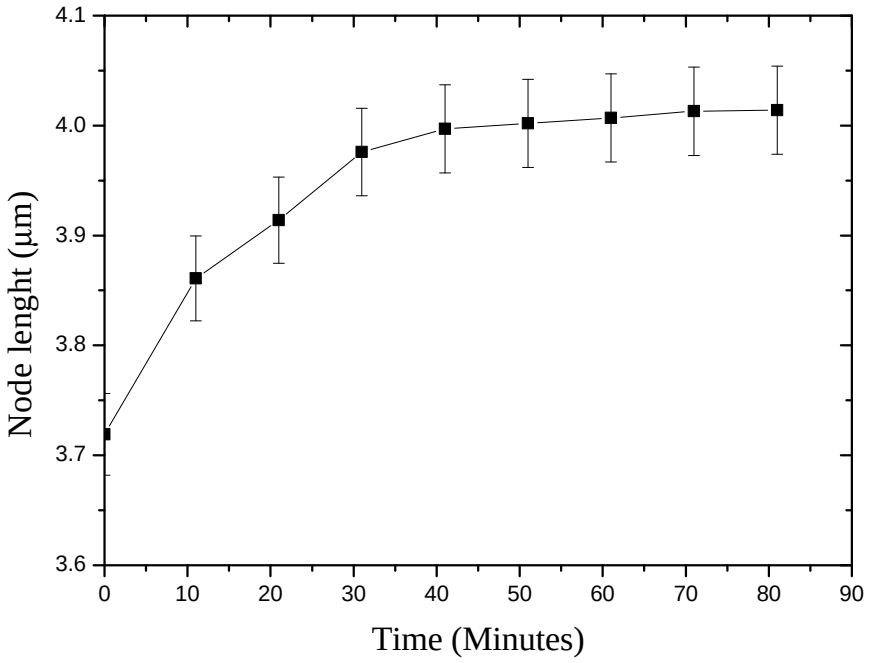

Figure 6.10: Node length over time for 70°C

6.2.2 Temperature effects on pore length

In this section the effects of thermal expansion of the material on pore size was investigated. An image was taken at the ambient temperature, 17°C. This image is represented as t=0 minutes 6.11(a). External controls were used to set the temperature of the stage to 60°C. The temperature of the stage regulates to within ± 0.2°C of the set temperature. The sample was left on the stage for 80 minutes and images were recorded every 10 minutes. These images can be seen in figure 6.11.

The figure shows the same pore at t=20 minutes 6.11(b), t=40 minutes 6.11(c), and t=60 minutes 6.11(d). The pore is not circular, therefore selecting the same diameter in each image is challenging. To overcome this, two distinct features on the pores perimeter in figure 6.11(a) were selected and a line segment was drawn between them. The same features could then be easily identified and selected in the subsequent images,

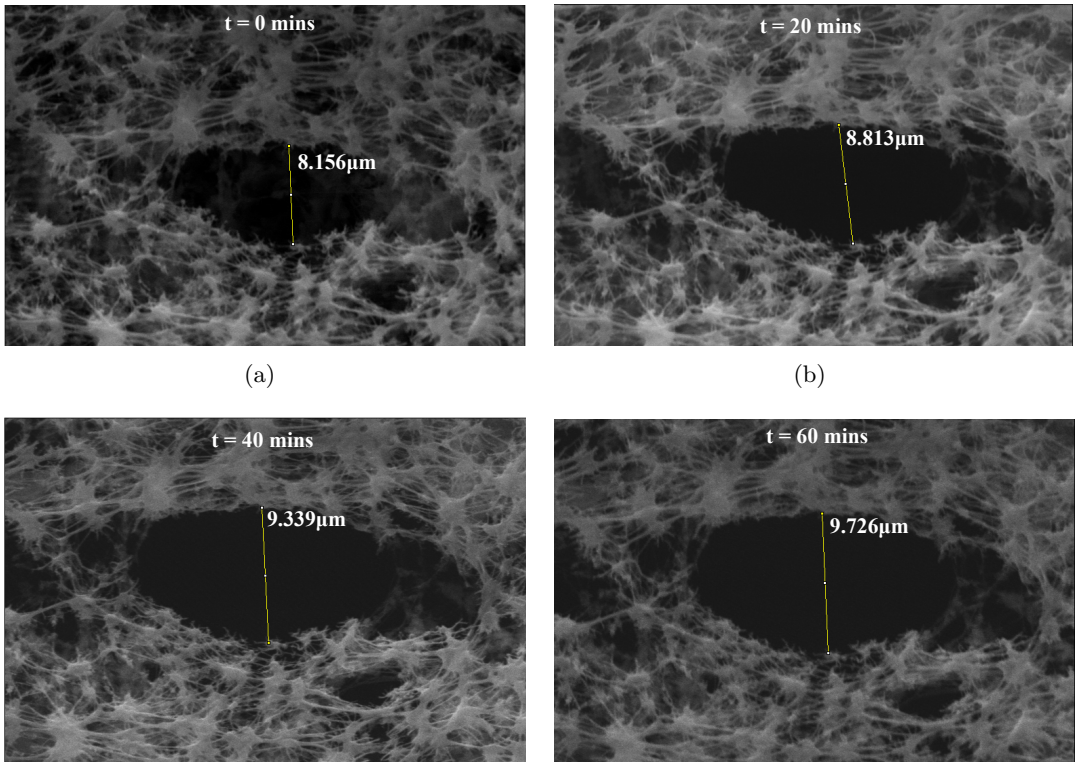

Figure 6.11: SEM images of a membrane on a heating stages set at 60°C. The images show the pore at time 0, then after 20, 40 and 60 minutes

ensuring the same feature was measured throughout the analysis. In each subfigure the feature of the pore has been measured and is shown. The pore length increases in each image. At t=0 and ambient temperature the diameter of the pore was 8.156 μm. After 60 minutes the pore length had increased to 9.726 μm. This is due to thermal expansion of the PTFE membrane material.

The rate of increase in the pore diameter is shown in figure 6.12. Initially, the rate of increase is rapid, it begins to slow after 50 minutes however it did not reach a steady state over the 80 minute duration. This indicated that the sample had not reached 60°C in this time.

The pore expansion trend shown in the figure bears the same distinctive features as the trend for thermal expansion of PTFE, shown in figure 6.8. There is an initial rapid expansion, corresponding to the transition phase at 19.2°C. After 10 minutes expansion

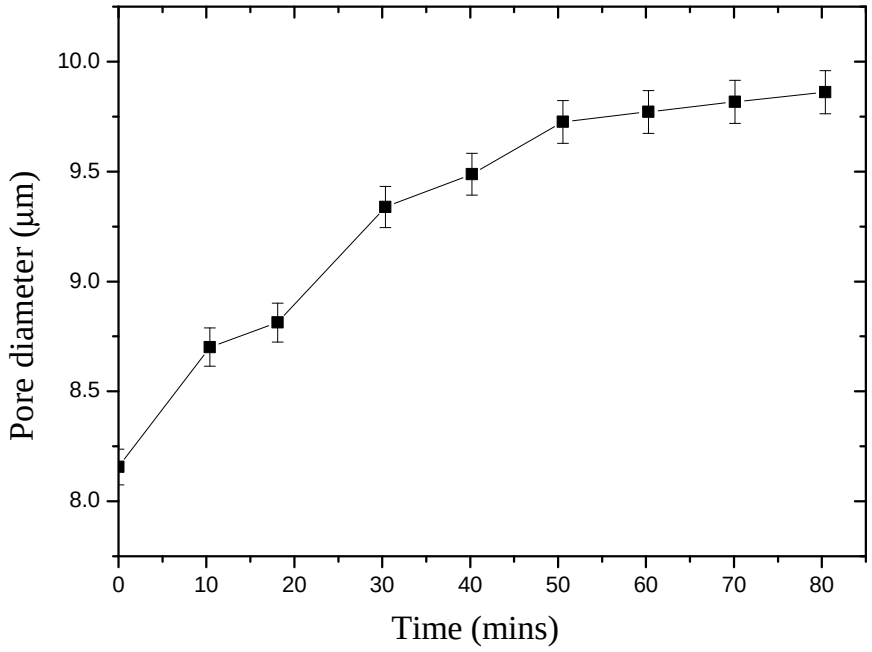

Figure 6.12: Diameter of the pore over time at 60°C

of the pore slows, which is then followed by a second rapid expansion, corresponding to the second crystal- crystal transition at 34.5°C. After the second transition, the rate of expansion in pore diameter slows down, and remains linear for a further 20 minutes. In the final 30 minutes of the experiment the rate of expansion decreases gradually. This suggests that the temperature of the PTFE was near to the temperature of the Peltier stage, set at 60°C, but had not reached it.

Figure 6.13 shows images of a sample that was placed on the heating stage when it was set to 70 °C. It was not possible to use the same membrane sample more than once during these experiments. As in order to image the membrane with an SEM it is necessary to coat the sample with a thin layer of electrically conductive material, in this instance gold was used. When heated this gold layer is annealed and therefore the material will not return to its original dimensions after cooling.

However a gold coating is not present on the membrane when used inside a

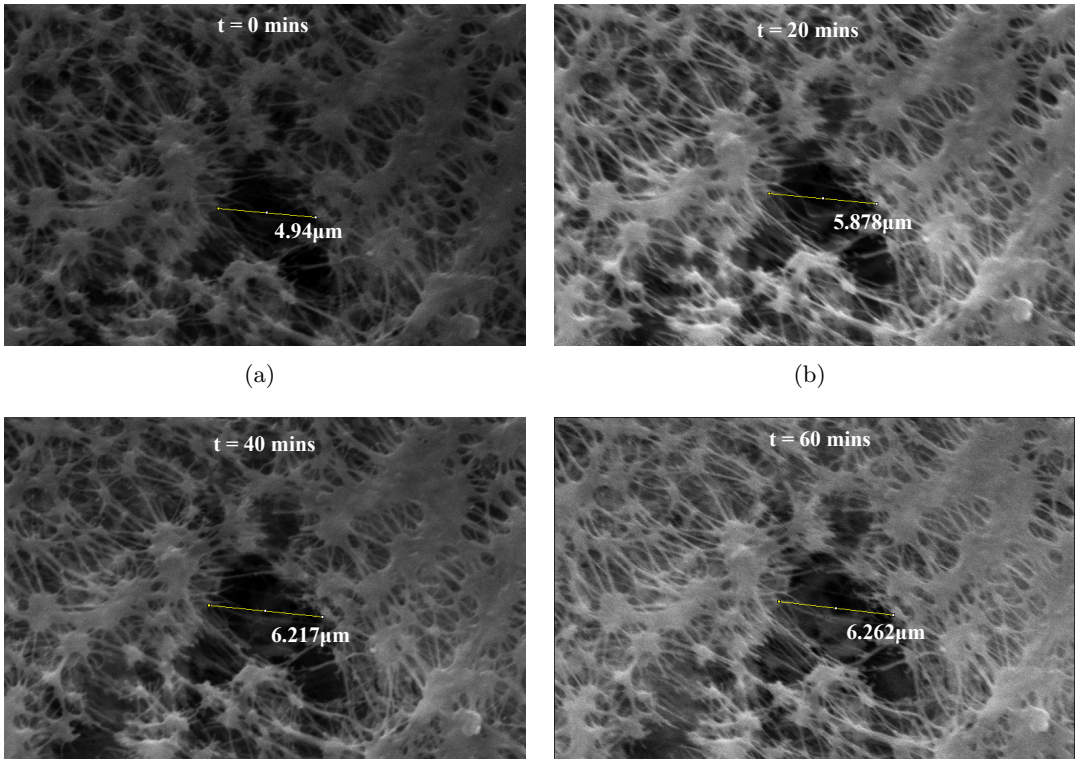

Figure 6.13: SEM images of a PTFE membrane when placed on a heating stages set at 70°C. The images show the pore at time 0, then after 20, 40 and 60 minutes

Membrane Distillation (MD) module. The membrane itself is made of PTFE, which is a thermoplastic material that will not be annealed within the operating temperature range of Membrane Distillation (MD) . Therefore it is important to note that this process of thermal expansion is reversible for the MD process and the membrane inside of module will return to its original dimensions when cooled. However for the purpose of this series of experiments in was necessary to use a new sample each time and therefore a new feature was identified in figure 6.13.

Figure 6.13(a) shows the sample when the chamber and heating stage were at an ambient temperature of 17°C. The heating stage was set to 70°C and figures 6.13(b)-6.13(d) show the membrane at 20 minute intervals thereafter. Again, the length of the pore increased throughout the duration of the experiment. At t=0, when the temperature was an ambient 17°C , the pore length was 4.940 μm. After resting on

the stage set to 70°C for 60 minutes, the length had increased to 6.262 μm.

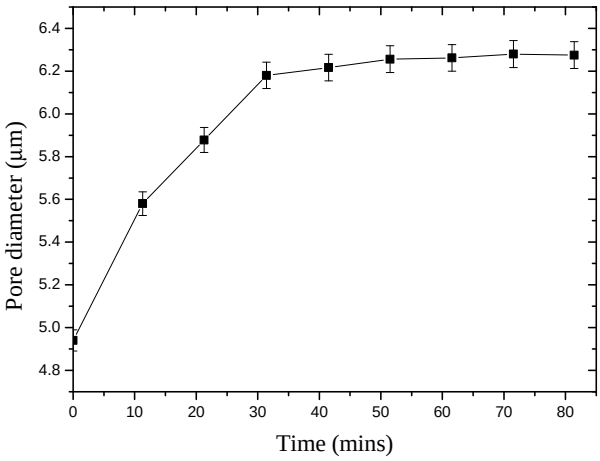

Figure 6.14: Diameter of the pore over time at 70°C

The measured length of the pore at each 10 minute interval is shown in figure 6.14. The rate of increase in the length of the pore was greater in the first 30 minutes of the experiment. After 40 minutes the length of the feature remained relatively constant, increasing by only 1% in the final 40 minutes. From this we can assume that the sample reached a temperature approaching 70°C after 40 minutes of reaching on the stage.

Figure 6.15 shows SEM images of a membrane sample when the heating stage was set to 80°C. Figure 6.15(a) shows the sample when the chamber and heating stage were at 17°C. The heating stage was set to 80°C and the figures 6.15(b) - 6.15(d) show the membrane at 20 minute intervals after. At t=0 and ambient temperature of 17°C, the pore length was 3.729 μm. After resting on the stage set to 80°C for 60 minutes, the length had increased to 5.367 μm.

The rate of increase in the pore diameter is shown in figure 6.16. The pore diameter increases rapidly at first. However the pore size becomes stable after 40 minutes, increasing by only 2% in the final 40 minutes. Again, the trend shows two distinct periods of rapid expansion corresponding to the solid to solid transition stages at 19.2°C and 34.5°C.

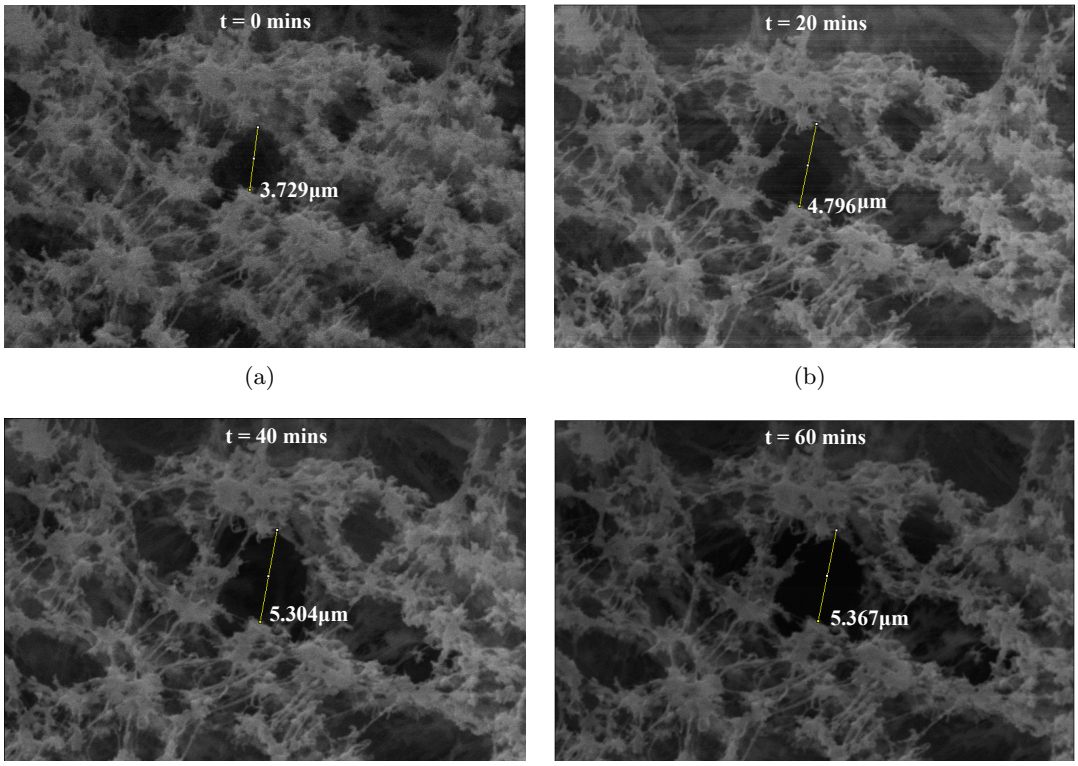

Figure 6.15: SEM images of a PTFE membrane when placed on a heating stages set at 80°C. The images show the pore at time 0, then after 20, 40 and 60 minutes.

To give an understanding of the pore's expansion in 2-dimensions, the area of the pore was measured when the sample was placed on the heating stage set to 80°C. This analysis was carried out using the same set of SEM images used to investigate the increase in pore diameter, shown in figure 6.15. The wand tracing function in ImageJ software was used to select the perimeter of the pore, as this was deemed to be more accurate than tracing the pore by hand. The SEM images are shown in figure 6.17; the pore perimeter has been highlighted and a measurement for pore area is included on each image. Figure 6.17(a) shows the area of the pore at room temperature was 14.167 μm^2. After 60 minutes the pores are area had increased to 20.907 μm^2, seen in figure 6.17(d); this is an increase of 32%.

Using equation 6.2 it is possible to calculate a value of the equivalent pore diameter from the area measured in the previous figure. This trend is shown in figure 6.18, the

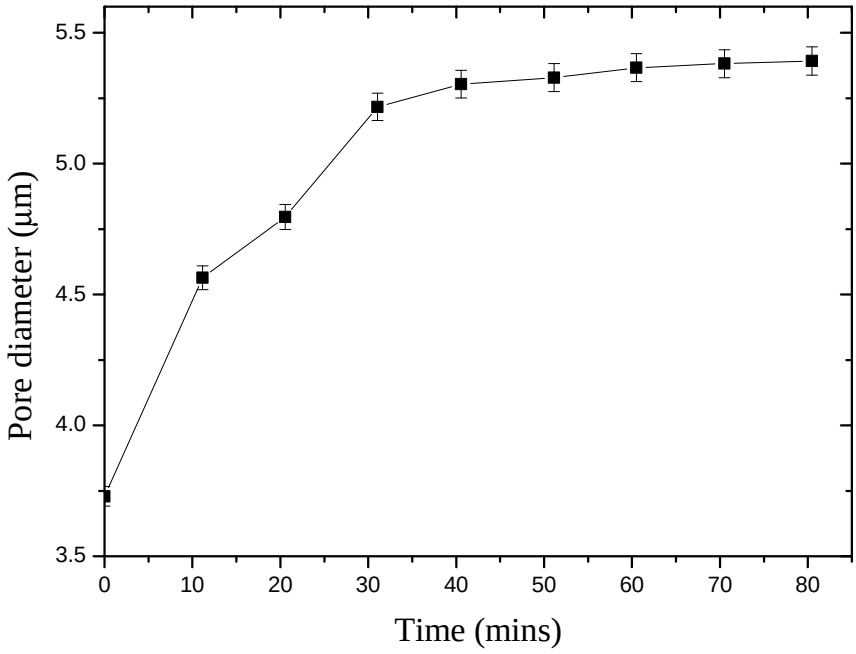

Figure 6.16: Diameter of the pore over time at 80°C

measured pore diameter from figure 6.15 is also shown for comparison. The overall expansion in equivalent pore diameter is slightly smaller than the measure diameter, however it does show a very similar trend to the measured diameter. There was an initial rapid increase in equivalent pore diameter within the first 10 minutes of the experiment, followed by a decreased rate of expansion for the next 30 minutes. The equivalent pore diameter became reasonably stable after 40 minutes, increasing by only 0.4% in the final 40 minutes of the experiment.

Given the similarities in the two trends it is reasonable to assume that the pores expansion is uniform in 2 dimensions. Therefore we can infer that the method used in this section to measure pore length between two distinct features gives a fair representation of the changes in pore diameter.

Further analysis of the increase in pore area was difficult from the remaining sets of SEM images. The feature seen in figure 6.11 and figure 6.13, when the sample was

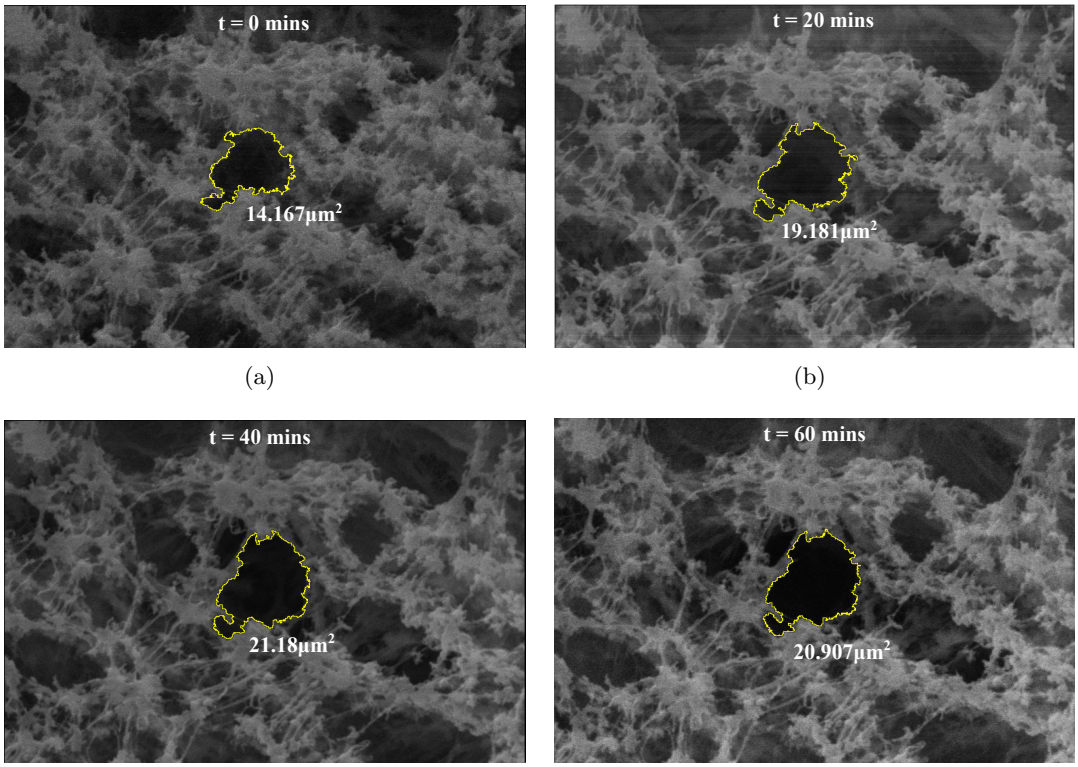

Figure 6.17: SEM images of a PTFE membrane when placed on a heating stages set at 80°C. The images show the pore at time 0, then after 20, 40 and 60 minutes. The pore perimeter is highlighted in each image

heated to 60 and 70°C, have a complicated shape with several thin strands of PTFE material stretching across the pore, and protruding from its perimeter. Therefore it was not possible to accurately select the perimeter of the pore throughout the series of images, and hence a meaningful analysis of the pore's area could not be conducted.

A comparison of the rates of increase in length over time for 60, 70 and 80 °C is shown in figure 6.19. Given that a different membrane sample was used each time, the pore observed in each sample has a different size and shape. In order to compare the material's rate of expansion for all three temperatures, the diameters measured were normalised and the dimensionless value of $\Delta D/D_0$ was compared, where D_0 is the original diameter at room temperature. This figure shows that the rate of increase in the diameter of the pore is greatest when the Peltier stage was set to 80 °C. This is

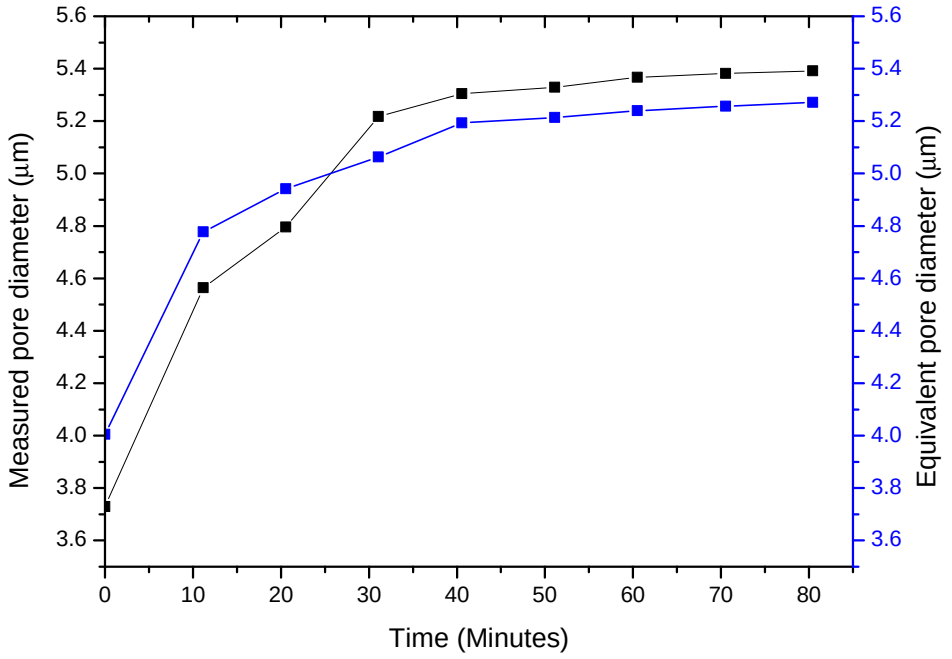

Figure 6.18: Increase in the area of the pore versus time at 80°C

to be expected, as the temperature difference between the sample and the stage was greatest in this instance, so the increase in sample temperature was greatest. The rate of increase was slowest when the stage was set to 60°C. In this case the pore diameter had not stabilised after 80 minutes.

All the data presented here suggests that the membrane pores expand over time when heated, the higher the temperature the greater the overall increase in the size of the pores. Higher temperatures also give rise to a faster rate of expansion, due to a greater temperature gradient leading to a higher rate of heat transfer. Saffarini et al [62], observed an increase in the average pore size of Gore PFTE membranes when annealed at higher temperatures. They also observed a decrease in the Liquid Entry Pressure (LEP) of the membrane at higher temperatures. LEP is defined as [9]:

$$LEP = \frac{-2B\gamma Cos(\theta)}{r_{max}} , \tag{6.4}$$

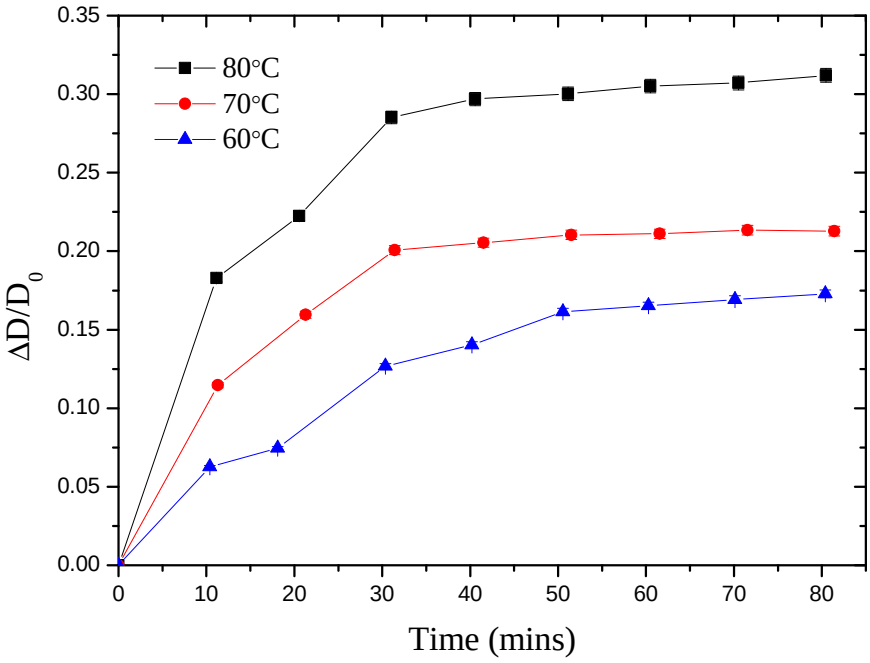

Figure 6.19: Increase in the diameter of the pore divided by the original diameter against time for 60, 70 and 80°C

where γ is the surface tension of the liquid, θ is the contact angle between the liquid and the membrane surface and r_{max} is the maximum pore radius in the membrane; this is the pore most likely for liquid to enter. B is a geometric factor that is determined by the pore's structure. A decrease in LEP at higher temperatures was expected as the surface tension and contact angle decrease with increasing temperature [92] . However the increase in pore size will also lower the LEP.

LEP should be greater than the trans-membrane pressure in the MD module to avoid membrane wetting. It was suggested by the Schneider et al [93], that the pore diameter should not exceed 1 - 1.2 μm to avoid membrane wetting. However figure 6.6 shows that the membrane contains pore diameters greater than this value, 10% of the pores had diameter of 1 μm or above. This was prior to heating and thermal expansion, therefore the increase pore diameter seen at higher temperatures will give greater risk

of membrane wetting.

An increase in pore structure of the membrane material with temperature will have an effect on the performance of an MD system. A decrease in the LEP of the membrane will lead to a greater chance of membrane wetting, and therefore an increase in the conductivity of the distillate produced. However an increase in the average pore size of the membrane should also have a positive effect on the distillate flux. As a larger value of r_{ave} will lead to increased vapour diffusion across the membrane, as shown in equation 5.18.

The rate of expansion of membrane pores during operation within an MD module is expected to be greater than shown in this analysis. As the flux of vapour through the membrane pores will increase the rate of heat transfer to membrane material. Membrane wetting and water intrusion into the pores would also have a significant influence on pore dilation [62].

6.2.3 Temperature rise in the PTFE samples

A lumped system analysis of the heat transfer conduction in the PTFE samples was carried out. A lumped system analysis can be carried out on a object, if the temperature throughout the object can be assumed to uniform [94]. Given that the membrane samples tested are relatively thin, at 0.24mm, this assumption can be made without much loss of accuracy. To determine the rate at which the temperature of the same sample increased and to calculate the heat transfer coefficient for the PTFE membrane inside the SEM, a temperature curve is fitted to data for expansion of the pore shown in the previous section. The start temperature inside of the SEM chamber was known to be 17°C, the final temperature of the sample was assumed to be equal to the set temperature of the Peltier stage when the size of the pores in the sample had reached steady state.

An energy balance between the heat transferred to the sample during time interval dt and the increase in the energy of the sample during the same time interval can be

expressed in the following equation [94];

$$hA_s(T_\infty - T)dt = mC_p dT \ . \tag{6.5}$$

Where m (kg) is the mass of the sample, $A_s(m)$ is the area of the sample, C_p $(J/kg.K)$ is the specific heat capacity of the material and h $(W/m^2.K)$ is the heat transfer coefficient. In this analysis, T_∞ is the temperature of the Peltier stage on which the sample rests. The value for the mass of the sample is equal to;

$$m = \rho V \tag{6.6}$$

where ρ (kg/m^3) is the density of the material and V (m^3) is the volume of the sample. Noting that dT = d(T - T_∞) since T_∞ is always constant, equation 6.5 can be written as:

$$\frac{d(T - T_\infty)}{(T - T_\infty)} = -\frac{hA_s}{\rho V C_p}dt \tag{6.7}$$

Integrating between t=0 when T = T_i to time t=t when T = T+(t), gives the following equation:

$$ln\frac{T(t) - T_\infty}{T_i - T_\infty} = -\frac{hA_s}{\rho V C_p}t \tag{6.8}$$

Taking the exponential of both sides gives;

$$\frac{T(t) - T_\infty}{T_i - T_\infty} = e^{-bt} \tag{6.9}$$

where:

$$b = \frac{hA_s}{\rho V C_p} \tag{6.10}$$

b is the reciprocal of the time constant and has the units, s^{-1}.

By using equation 6.9, the temperature of a sample after time, t, can be determined. As this is an exponential function, the temperature of the sample will increase rapidly at first, and later slow down. This equation can be used to calculate the amount of time taken for the sample to reach T_∞. Altering the value of b changes the curvature of the trend as shown in figure 6.20. The larger the value b, the greater the rate of heat transfer, therefore the sample reaches T_∞ in a shorter time.

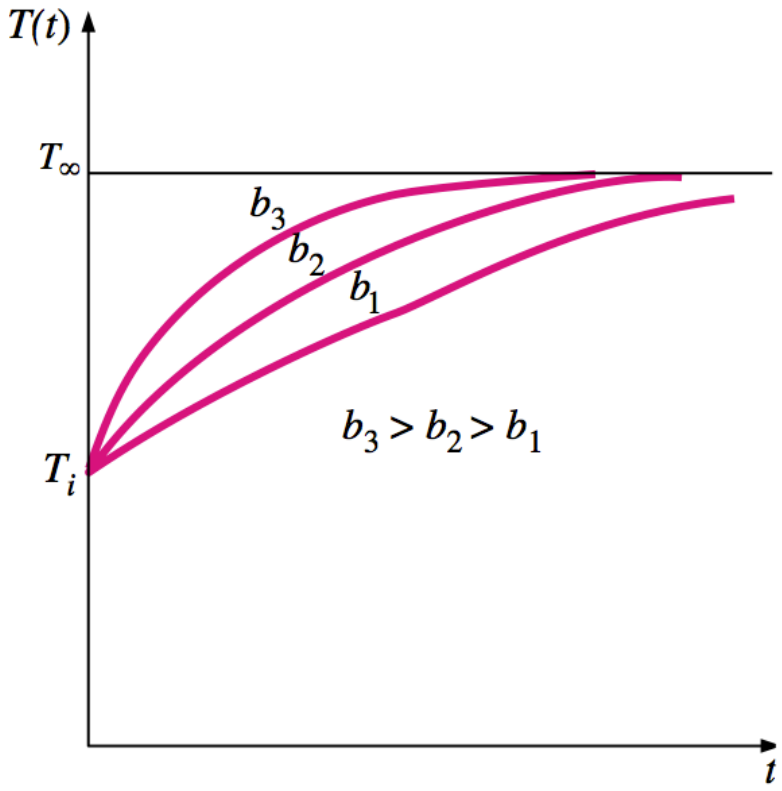

Figure 6.20: The temperature of the sample approaches T_∞ over time, for various values of b

Values of b were selected to fit the curve of T(t) against time, t, to the trends of pore expansion shown in the previous section. T_i is 17°C in all cases, as this is the initial temperature inside the SEM chamber after the vacuum is applied. To investigate the increase in temperature when the Peltier stage was set to 80°C, the trend shown in figure 6.15 was used and 80°C was used as the value for T_∞. The value of b varied,

for each ten minute interval in order to fit exactly to the trend for increase in the pore diameter. Figure 6.21 shows how the value of b obtained from this method varied over the course of the 80 minute experiment.

It is important to note that the peaks seen at 10 minutes and 30 minutes correspond to the periods of rapid expansion in the PTFE material seen in figure 6.19 after 10 and 30 minutes. This expansion is believed to be the result of the phase transitions that occur at 19.2°C and 34.5°C, as discussed in section 6.2.1. This accelerated period of expansion therefore does not correspond to a similarly rapid increase in the samples temperature.

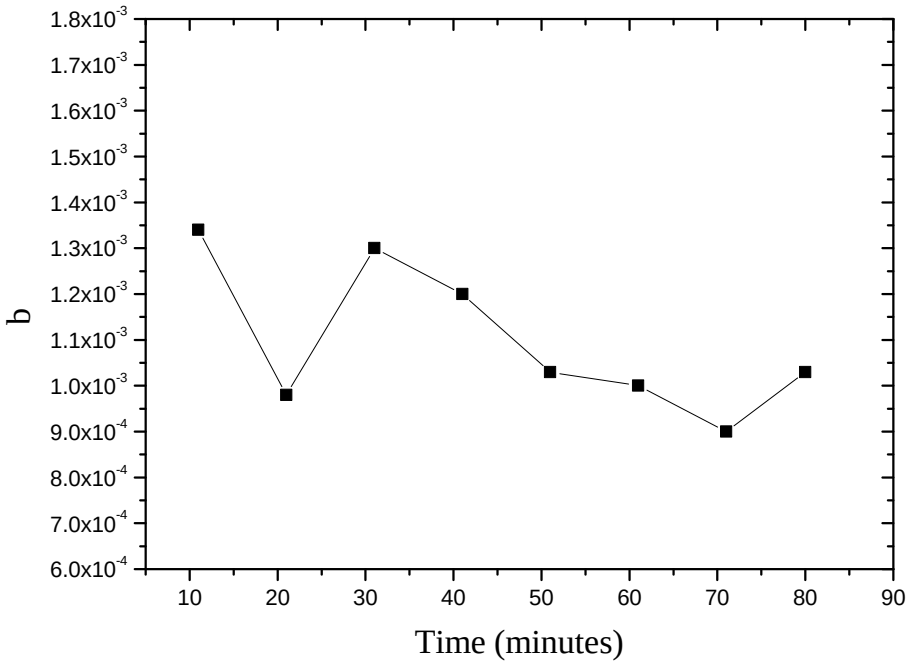

Figure 6.21: Values for b over time, when $T_\infty = 80°C$

A single value of b was obtained by taking the average of the final five points on the graph. This method was preferred, as the heat transfer coefficients found during the first 30 minutes have been influenced by the phase change transitions at 19.2°C and 34.5°C. However it is noted that the uncertainty in b increases as the T(t) approaches

T_∞ as the ΔT between time intervals decreases. For this analysis the average value of b was found to be 1.032 x10^{-3}.

By substituting values for the specific heat capacity and density of PTFE, along with the area and volume of the sample into equation 6.21 and rearranging, the heat transfer coefficient, h, was obtained. When calculating the volume of material, the percentage porosity was also taken into account. The following equation was used;

$$V_{sample} = A_m * \delta_{membrane} * \phi, \tag{6.11}$$

property	value	units
Specific heat capacity, C_p	1090	J/kg K [95]
Density, ρ	2200	kg/m^3 [90]
Area, A	2.5 x 10^{-5}	m^2
Volume, V	5.04 x 10^{-9}	m^3

Table 6.1: Properties of the Gore^{TM} PTFE samples

where $\delta_{membrane}$ (mm) is the thickness of the membrane and ϕ is the porosity of the membrane, as defined in equation 6.1. The relevant information on PTFE material is shown in table 6.1. Using these values and the average value of b, the heat transfer coefficient, h, was found to be 0.62 W/m^{2}K. This low value for h is to be expected considering heat conduction into a thermoplastic such as PTFE and given that it took 80 minutes for $T(t)$ to increase to a value near to T_∞. Also, poor contact between the membrane and the stage could be a factor.

Figure 6.22 shows a plot of T(t) against time for T_∞ equal to 80°C, calculated using the average value of b, 1.032 x 10^{-3}. The figure also shows the expansion of the pore diameter divided by the original pore length over time. The curve produced when using the average value of b gives a lower value of $T(t)$ at 10 and 30 minutes, than the corresponding point on the ΔD/D$_0$ curve.

Values of b were selected to fit the curve of T(t) against time, t, to the trends of pore expansion when the Peltier stage was set to 70°C, shown in figure 6.13. Again

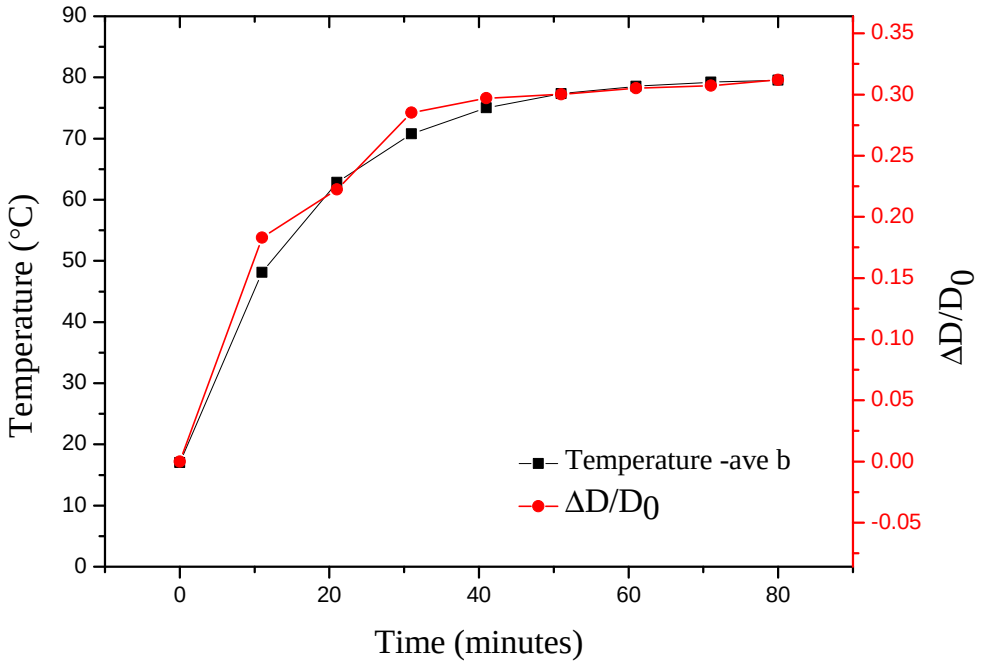

Figure 6.22: T(t) against time for when $T_\infty = 80°C$, based on average value of b

T_i was 17°C and a values of 70°C was used for T_∞. The value of b obtained from this method varied over the course of the 80 minute experiment. Figure 6.23(a) shows the values of b required to fit the curve accurately to the trend of pore expansion over the course of the 80 minute experiment.

The value of b was determine by averaging the final five points on the figure, it was calculated as 1.110 x10^{-3} s^{-1}. As before, equation 6.10 was used to calculated a the heat transfer coefficient based on this average value of b; it was found to be 0.67 W/m^2K. This is in agreement with the heat transfer coefficient calculated for the sample that was heated to 80°C. It was expected that the value of h should be the similar, as the samples used are made of the same material and therefore have the same properties. The energy transferred to the sample was less as the stage was only set to 70°C, however the final temperature of the sample T_∞ was also lower,therefore using the energy balance equation, 6.5 , the values of h should be the similar.

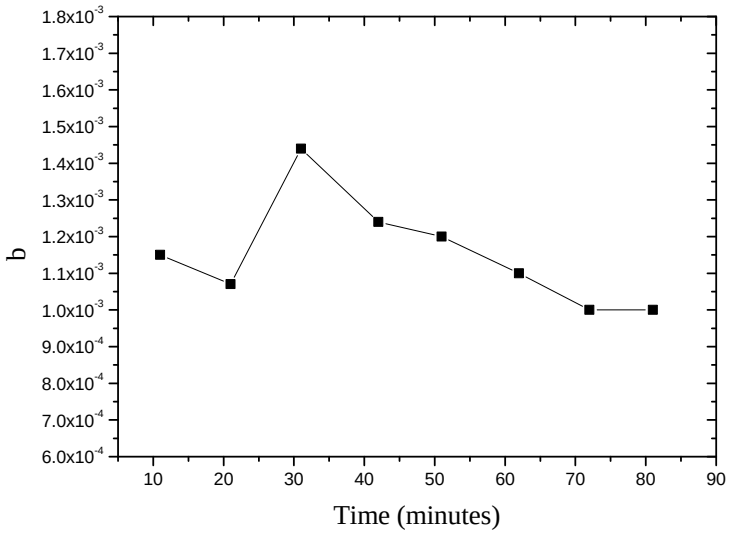

(a)

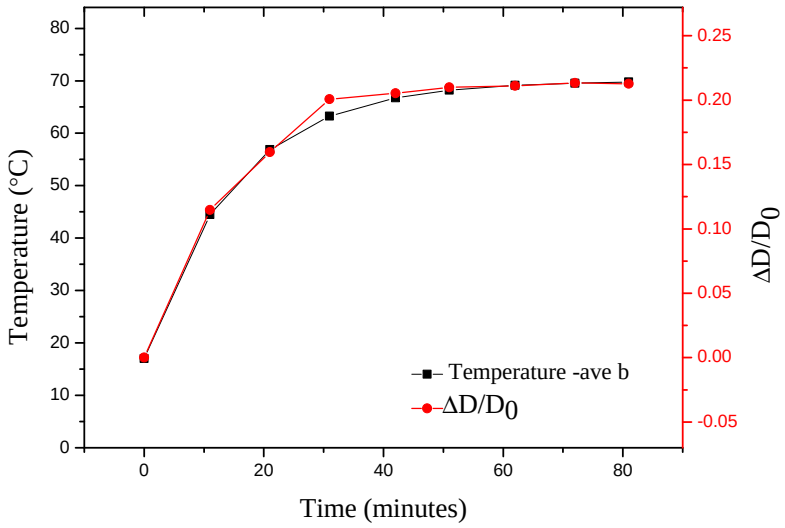

(b)

Figure 6.23: a) shows the values for b over time when $T_\infty = 70°C$, and b) T(t) against time for when $T_\infty = 70°C$, based on average value of b

Figure 6.23(b) shows T(t) against time for when T_∞ was 70°C, calculated using on the average value of b for the first 40 minutes, 1.110 x10^{-3} s^{-1}. Using the average value of b provides a good match. The temperature at 30 minutes is lower than the

corresponding point on the curve for $\Delta D/D_0$. This due to selecting an average value of b in the final 50 minutes and therefore removing the periods of rapid expansion due to the solid state transition of the material.

Figure 6.24(a) show the values of b used to fit a curve of T(t) against time for the data when the sample was heated to 60°C inside the SEM chamber. In this instance the curve steadies out in the final 30 minutes. This is because when the sample was heated to 60°C, the pore diameter as measured from the SEM images continued to expand throughout the duration of the 80 minute experiment.

An average value for b was calculated to be 6.960 x 10^{-4} s^{-1}. This value is lower than the in previous experiments when the sample was heated to 80°C and 70°C. This will therefore yield a lower value for the heat transfer coefficient. In this case it was found to be 0.42 W/m^2K. This value is 38% lower than in the previous two experiments. There are several possible reasons for this lower heat transfer coefficient. Firstly, the feature observed in the experiment when the Peltier stage was set to 60°C is considerably larger than the features observed at 80°C and 70°C. It appears that the pore has expanded predominately across its width, rather than along the height of the pore. It is possible for the pores to become misshapen in this way when expanding, given the none uniformity of the strands and nodes that form the pores.

It is also possible that the material may not have been in good contact with the Peltier stage during the operation. Although the sample was stuck down to the stage before being placed inside the SEM chamber, it can be come dislodged when the air is pumped out of the chamber to provide the vacuum.

Figure 6.24(b) shows T(t) against time for when T_∞ was 60°C, calculated using on the average value of b, 6.960 x10^{-4} s^{-1}. The two trends are in good agreement with each other, particularly in the final 30 minutes of the experiment.

The rate at which the pores expand inside of the SEM chamber, will be different to the rate seen inside of an MD module when in operation, given the very different conditions. The PTFE material is expected to expand quicker when used inside an MD

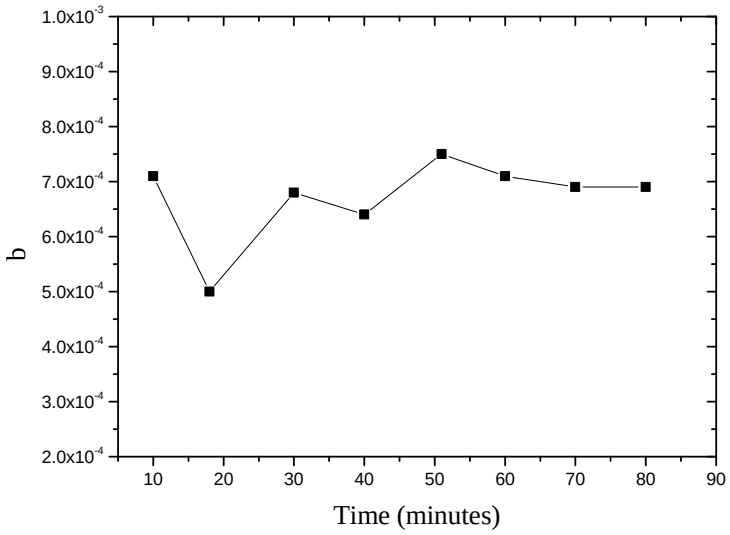

(a)

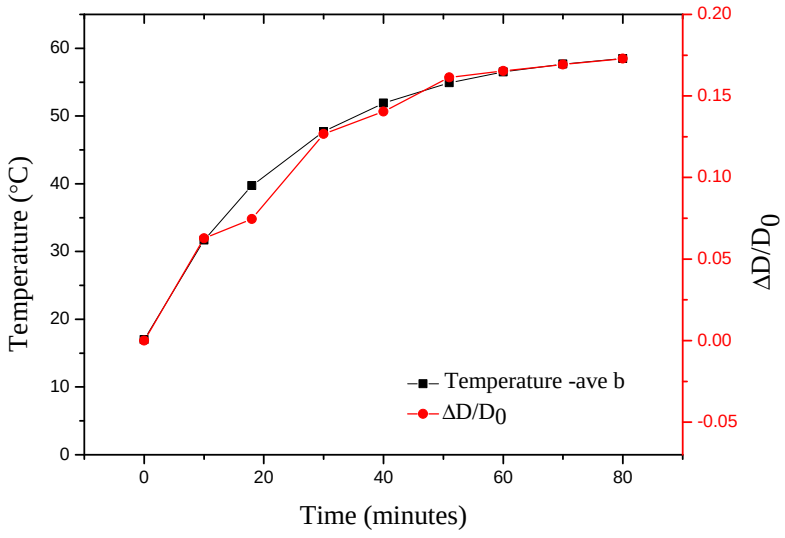

(b)

Figure 6.24: a) shows the values for b over time when $T_\infty = 60°C$, and b) T(t) against time for when $T_\infty = 60°C$, based on average value of b

module. Given that vapour flux will diffuse through the pores, giving heat transfer by convection as well as conduction. Whereas, when placed on the stage inside the SEM heat transfer occurs via conduction only. Therefore the heat transfer coefficient would

be greater in the MD module and the sample would heat up to the temperature of feed solution in less time.

6.3 Conclusions

This chapter investigates the change in membrane microstructure when the temperature of the sample was increased. The structure of the membrane was established at an ambient temperature of 17°C. SEM image analysis was used to measure the porosity of the sample, which was found to be 84 ± 4% . This value was comparable to the porosity value of 80%, stated by the manufacturer, which was determined by capillary flow porometry. Analysis of the membrane under magnification showed that the pores are not evenly distributed across the surface of the membrane. A large variation in the size of the pores within the sample was seen. These values range from 0.12 - 1.88 μm, and the average value was 0.51 ± 0.32 μm. However a frequency distribution analysis gave a modal value of 0.3 μm, closer to the 0.2 μm quoted by the manufacturer.

A Peltier stage was used to heat the membrane samples inside the SEM chamber. The microstructure of the membrane was observed as the temperature of the sample increased. It was found that the pores expanded over time when heated. The temperature of the sample was originally 17°C, it was then place on a Peltier stage with a temperature of 80°C and imaged every ten minutes. The length of the pore increased from 3.729 μm/cm to 5.367 μm/cm over a 60 minute period. The rate of expansion slowed drastically after 40 minutes and was stable in the final 20 minutes of the experiment. From this it is possible to conclude that the sample had reached the same temperature as the Peltier stage. When the sample was heated from 17°C to 60°C, the pore length increased from 8.156 μm/cm to 9.762 μm/cm over a 60 minute period. However the pore size continued to increase over the 80 minute experiment, suggesting that it had not heated to 60°C in that time.

The increase in pore size is thought to be the result of the thermal expansion of the membrane material when heated. The overall increase in pore size was proportional

to the temperature of the stage; higher temperatures gave larger expansion. The rate of expansion was greatest for higher temperatures, as the larger temperature gradient gave higher heat transfer rates.

A lumped system analysis of the heat transfer inside the SEM chamber was used to determine a heat transfer coefficient of 0.62 W/m^2K and 0.67 W/m^2K, when it was heated to 80°C and 70°C, respectively. From this analysis the relationship between increase in temperature and increase in pore length was established.

From this analysis we can conclude that the change in membrane temperature during intermittent use and subsequent change in the pore size will influence the performance of an MD module. When a membrane module is shut down for an over night period, as is the case with solar powered MD systems, the temperature of the membrane will decrease to ambient. When operation begins the next day, the membrane will be heated to the temperature of the feed, usually between 60°C and 80°C, causing the pores to expand. This change in pore size will influence the quantity and the quality of the distillate yield. Larger pore size will lower the Liquid Energy Pressure of the membrane, making membrane wetting more likely. Therefore the quality of the distillate produced could potentially decrease. However larger pores will give greater diffusion of vapour across the membrane and therefore an improvement in the distillate flux would be expected.

These ideas are investigated further in the following chapter. The system is cleaned and left to cool over night. The quantity and quality of distillate produced from the bench scale MD system is then measured during the first 80 minutes of operation, while the system is heated. The influence of heating the membrane and resulting increase in pore size is investigated, in terms of the distillate flux and conductivity produced during the initial start up of the system.

Chapter 7

Membrane performance during start up

In this chapter the initial start up performance of a bench scale MD system is investigated under constant operating conditions after an overnight shut down period. All input parameters such as feed temperature, feed conductivity and feed flow rate are held constant. However it was observed that the distillate flow rate and conductivity changed during the first hour of operation.

The initial start up period was investigated for a range of hot inlet feed temperatures from 60-80°C, to determine the influence of temperature on the time taken for the module to reach steady state. The effects of intermittent use of the system, and the

subsequent heating and cooling of the module are also investigated. Both the G02 and G04 membranes were tested and the results are reported in this chapter.

7.1 Performance of the system during the start up period

Before each experiment the system was washed out with de-ionised water, emptied and left to dry overnight. At the start of each experiment the system was switched on and operated with all input parameters kept constant. The feed flow rate was constant at 0.6 l/min throughout all experiments. The salt concentration of the feed solution was also kept constant at 35 g/l. The temperature at the inlet of the hot channel was kept constant for the duration of each individual experiment. A range of inlet temperatures from 60-80°C were investigated. The distillate flux and distillate conductivity were monitored during the first 80 minutes of operation.

7.1.1 G02 membrane

Before entering the hot channel of the MD module, the feed solution was heated to a desired temperature by passing through a coil placed inside a hot water bath. The temperature at the hot channel inlet was maintained at 60°C. The temperature at the inlets and outlets of both the hot and cold channels were recorded and are shown in figure 7.1. The trans-membrane temperature difference gives rise to a vapour pressure difference, which is the driving force for mass transfer across the membrane. The trans-membrane temperature reported in this study is defined as;

$$T_{trans-membrane} = \left(\frac{T_{hot,in} + T_{hot,out}}{2}\right) - \left(\frac{T_{cold,in} + T_{cold,out}}{2}\right) \tag{7.1}$$

The transmembrane temperature is also plotted on figure 7.1. 3 minutes after the pump was switch on and the feed solution began to flow through the system, the temperature at the inlet of the hot channel reached 60°C. The temperatures established throughout the system reached a steady state and remained constant after this time.

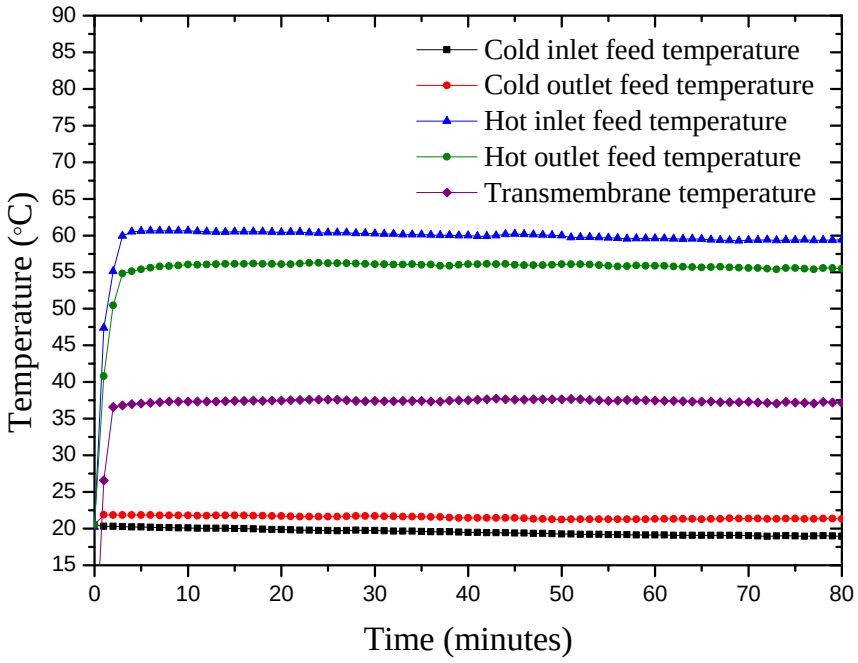

Figure 7.1: Temperatures of the MD channels when the hot inlet is maintained at 60°C

The flux and conductivity of the distillate during the first 80 minutes of operation are shown in figure 7.2. Distillate produced during operation flows from the MD module and into a well fitting that contains a conductivity probe; the probe and fitting are shown in figure 4.3. Distillate then flows out of the fitting and into a beaker placed on a weight scale. The increase in weight recorded by the scale is converted into a value for distillate flux.

Figure 7.2(a) shows a 13 minute delay before the distillate began to flow into the beaker. The MD process has an inherent response time; after the feed begins to flow through the hot channel of the module vapour must form at the surface of the membrane. This vapour must then diffuse through the pores and condense in the distillate channel in sufficient quantities to flow out. However in this set up the delay is also partly due to the need to fill the small well fitting containing the conductivity probe. The fitting is necessary to measure the distillate conductivity, as the small

membrane surface area within the bench scale MD unit produces low distillate flow rates. For the probe to measure conductivity it must be fully submerged therefore the well must be full, the fitting can been seen in figure 4.3. To assess the time delay introduced by the conductivity probe and fitting, they were removed from the set up and the module was operated under the same conditions, with a hot inlet temperature of 60°C and a feed flow rate of 0.6 l/m. The time taken for distillate to flow directly from the outlet of the module was found to be 6.5 minutes. Therefore it is assumed that the fitting took 6.5 minutes to fill, and the rate at which it filled in that time is not known.

After 13 minutes the distillate flux shows a gradually increasing trend. The low distillate flow rates produced by the small MD unit results in spikes in the distillate flux trend. This is due to surface tension within the outlet line, causing the distillate to gather as droplets before dropping onto the scale. However there is a gradual rise in the distillate flux during the experiment, as shown on figure 7.2(a). The average distillate flux between 20-30 minutes was 1.63 l/m^{2}h. Between 70 - 80 minutes of operation the average distillate flux had increased to 1.90 l/m^{2}h. This is an increase of 24%. All of the operating conditions remained constant during this time. Therefore the increase in distillate flux could be attributed to the response time of the expansion of the membrane pores as they are heated, leading to an increase in the average pore size over time. This would result in greater vapour diffusion across the membrane, as mass transfer through the membrane pores is directly related to pore size. The relationship between mass flux and pore size is defined as [9]:

$$N \propto \frac{r^a \phi}{\delta_m \tau} \tag{7.2}$$

Where N is the molar flux of water vapour, and r is the mean pore size and the factor a is equal to 1 or 2 for Knudsen diffusion or viscous flow respectively. δ_m is the membrane thickness, τ is the membrane tortuosity and ϕ is the membrane porosity. This equation highlights the importance of the effect the pore size on the molar flux

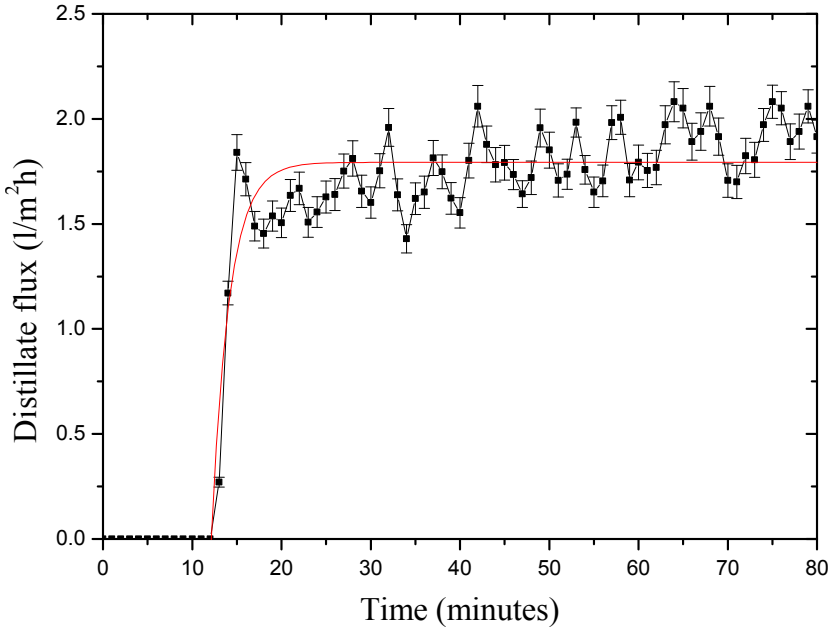

(a)

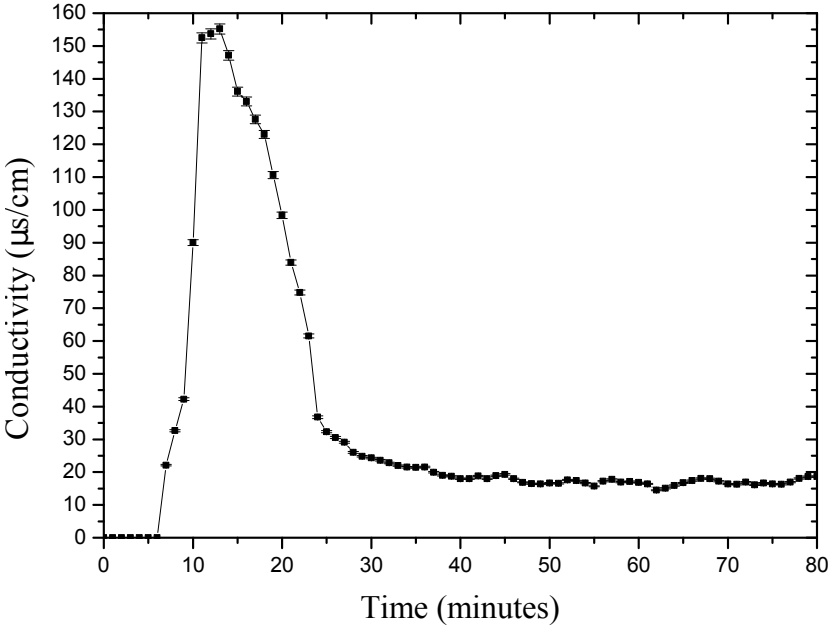

(b)

Figure 7.2: Distillate flux and distillate conductivity during start up period, when the hot inlet temperature is set to 60°C

of vapour, particularly when the diffusion mechanism transits between predominately Knudsen to a Knudsen-viscous process. Knudsen diffusion occurs when the mean free

path of a molecule is larger than the diameter of the pore through which that molecule diffuses [96]. This results in a large number of interactions between the molecule and the wall of the pore. The mean free path of saturated water at 60°C is 0.7μm. For air filled pores of approximately 0.5 μm collisions occur as frequently between the molecule and the wall of the pore, as they do between the molecules themselves, therefore Knudsen diffusion must be considered [9]. For pores greater than this, viscous flow will be the dominant diffusion process. Therefore as the membrane is heated, a corresponding increase in pore size will result in increased distillate flux, particularly for the pores that expand beyond the 0.5 μm threshold.

The distillate conductivity, shown in figure 7.2(b), has the same initial zero value as seen with the distillate flux. The conductivity began to rise after 6 minutes, when the well fitting began to fill. A maximum conductivity of 146 μS/cm was recorded after 13 minutes when the well was full and the probe fully submerged. The conductivity started to decrease after 13 minutes, when distillate began to flow out of the fitting. The decrease indicates that the distillate entering the fitting had a lower conductivity, therefore diluting the content of the well fitting. The conductivity then rapidly decreased until 30 minutes after the pump was switched on, after which the rate of decrease slowed. It became stable after 50 minutes of operation, varying by $\pm$1% thereafter. The average conductivity in the final 30 minutes of the experiment was 16.89 μS/cm. This is far in excess of the 3 minute response time of the conductivity probe when in the fitting, as shown in 4.4. Therefor it can be concluded that change in conductivity is gradual, and could be attributed to the change in average pore size of the membrane as it is heated.

It is important to note that the decrease seen in distillate conductivity indicates that the increase in distillate flux, shown in figure 7.2(a), is not the result of membrane wetting. Membrane wetting occurs when the Liquid Entry Pressure (LEP) of the membrane pores is exceeded and saline liquid is able to cross the membrane. This would result in added volume in the distillate channel; it would also cause significant

rise in distillate conductivity. This effect was demonstrated in the results reported by Guillen-Burrieza et al [97, 98], after the module had undergone 4 weeks of intermittent use. This effect was attributed to scaling of the membrane. However an increase in membrane wetting was not seen during the first hour of operation.

A similar decrease in distillate conductivity during the first hour of operation has been reported by other MD researchers[11, 97]. This suggests that although the bench scale MD module used in this study contains only a small membrane surface area the effect observed is comparable to that of significantly larger systems. Winter et al [11], proposed that this effect was due to contamination of the membrane during the manufacturing process. However this trend is seen after multiple uses and when the membrane module is flushed out before and after use. Guillen-Burrieza et al [97] suggested that intermittent use of the MD module could be the cause of the initial high distillate conductivity values observed. When a membrane dries and cools, particularly after being operated at maximum temperatures, salt crystals can form on the surface of the membrane and through the pores, resulting in a worsening of the distillate quality. Constant operation of the module results in continuous evaporation and diffusion through the pores, and therefore better distillate conductivity values. Guillen-Burrieza et al [98] later explored the effect of intermittent operation on the fouling of PVDF and PTFE membranes. They investigated salt formation on the surface of the membrane and within the membrane pores. They also looked at the longer term effects of intermittent use over a 4 week period. Cross-sectional images of the membrane were taken using SEM after 4 weeks of use. The images show a layer of salt deposition on the surface of the membrane, as well as some crystal formation within the membrane pores. This indicates that membrane wetting occurred.

However during the course of this research the membrane system was flushed out with de-ionised water after each experiment. This would drastically reduce the build up of salt scaling on the surface of the membrane. It is still possible that saline liquid within the pores could remain after cleaning. To overcome this issue the de-ionised

water was heated to 80°C before entering the hot channel of the module, producing ultra-pure distillate and flushing out the pores in the process.

The decrease in distillate conductivity could be a result of the temperature effect on the microstructure of the membrane. The previous chapter demonstrated that the pores of the PTFE membrane expand when heated. An increase in pore size will lower the LEP of the membrane, defined in equation 6.4. This would have an adverse effect on the quality of the distillate, as membrane wetting would be more likely and therefore higher distillate conductivity would be expected [62]. Given the decrease in distillate conductivity observed during this experiment, it is assumed that the change in LEP is negligible.

The decrease in conductivity could be attributed to the increase in distillate flux observed during the first hour of operation. This effect is thought to be due to an increase in pore size, resulting in greater vapour diffusion across the membrane. The greater volume of pure water vapour across the membrane would further dilute any liquid salt solution that was able to pass through the pores. Given that a decrease in conductivity is observed, it can be concluded that greater diffusion is the dominant process when pore size increases, giving an overall beneficial effect. However an optimum pore size is likely to exist, after which the decrease in LEP would become the dominant effect. The membrane must have a pore size large enough to produce adequate distillate flux, however small enough to minimise membrane wetting [9]. Therefore when selecting an appropriate membrane, the average pore size of the membrane at optimum working temperature of 80°C should be considered rather than the pore size at room temperature.

When the inlet temperature of the hot channel was maintained at 70°C, the temperatures at the inlets and outlets of the channels were recorded and are shown in figure 7.3. The temperatures stabilised 3 minutes after the pump was switched on and remained constant for the duration of the experiment thereafter.

The distillate flux and conductivity are presented in figure 7.4. With the

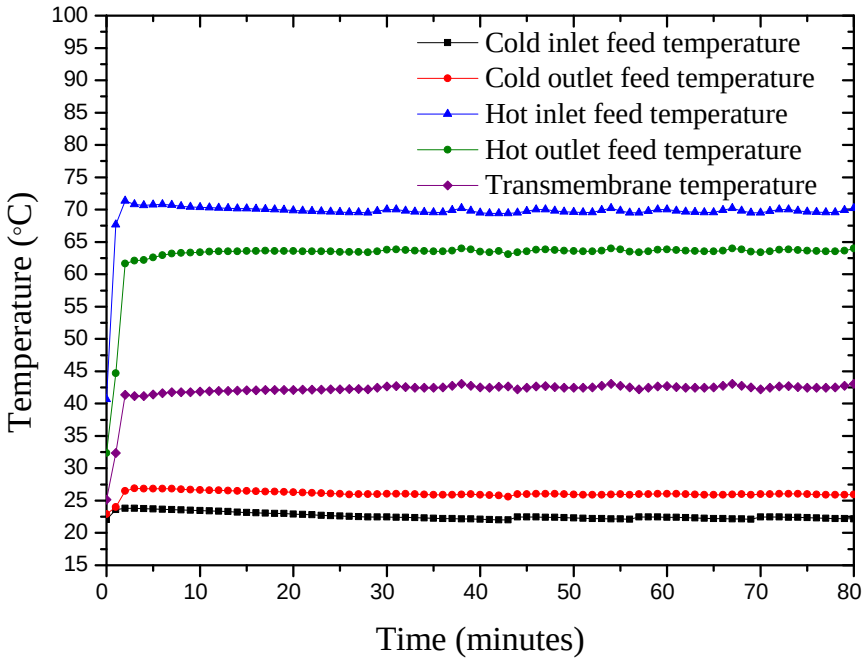

Figure 7.3: Temperatures of the MD channels when the hot inlet is maintained at 70°C

temperature of the feed entering the hot channel set to 70°C, it took 9 minutes for distillate to flow out of the fitting and the flux to be measured. Operating under the same conditions, with a hot inlet feed temperature of 70 °C without the conductivity probe and fitting, it took 5 minutes for the module to produce distillate. Therefore it is assumed that it took 4 minutes to fill the conductivity fitting. The greater flux at higher temperatures means in took less time to fill the well than when the system was operated at 60°C.

As before, the flux increased gradually throughout the experiment; this is shown in figure 7.4(a). The average distillate flux between 20 - 30 minutes was 3.69 l/m^{2}h. In the final 10 minutes of the experiment the distillate flux had increased to 4.19 l/m^{2}h. The increase of 0.50 l/m^{2}h is greater than 0.27 l/m^{2}h rise in distillate flux seen in figure 7.2(a). This suggests that the increased distillate flux is related to the temperature effecting the size of the membrane pores. In the previous chapter it was demonstrated

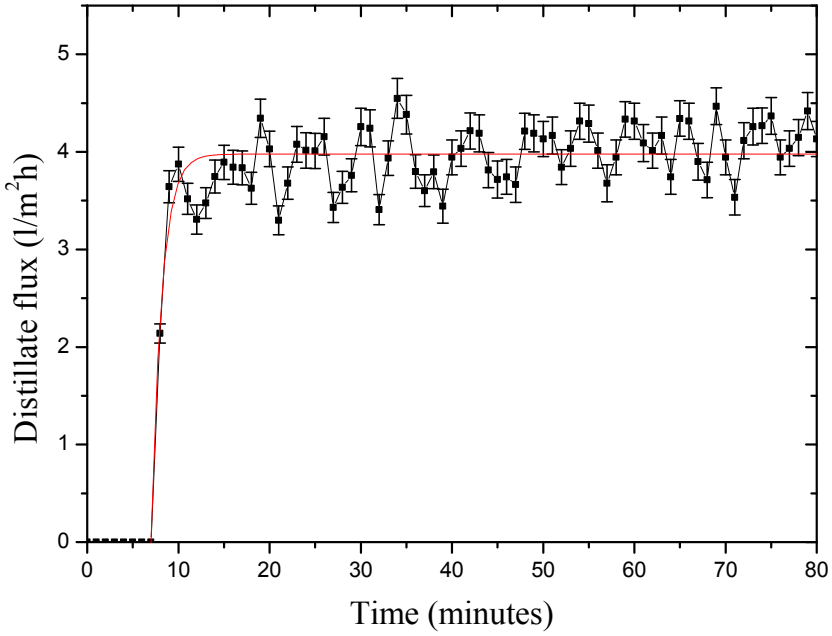

(a) Distillate flux

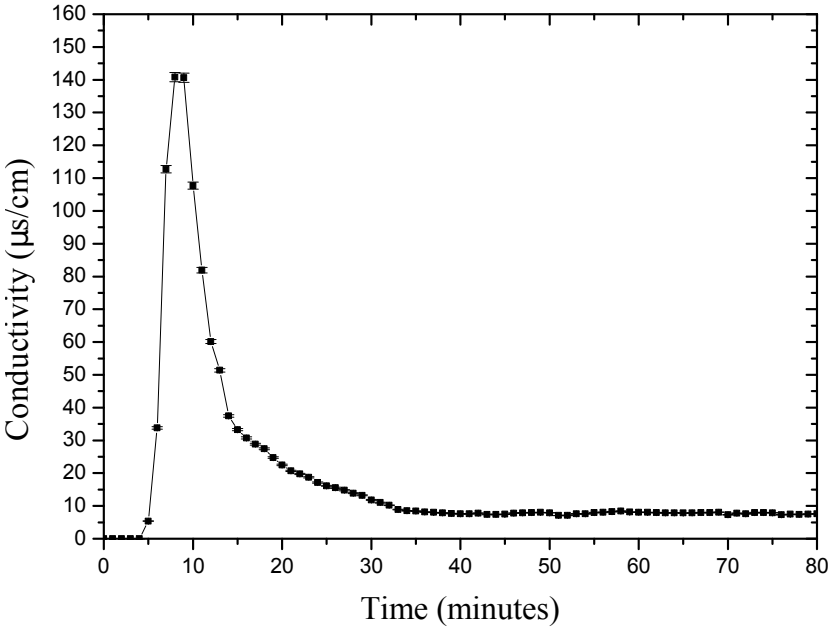

(b) Distillate conductivity

Figure 7.4: Distillate flux and distillate conductivity during start up period, when the hot inlet temperature is set to 70°C

that greater expansion of the pores is seen at higher temperatures, as shown in figure 6.19. Greater increase in pore size would result in a larger increase in vapour diffusion

across the membrane and higher distillate flux.

The conductivity of the distillate is reported in figure 7.4(b). The conductivity value began to increase after 5 minutes, when the well fitting began to fill. Again this took less time than when the hot inlet temperature was 60°C. After 9 minutes the conductivity began to decrease rapidly, and became stable after 30 minutes. From 30 - 80 minutes the average conductivity was 7.75 μS/cm. The rate of decrease was much greater at 70°C; this could be explained by the faster rate of thermal expansion of the membrane pores. This is due to a larger temperature gradient and higher rate of heat transfer. The stable value of conductivity was lower at 70°C than at 60°C. This could be attributed to the larger increase in flux and therefore greater dilution of feed liquid entering the pores.

When the feed solution entering the hot channel was maintained at 80°C, the temperatures at the inlets and outlets of the channels were recorded and are shown in figure 7.5. The average trans-membrane temperature was 51.1°C.

The distillate flux and conductivity over the first 80 minutes of operation are shown in figure 7.6. It took 6 minutes for the distillate to flow out of the fitting. Without the fitting in place while operating under the same conditions it took 3 minutes for distillate to be produced by the module. For the 10 minutes after the flow was established the average distillate flux was 6.40 l/m^{2}h. The distillate flux gradually increased over the course of the operation. For the final ten minutes of the experiment the average values are 7.11 l/m^{2}h, an increase of 0.71 l/m^{2}h. This increase in distillate flux is greater than in the previous experiments, where the temperature of the hot channel inlet was 60 and 70°C. This could be attributed, again, to the increase in pore size as the membrane is heated, as higher temperatures causing greater expansion of the pores.

Figure 7.6(b) shows the distillate conductivity during the first 80 minutes of operation. After 3 minutes the conductivity began to rise as the well filled with distillate, by 7 minutes the well was full and distillate flowed out of the fitting onto the scale. The conductivity then began to decrease rapidly in the first 20 minutes. After

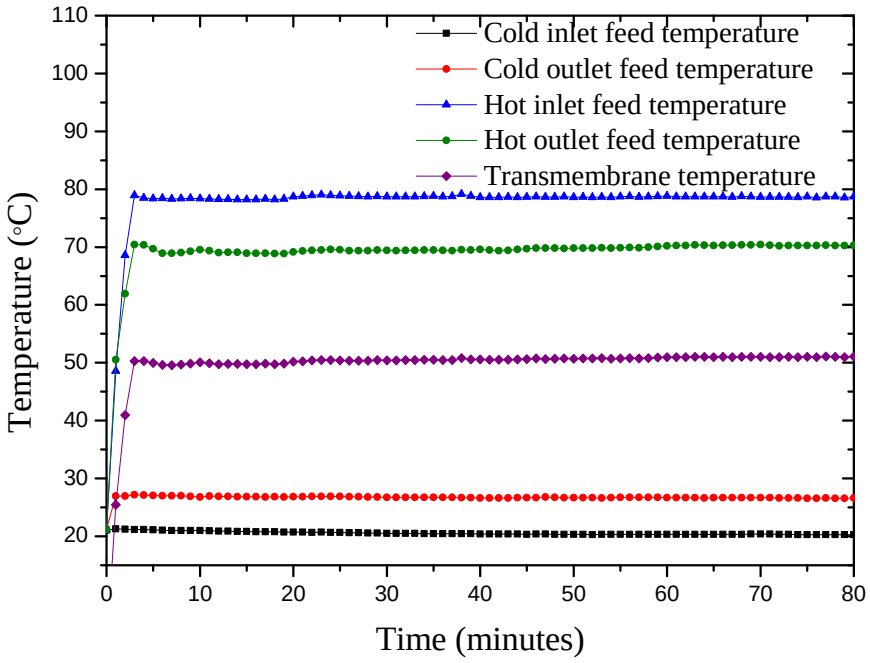

Figure 7.5: Temperatures of the MD channels when the hot inlet is maintained at 80°C

30 minutes the conductivity value had stabilised, with an average value of 3.78 μS/cm from 30 - 80 minutes. This value is similar to those reported by Winter et al [11], for 10 m^2 and 14m^2 spiral wound modules made with the same PTFE Gore^{TM} membranes. Several experiments were conducted with a feed solution of 35g/l (approximately 40,000 μS/cm) heated to 80°C; the conductivity of distillate produced after 1.5 hours of operation varied between 2 - 3.5 μS/cm. Experiments were conducted with feed salinity up to 105g/kg and almost no dependance was found between this parameter and the distillate conductivity.

As mentioned previously, Winter el al, [11], also reported a rapid decrease in conductivity of the distillate at the start of each experiment. They reported data for the 10 m^2 spiral wound module when operated with a feed salinity of 50μS/cm, which was also heated to 80°C. The results show a similar trend to that in figure 7.6(b). A rapid decrease occurred during the first 15 minutes of the experiment.

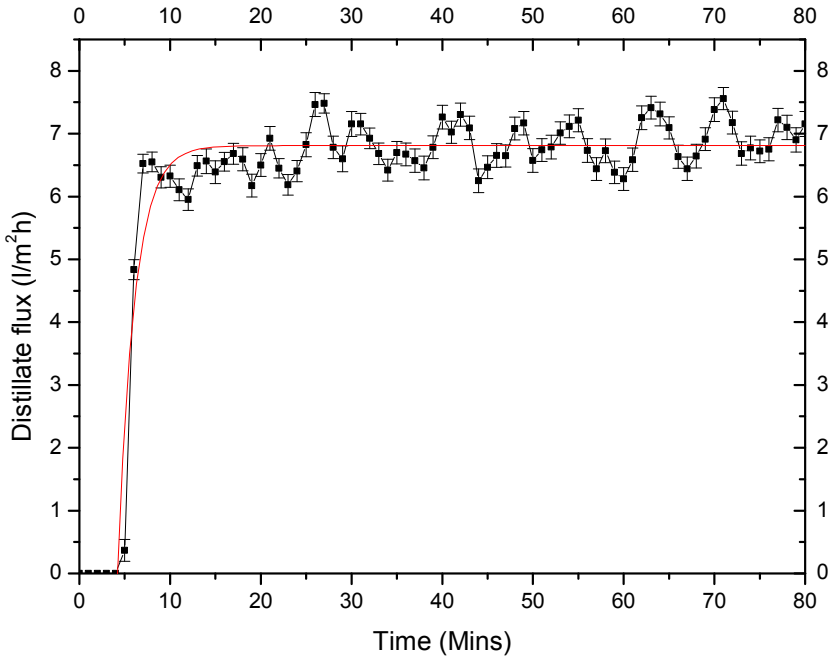

(a) Distillate flux

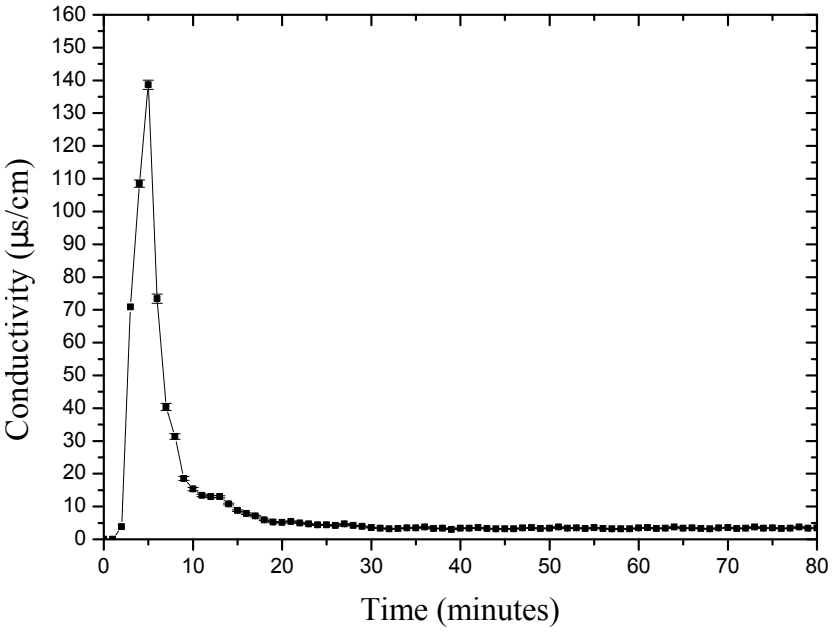

(b) Distillate conductivity

Figure 7.6: Distillate flux and distillate conductivity during start up period, when the hot inlet temperature is set to 80°C

It is was observed during the course of these experiments that the rate of decrease in the distillate conductivity during the initial start up period is greater for higher

temperatures. Figure 7.7 shows the conductivity over time, when the system was operated at constant temperatures of 60, 70 and 80°C. The start time was set to when distillate was flowing through the fitting. The conductivity decreased most rapidly when the feed entering the hot channel was at 80°C. When referring to the lumped system analysis of heat transfer conducted in the previous chapter, equation 6.5 shows that an increase in T_∞, which is in this instance the temperature of the feed, will cause the membrane material to heat up quicker. This will increase the rate of expansion of the pores, yielding a greater distillate flux, which will in turn cause the distillate conductivity to decrease more rapidly.

The greatest overall decrease in conductivity was also seen at 80°C. When operating with a feed solution of 60°C the overall decrease in conductivity was lower. This suggests that there is a link between decrease in conductivity during the start up period and the temperature effect on the microstructure of membrane, as figure 7.7 has a similar trend to figure 6.19, where the higher temperature of the Peltier stage inside of the SEM chamber resulted in overall greater expansion in the membrane pores. The larger pores result in greater vapour flux across the membrane, further diluting the distillate and resulting in lower conductivity.

The rate of expansion in the pore size when heated to 80°C in the SEM chamber was lower than the rate of decrease in the conductivity of the distillate flux when the module was operated with a feed temperature of 80°C. In the SEM chamber, when heated to 80°C, a rapid expansion of the pores was observed over 30 minutes, however the decrease in conductivity of distillate occurs in 10 minutes. However this is to be expected as the sample in the SEM chamber was dry, inside a vacuum and heated on one side by the Peltier stage. When membrane is heated to 80°C during operation on the MD module, there is a vapour flux through the pores and the temperature on the air-gap side is expected to be greater than the ambient temperature. This will result in a greater rate of heat transfer to the material, and a greater rate of expansion of the material. As the material expands the pore size increases, therefore the temperature

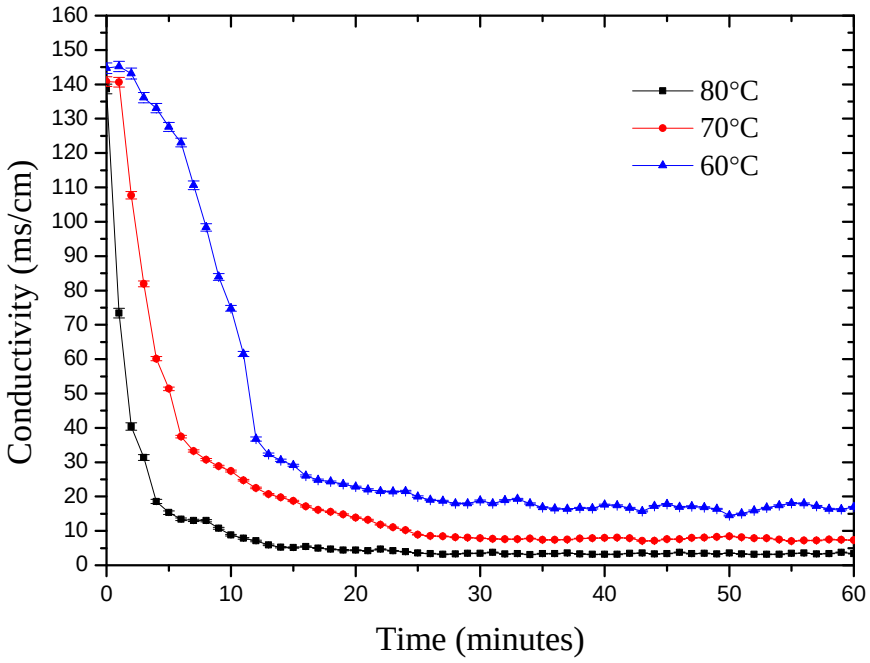

Figure 7.7: Comparison of the rate of decrease in the distillate conductivity for hot inlet temperatures of 60, 70 and 80°C

of the material and the average pore size of the membrane are directly linked.

7.1.2 G04 membrane

A similar experiment was carried out with the Gore^{TM} G04 membrane. The same feed flow rate of 0.6 l/m was used and the feed salt concentration was also the same at 35 g/l. The feed temperature into the hot channel was maintained at 80°C. The temperature of the inlet and outlet of both channels were recorded and are presented in figure 7.8. The average transmembrane temperature recored was 56.2°C. This is 5.1°C higher than the average transmembrane temperature for G02 membrane when operated with an inlet temperature 80°C. Although the inlet temperature was maintained at 80°C in both experiments, the temperature of the cold feed inlet is lower in figure 7.8, giving a greater transmembrane temperature.

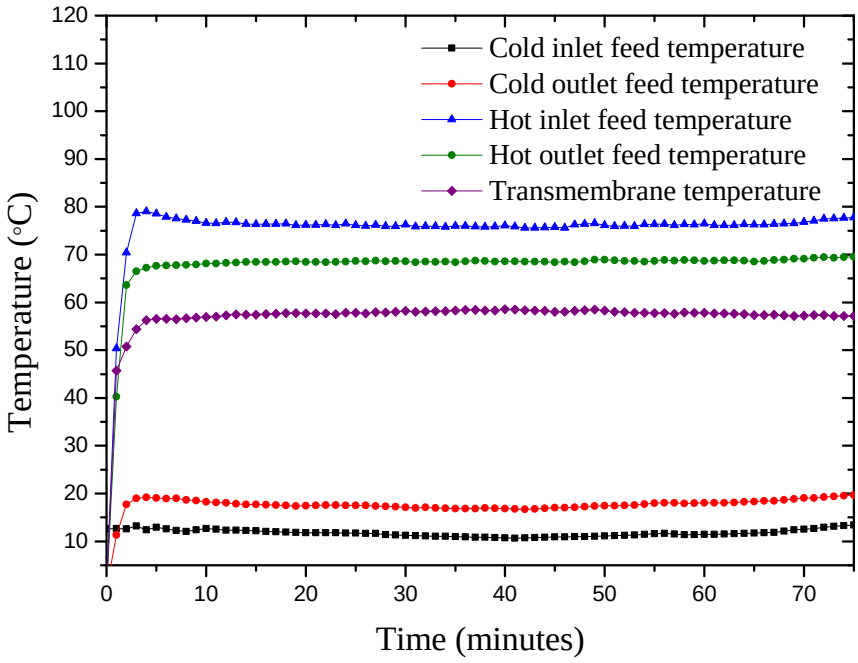

Figure 7.8: Temperatures of the MD channels when the hot inlet is maintained at 80°C, with G04 membrane

Figure 7.9 shows the distillate flux and conductivity for the G04 membrane. The distillate flux shows the same gradual increase over the course of the experiment. The average flux between 10 - 20 minutes was 6.61 l/m^{2}h. For the final 10 minutes of the experiment the average flux had increased to 7.39 l/m^{2}h. Both the initial and the final value for distillate flux are higher than seen the with the G02 membrane when operating under the same conditions, shown in figure 7.6. This is expected, as the larger average pore size of the G04 membrane yields greater flux.

The distillate flux from G04 membrane is shown in figure 7.9(b). The highest value of conductivity recorded was 230 μS/cm, after 5 minutes of operation. The distillate conductivity reduced and became stable after 30 minutes. The average conductivity of the distillate in the final 30 minutes of operation was 175μS/cm. The starting conductivity was higher than when using the G02 membrane. The final steady state

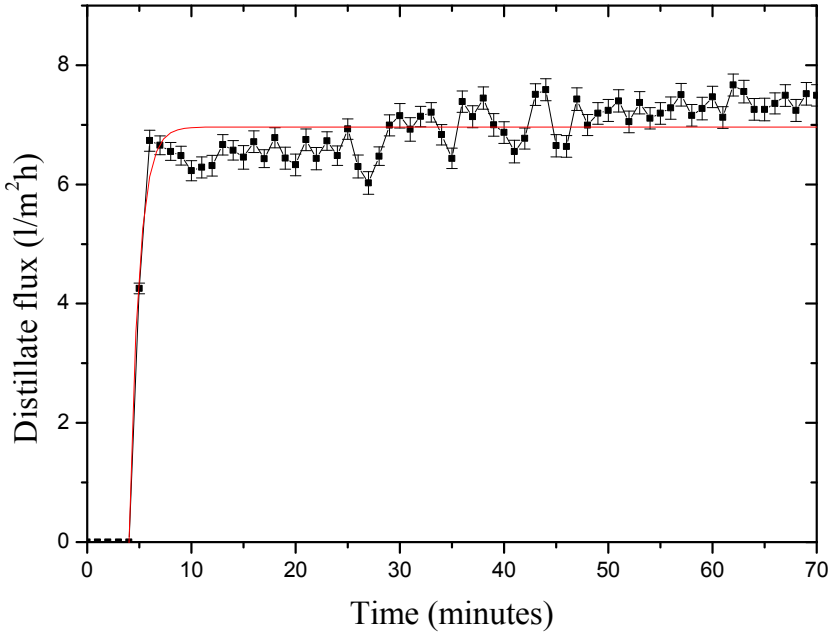

(a) Distillate flux

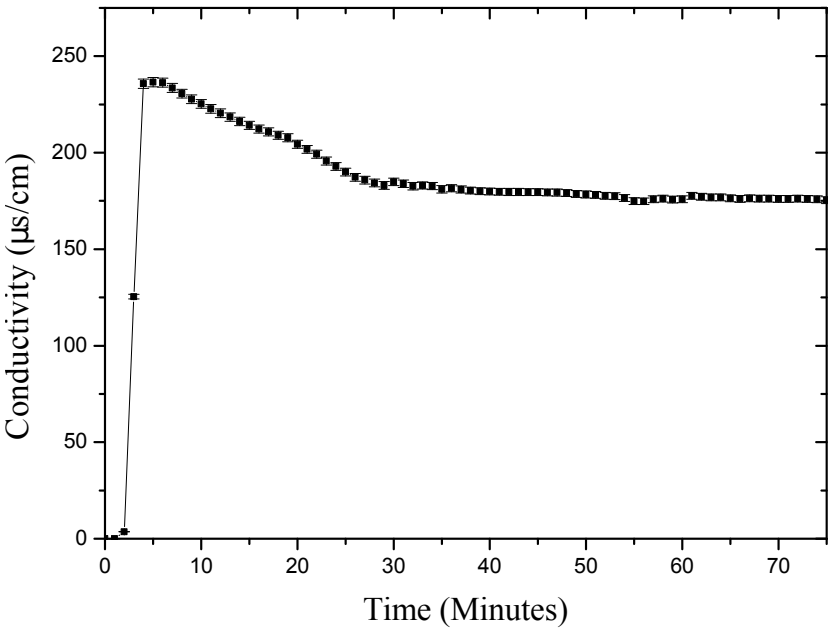

(b) Distillate conductivity

Figure 7.9: Start up data for hot inlet feed temperature 80°C

value was also significantly higher for the G04 membrane. This is attributed to the higher average pore diameter of the G04 membrane, stated to be 0.45 μm by the manufacturer. There will however be a distribution of pore sizes about the average

value and some pores will be significantly larger. Therefore the G04 membrane is more susceptible to membrane wetting and a higher distillate conductivity is expected.

The total change in distillate conductivity and distillate flux for the G02 membrane is shown in table 7.1, for the range of hot inlet feed temperatures from 60 - 80 °C . The table also includes the total change in distillate conductivity and distillate flux for the G04 membrane for a hot inlet feed temperature of 80 °C. This table highlights the relationship between total increase in distillate flux during the start up period and constant operational temperature of the module. Higher hot inlet temperature results in an overall greater increase in the distillate flux. It also leads to a greater decrease in distillate conductivity, suggesting the two are linked. Data presented in chapter 6 demonstrated that higher temperatures yield greater expansion of the pores. Therefore it is proposed that this is the cause of the increase in distillate flux observed and subsequent improvement in distillate quality.

Membrane	Hot inlet temperature °C	Δ conductivity μS/cm	Δ distillate flux l/m^{2}h
G02	60 °C	128.1	0.27
G02	70 °C	133.3	0.5
G02	80 °C	137.2	0.71
G04	80 °C	62.6	0.78

Table 7.1: Change in distillate conductivity and flux observed over an 80 minute period, for G02 and G04 membranes, at a range of temperatures

7.2 Conclusions

In this chapter the distillate output is observed as the module is heated from an ambient temperature, to establish the effect of long-term intermittency, such as an over night shut down period. The distillate flux and conductivity were investigated during the

first 80 minutes of operation under constant input condition, such as feed flow rate and feed temperature. It was observed that the distillate output from an MD module varied during the first hour of operation, approximately, despite constant input parameters. This effect is believed to be the result of an increase in membrane pore size as it is heated. The details of the relationship between membrane temperature and pore size are outlined in chapter 6.

The start up period was investigated for fixed feed temperatures at the inlet channel between 60 and 80°C. In was found that in all cases the temperature in the channels reached a steady value after just 3 minutes, however the distillate output continued to vary. This is thought to be the result of the low heat transfer coefficient of the PTFE membrane material. Although the feed solution quickly reached the desired operating temperature, the membrane itself takes considerably longer to heat up. As a result the increase in membrane pore size occurs gradually. Therefore the distillate flux will also gradually increased over the duration of the experiment.

When the module was operated with a constant temperature of 80°C at the inlet to the hot channel, the average distillate flux in the first 10 minutes of operation was 6.40 l/m^{2}h. After 50 minutes the average distillate flux was 7.11 l/m^{2}h; an increase of 0.71 l/m^{2}h. The increase in distillate volume is an indication of an increase in the size of the membrane pores. The rate of diffusion is dependant on pore size, an increase in pore size leads to greater vapour diffusion which leads to a larger distillate flux. The increase in distillate flux was greater when the feed solution entering the hot channel was maintained at 80°C, when compared to hot inlet temperatures of 60 and 70°C, shown in table 7.1. This is expected, as the increase in pore size is also largest when the membrane was heated to 80°C.

The conductivity of the distillate was observed to decrease over time. The greatest decrease in conductivity was observed when the feed in the hot channel was maintained at 80°C. The conductivity decreased from 140.04 μS/cm to 3.78 μS/cm in the first 30 minutes of operation. This could be due, in part, to scaling of the membrane. Any

salt crystals that may have formed in the membrane pores during cooling periods when the module was shut down would be flushed out during initial operation of the system. However measures where taken in the experimental procedure to avoid this effect; the system was washed out with de-ionised water after every use, before the system was shut down. Therefore it is likely that the increase in distillate flux results in lower conductivity, as more pure water vapour passing through the membrane pores would lead to a dilution of any small amount of saline liquid able to pass through the pores.

When a membrane distillation system is powered by solar energy it is inevitable that it can not operate over night, therefore such long-term intermittency is unavoidable. However, depending on the configuration of the combined solar MD system, the membrane module may also experience short term energy fluctuations. If the MD module is directly coupled with a concentrated solar collector this short term intermittency can be particularly pronounced. Therefore the effects of short term intermittent use on the distillate yield is investigated in the following chapter.

Chapter 8

Effect of solar fluctuations on membrane performance

In this chapter, the effects of short term intermittent use of a Membrane Distillation (MD) module are investigated. The aim is to determine if the module is compatible for coupling with a Concentrated Photovoltaic/Thermal (CPV/T) energy collector. During cloudy weather solar irradiance incident on an energy system can fluctuate. When directly coupled with a CPV/T collector, the MD system will experience a fluctuating energy input. This research aims to assess the performance of the MD unit under fluctuating operating conditions, such as those expected from a CPV/T collector.

The feed flow rate was constant at 0.6 l/min throughout all experiments discussed

in this section. The salt concentration of the feed solution was also kept constant at 35 g/l. A square wave temperature input was chosen to most accurately represent the output from a CPV/T system. The feed solution was heated as it passed through a stainless steel coil, before entering the hot channel of the module and flowing along the membrane. To achieve a square wave temperature input, the stainless steel coil was placed inside a heated water bath and then removed periodically. When the coil was placed inside the bath the feed solution was heated to a desired temperature; this is referred to as an 'on' interval. A temperature range from 60 - 80°C was investigated. When the coil was removed from the bath the temperature of the feed dropped to ambient; this is refereed to as an 'off' interval. The length of the 'off' intervals were varied between 5 - 20 minutes. It is possible for cloud cover to last for longer, but over these lengths of time the behaviour becomes similar to that seen during start up. The distillate flux and conductivity were monitored throughout the feed temperature cycles, allowing the effect of short term intermittency to be explored.

8.1 Solar energy system

The MD module detailed in this thesis paper is intended for use with a solar concentrated photovoltaic and thermal (CPV/T) energy source. A schematic of the proposed CPV/T system is shown in figure 8.1. The construction of this system was beyond the scope of this work. However extensive modelling of the system was carried out, this modelling informed the way in which the system was simulated using the heat bath. The system would consist of a parabolic dish concentrator with 2-axis tracking. Solar radiation that is incident on the aperture of the dish will be reflected and concentrated to a focal point. A combined photovoltaic and thermal receiver is placed at the focal point of the dish to collect the solar radiation. The use of concentrating optics such as a parabolic dish drastically reduces the area of the receiver required, as light is concentrated into a smaller area. Given that the receiver is often the most expensive part of a solar energy system, this can greatly reduce the overall cost [44].

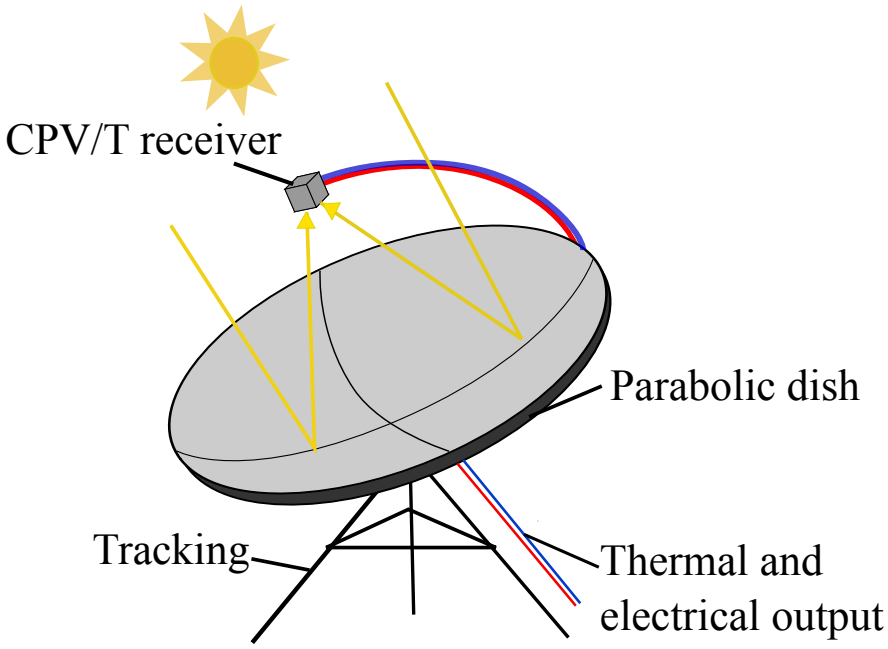

Figure 8.1: Photovoltaic/Thermal receiver with parabolic concentrator

The output from a CPV/T solar collector is both electricity from the PV cells and thermal energy from the heated fluid in the thermal collector. This system is ideal for use with an MD unit for the purification of seawater. The electricity can be used to power the pumps required to push the fluid through the system, while the thermal energy collected can be used to heat the seawater to the desired temperature for desalination, effectively creating a single standalone system that can run autonomously.

8.1.1 Solar energy fluctuations

The amount of solar energy available can fluctuate significantly throughout the day, due to intermittent cloud cover. The total solar energy that reaches the earth's surface is know as global radiation, and is a combination of direct and defuse radiation. Direct radiation is light that falls perpendicular to the earths surface, whereas defuse radiation is light that has been scattered through the earths atmosphere. The proportion of direct and defuse light that make up total global radiation can change drastically depending on the presence of cloud cover [47]. During dense cloudily conditions the light incident

on the earths surface will be entirely defuse, as clouds cause the light to scatter.

When using high concentrating optics such as the parabolic dish, only light falling perpendicular to the aperture of the dish will be concentrated onto the receiver at the focus. Such variations in global radiation composition pose a more significant issue than they do for flat panel systems which also collect diffusion radiation.

Vijayakumar et al [48] investigated short term direct beam radiation during cloudy conditions. The radiation was shown to rapidly reduce to zero for several minute intervals during the day, displaying an on-off behaviour. Figure 8.2 shows direct beam radiation data collected at a test site on campus at Heriot-Watt University on the 11th of August, 2012. This data was collected using a solar tracker ($Solys2$) and pyrheliometer ($CHP1$) from Kipp and Zonen. The conditions on the day were described as intermittent cloud cover. The direct beam irradiance data shows the same 'on' and 'off' behaviour as discussed by Vijayakumar et al [48]. The duration of the fluctuations vary significantly from 1 minute to 20 minutes.

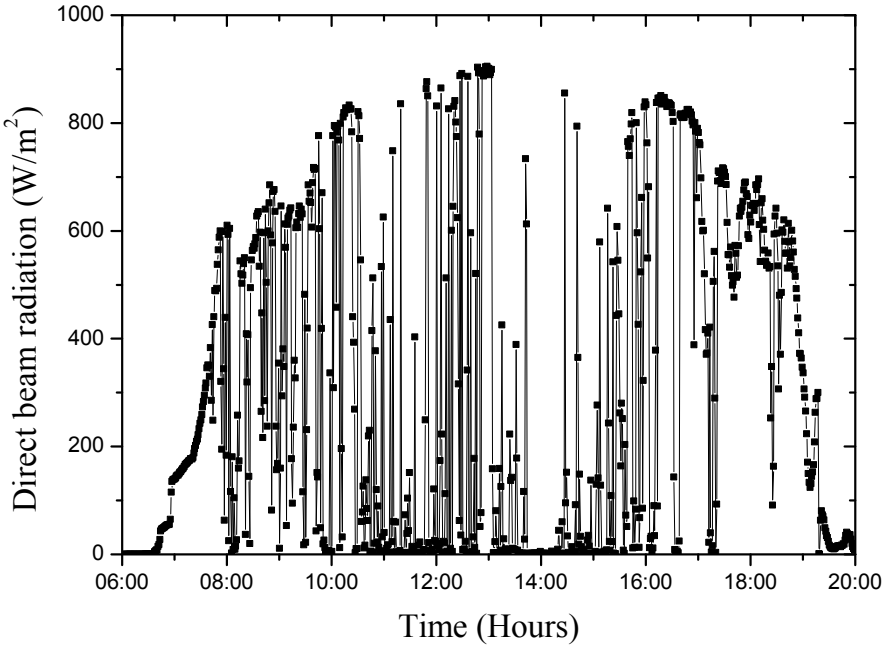

Figure 8.2: Direct beam radiation on 11/08/12, Edinburgh, UK

These energy fluctuations will result in transient operation of the MD unit, when

directly coupled with a CPV/T system. To investigate the effects of such fluctuations in a controlled lab environment, the solar energy input was simulated with the use of a heated water bath. The feed solution flowed through a heat exchanger coil before entering the MD module. This coil was placed inside the heated bath and then removed, periodically. Therefore the temperature of the feed solution entering the module was altered to follow a square wave function, effectively supplying the MD module with an on and off heat supply. The length of the intervals was varied from 5 minutes to 20 minutes, to replicate the behaviour of direct beam radiation.

8.2 Effects of the square wave power input on distillate yield

Before the module was tested with fluctuating energy input, it was first operated for a period of 90 minutes with constant input operating parameters. To do so the heat exchanger coil was left inside the heated bath, and the feed temperature remained constant. This was to ensure that the module was operating under steady-state conditions before the temperature fluctuations began. As demonstrated in Chapter 7, the system can take up to an hour for the distillate output to become stable. All of the experiments in this section were conducted using the G04 membrane.

The MD module was tested with a square wave temperature input period of 40 minutes, with equal heating intervals of 20 minutes on and 20 minutes off. When the heat exchanger coil was placed inside the water bath the feed solution was heated and a constant feed temperature of 80°C was maintained at the entrance to the hot channel of the module. When the coil was removed from the bath, the temperature decreased to ambient, which in this instance was 17 °C. The temperature at the inlet and outlet of the hot and cold channels are presented in figure 8.3.

When the heat exchanger coil was removed from the bath, the temperature of the feed solution dropped rapidly in the first 2 minutes. Therefore the function does not

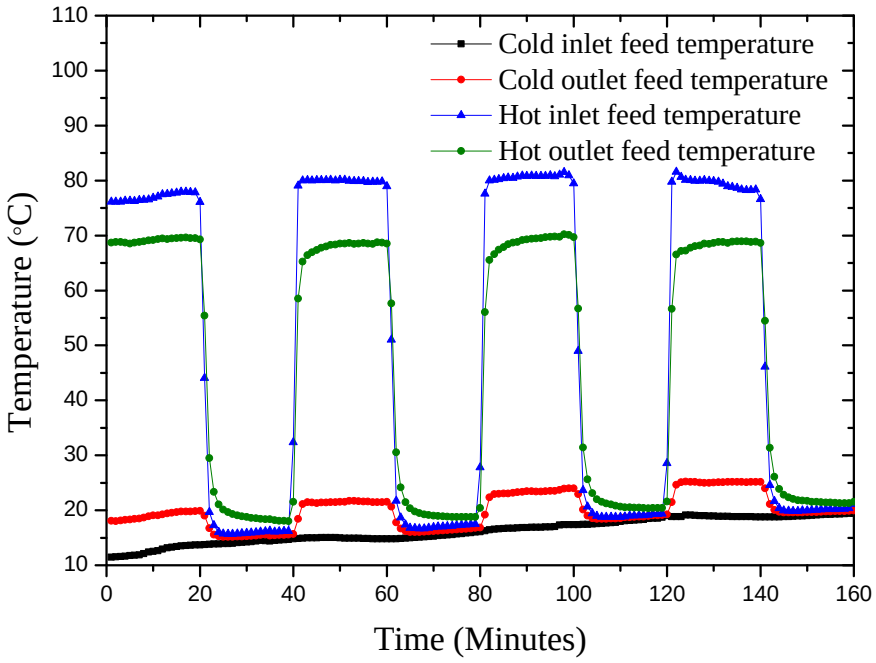

Figure 8.3: Square wave temperature function of the inlet and outlet channels, with the bath set at 80°C for 20 minute intervals

display a perfectly digital on/off behaviour. However, this rapid decrease is similar to the drop in temperature expected from an energy system, as the PV/T receiver would retain residual heat when in operation.

Also, during an 'off' interval the temperature of the feed exiting the hot channel remained slightly higher than the feed entering the channel, suggesting that the feed is heated as it passes through the hot channel. From this we can infer that the module still retained some heat. However by the end of the 20 minute off interval, the temperature of the feed exiting the channel approached the same value as the inlet temperature, suggesting that the MD module was cooled.

The hot inlet feed temperature and distillate output produced from the module can be seen in figure 8.4(a). Vapour pressure difference is the driving force for mass flux across the hydrophobic membrane. The vapour pressure difference is a function of the

temperature difference across the membrane; therefore the distillate output follows the same trend as the feed temperature.

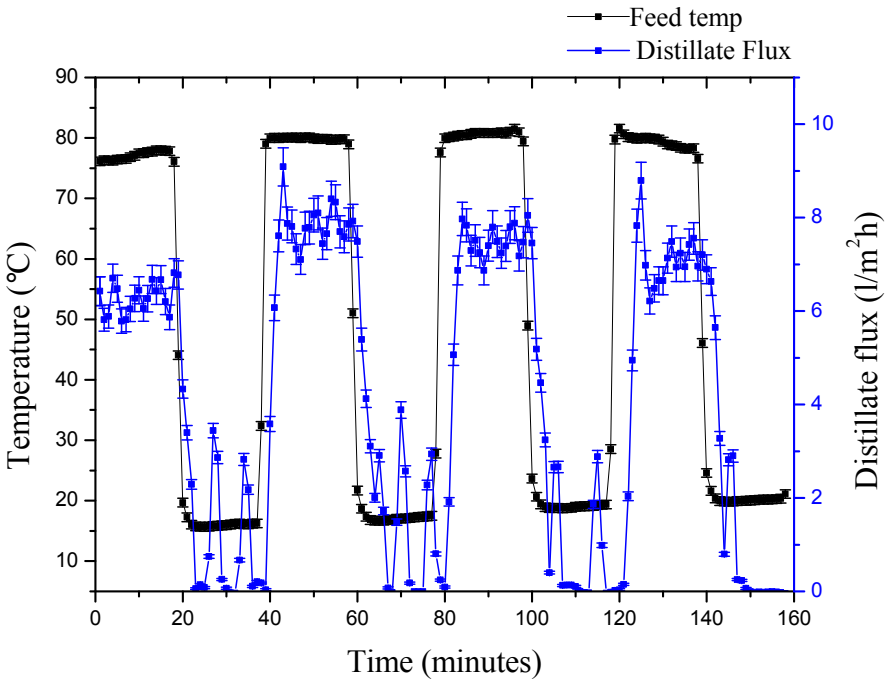

(a) Distillate flux

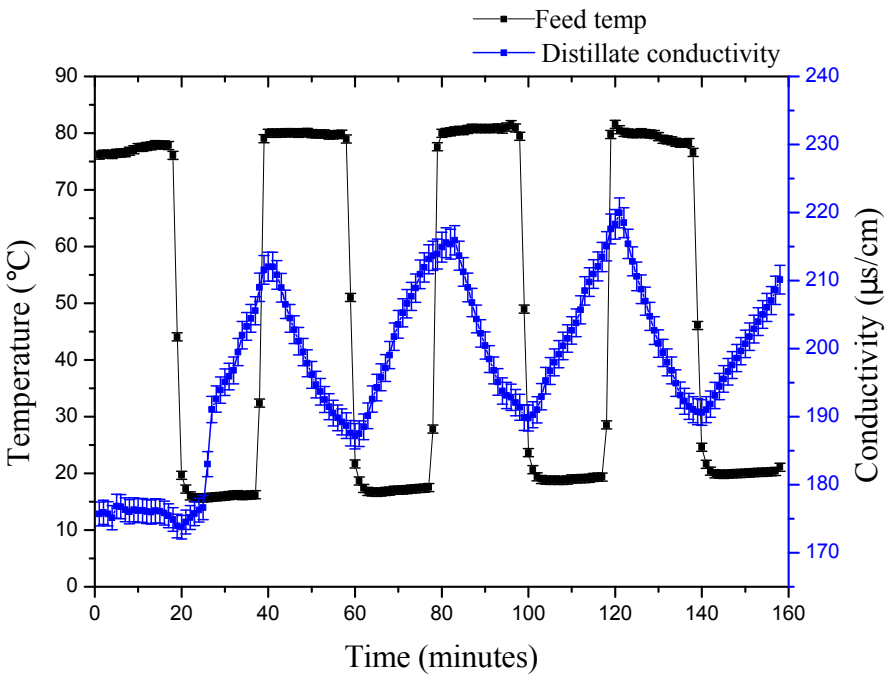

(b) Distillate conductivity

Figure 8.4: Hot inlet seawater temperature 80°C, 20 min intervals

The distillate flux shows a delayed response to the fluctuations in temperature; this delay is thought to be due to the thermal mass of the heat exchanger coil and the MD unit. During an off period the feed returns to ambient temperature over a 2 minute period, however the distillate flux takes an average of 5 minutes to respond and decrease accordingly.

There is a marked improvement in the distillate flux after the first temperature fluctuation, with a peak of 9.1 l/m^2h. This is thought to be due to the improved mixing in the hot feed channel. This would lead to the removal of temperature and concentration polarisation boundary layers, which were established during long periods of continuous operation under constant conditions.

The conductivity of the distillate produced, shown in figure 8.4(b), has a clear correlation with the temperature of the inlet seawater. The conductivity of the distillate increases as the feed temperature decreases. The mean increase in conductivity per cycle was 31.3 $\pm$ 3.1 μS/cm. There is also a gradual increase in conductivity seen per cycle, leading to an overall increase during the course of the experiment.

As discussed in Chapter 4, the conductivity well fitting introduced a delay into the reading. When an instantaneous change was made to the conductivity of the solution flowing into the well, it took 3 minutes for the conductivity probe to respond. The 20 minute time periods involved in these experiments are far in excess of the 3 minute response time of the conductivity sensor due to its fitting. Therefore it can be concluded that the conductivity does gradually increase during an 'off' interval and gradual decrease seen during an on interval. This is perceived to be a function of the membrane and not only the response time of the fitting. Therefore it is concluded, as in the previous chapter, that the change in conductivity is the result of heating and cooling of the membrane material, which alters the structure of the membranes pores.

During an 'off' interval, the average temperature of the feed solution flowing through the hot channel was 20°C and small amount of distillate was still produced. However this distillate had a higher conductivity. It is proposed that during this time any trace

amounts of liquid able to pass through the pores would be more apparent, as very little pure vapour is transiting the pores in order to dilute it.

The distillate produced during an 'off' interval would be cooler than distillate produced when the system is operating with a feed temperature of 80°C. This change in temperature will effect the conductivity probe, as this measurement is temperature dependant. The conductivity probe was calibrated at various temperatures, the data obtained in this process is shown in figure 4.1. For a solution with an initial conductivity of 200 μS/cm at 20°C, there was an average increase of 1.9 μS/cm for every 1°C temperature increase. Therefore given the decrease in distillate temperature a lower conductivity measurement is expected, however the trend clearly shows an increase in conductivity. If a distillate temperature of 20°C during an 'off' interval is assumed, there is an 5°C difference in the distillate produced when compared to an 'on' interval. To correct for this temperature change the conductivity should be 9.5 μS/cm higher than the recorded value, giving an overall true increase of 40.8 μS/cm compared to the 31.3 μS/cm reported earlier.

After running for 90 minutes with constant input conditions until a steady state output was achieved, the experiment was repeated with a square wave input temperature function with heating intervals of 10 minutes 'on' and 10 minutes 'off'. As in the previous experiment, when the heat exchanger coil was placed inside the bath the feed temperature entering the hot channel was maintained at 80°C. The temperatures at the inlet and outlet of both the hot and cold channels were recorded and are shown in figure 8.5.

As before, it took 2 minutes for the temperature of the feed solution entering the hot channel to decrease to ambient. The temperature of the feed exiting the hot channel was again higher than the feed entering it, suggesting the membrane and module were still hot. However the temperature difference between the feed entering the hot channel and the feed exiting it remained greater the 'off' interval. This is to be expected as the membrane and module would not be cooled to the same extent during the shortened

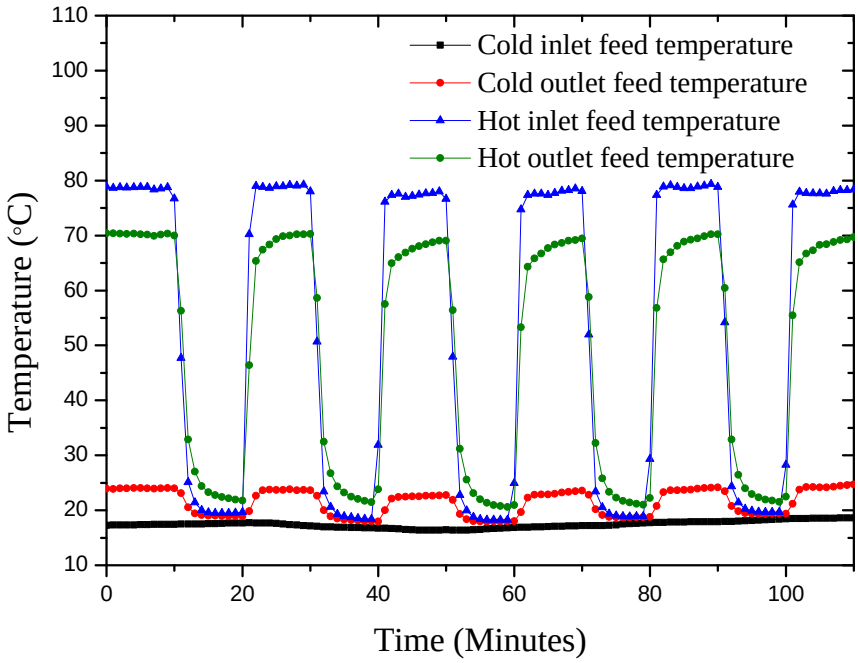

Figure 8.5: Square wave temperature function of the inlet and outlet channels, when the bath was set at 80°C for 10 minute interval

'off' interval.

The distillate flux and conductivity results are presented in figure 8.6. A delayed response between the decrease in feed temperature and decrease in distillate flux is seen in figure 8.6(a); this is again attributed to the thermal mass of the MD module.

The conductivity of the distillate increased while the feed solution flowing through the module was at an ambient temperature. The mean increase in conductivity during a 10 minute 'off' interval was 11.9±2.4 μs/cm. This is lower than the mean increase observed in the previous results, suggesting that the shorter 'off' interval was not sufficient time to cool the membrane and alter its microstructure to the same extent as during the 20 minute 'off' intervals.

During an 'on' interval the conductivity does not return to its former value, suggesting that the membrane has not returned to its previous temperature, and that

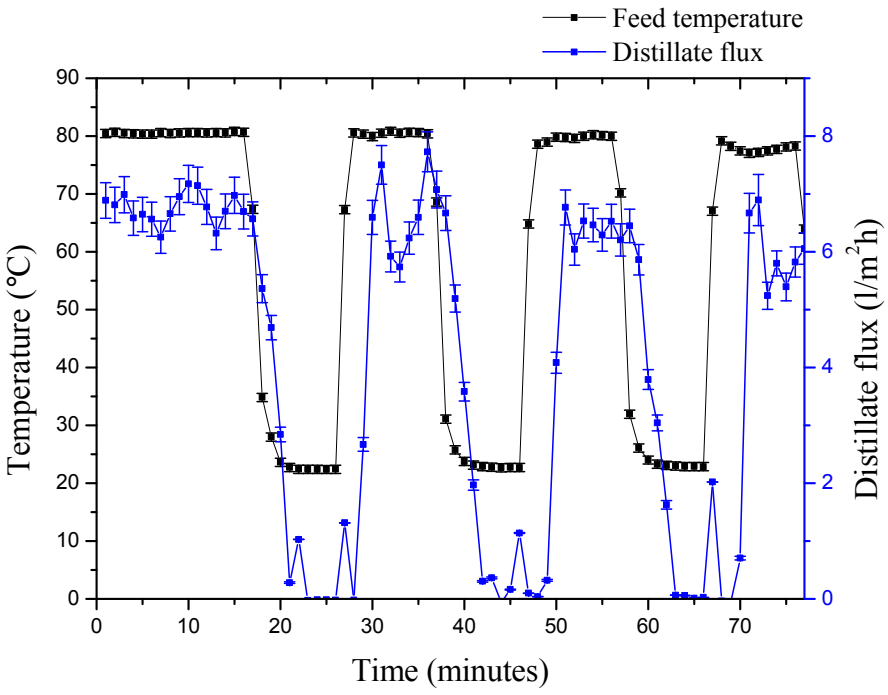

(a) Distillate flux

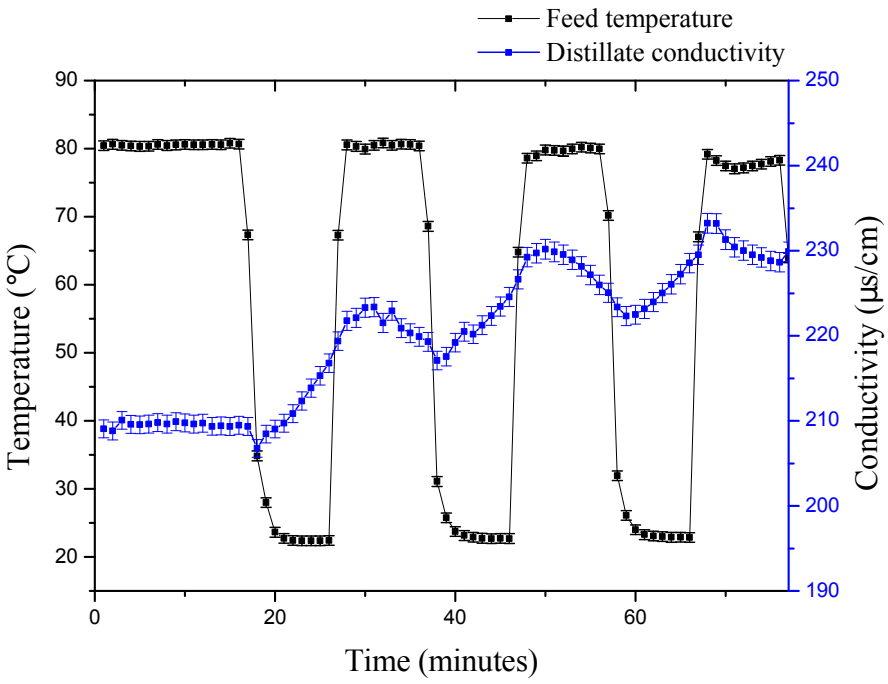

(b) Distillate conductivity

Figure 8.6: Hot inlet seawater temperature 80°C, 10 min intervals

the pores have not expanded to their previous size. The mean decrease in conductivity as result of an 'on' interval was 7.1 ± 0.89 μS/cm. This resulted in a gradual increase in conductivity over the course of several feed temperature cycles. This effect is more pronounce than in the previous data set with 20 minute intervals, as shown in figure 8.4.

A square wave temperature input function with 'on' and 'off' intervals of 5 minutes was also tested. The temperatures at inlet and outlet of each channel are shown in figure 8.7.

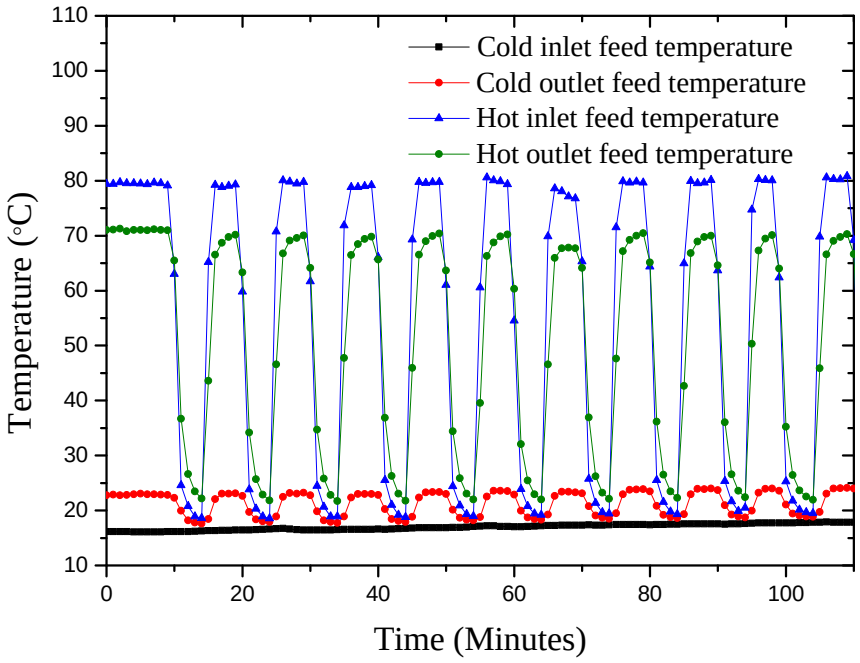

Figure 8.7: Square wave temperature function of the inlet and outlet channels, with 5 minute interval when the bath was set at 80°C

Figure 8.8 shows the distillate flux and distillate conductivity for 5 minute intervals. Figure 8.8(a) clearly shows the same time delay between the decrease in feed temperature and decrease in distillate flux is on average 5 minutes, as the two curves are out of phase with each other.

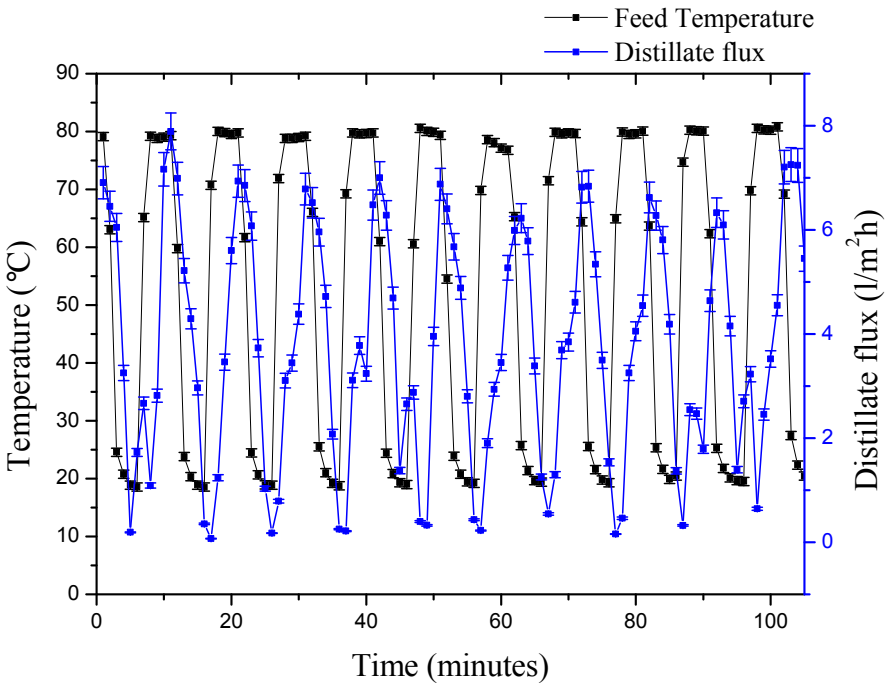

(a) Distillate flux

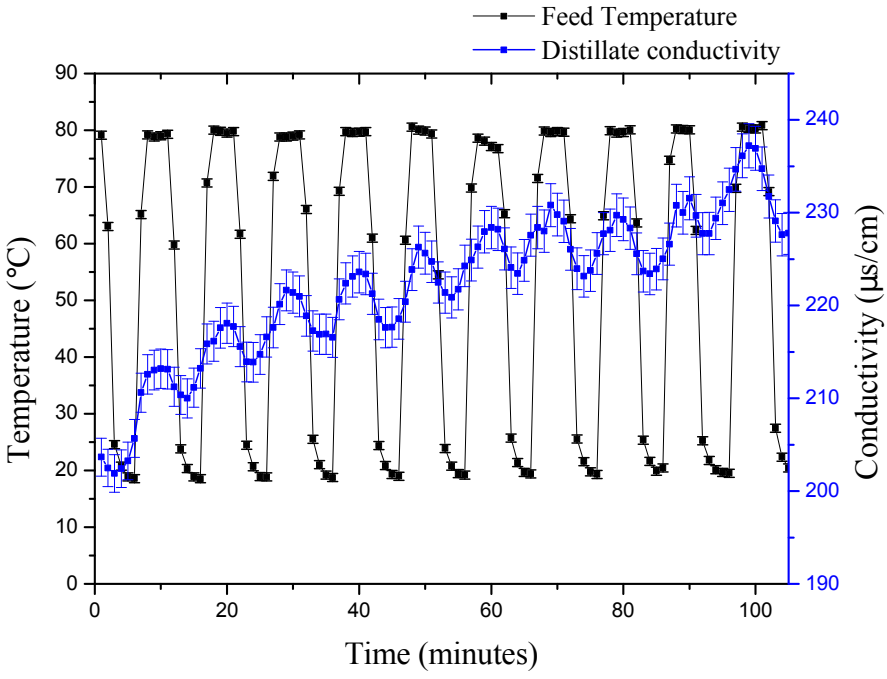

(b) Distillate conductivity

Figure 8.8: Hot inlet seawater temperature 80°C, 5 minute intervals

The mean increase in conductivity during a 5 minute 'off' interval was 7.8 ± 0.8 μS/cm; again this is less than the mean amplitudes seen in the previous results for twenty minute and ten minute interval fluctuations.

As in the previous two data sets for 20 and 10 minute intervals, a gradual increase in conductivity is observed over the course of several repeated cycles, leading to an overall increase over the 80 minute experiment. However it is important to note that this increase is significantly more apparent for the 5 minute intervals, than for the previous data sets. The mean decrease in conductivity is only 5.6 ± 0.7 μS/cm, which is significantly less than the mean 7.8 ± 0.8 μS/cm increase seen. It can be concluded that the membrane is not sufficiently heated during the 5 minute 'on' interval, for the distillate conductivity to decrease to its former value. This led to the conductivity rising gradually by 32.3 μS/cm during the 110 minute experiment.

From this it can be concluded that although a single 5 minute interval does not significantly affect the quality of the distillate, several consecutive 5 minutes temperature fluctuations, as would be typically seen on a cloudy summer day, can have a marked effect.

A similar square wave temperature input was tested for 20 minute intervals, but with a feed temperature at the inlet of the hot channel maintained at 60°C rather 80°C during an 'on' interval. The temperatures at the inlet and outlet of the channels are shown in figure 8.9.

The resulting distillate flux and distillate conductivity are presented in figure 8.10. The lower feed temperature yielded a lower distillate flux, of between 3 l/m^{2}h and 4 l/m^{2}h. A clear link between feed temperature and distillate conductivity is shown. The lower amplitude of the temperature fluctuation, from ambient to 60°C, has also given rise to smaller fluctuations in the distillate conductivity with a mean increase of 10.7 ± 0.9 μS/cm per cycle. This is considerably lower than was seen for a higher temperature of 80°C, and otherwise identical input parameters (figure 8.4(b)).

The square wave temperature input was again tested with 10 minute intervals and

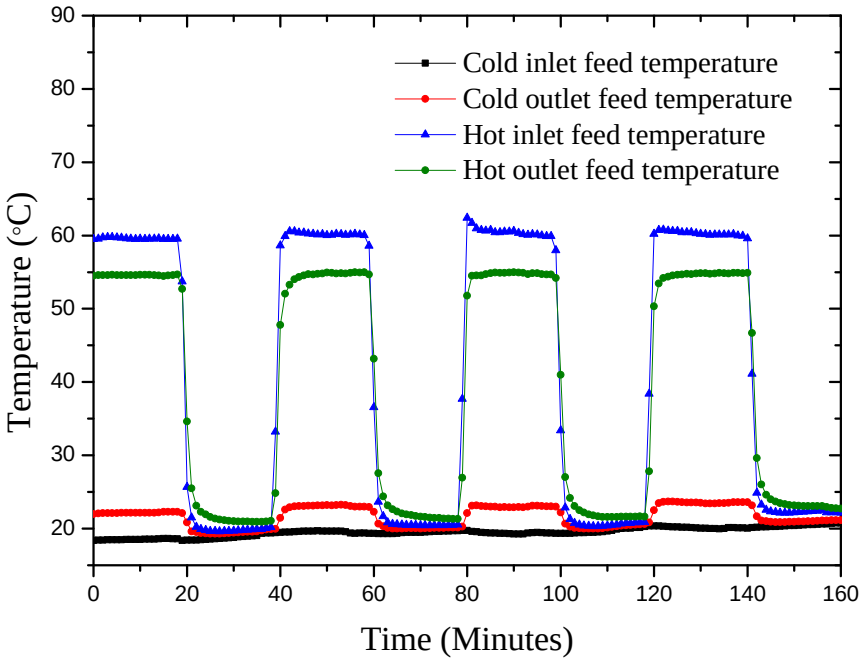

Figure 8.9: Square wave temperature function of the inlet and outlet channels, when the bath was set at 60°C for 20 minute intervals

a feed temperature at the hot channel inlet of 60°C during an 'on' interval. The results are shown in figure 8.11.

The distillate flux and conductivity are shown in figure 8.12. A lower distillate flux was measured than in the previous cases with an inlet feed temperature of 80°C. The mean distillate flux during an 'on' interval was 3.14 l/m^{2}h. This value is less than in the previous results with 20 minute intervals.

Figure 8.12(b) shows the conductivity trend, during the temperature cycles. An increase in conductivity during an 'off' period was observed, the mean increase was 4.24 $\pm$ 1.1 μS/cm per cycle.

In all of the results presented the conductivity of distillate increased when the heat exchanger coil was removed from the water and the feed solution cooled to ambient temperature. The conductivity of the distillate consistently decreased again when the

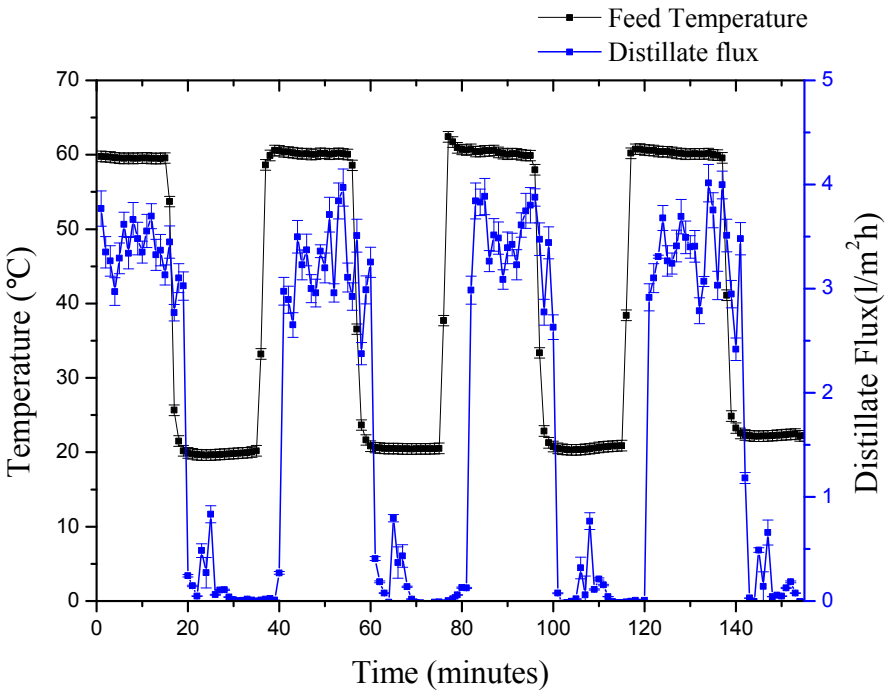

(a) Distillate flux

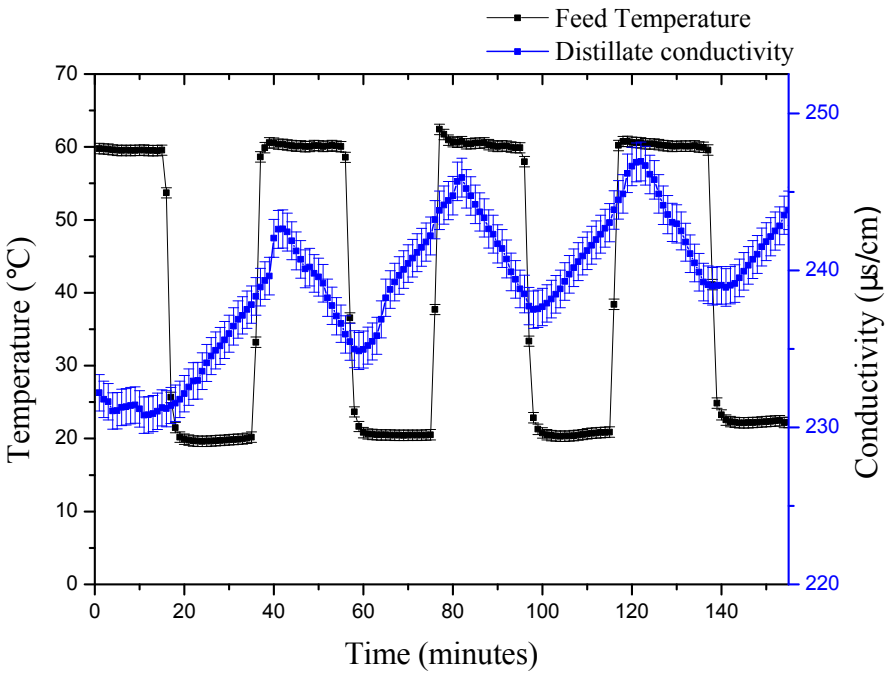

(b) Distillate conductivity

Figure 8.10: Hot inlet seawater temperature 60°C, 20 minute intervals

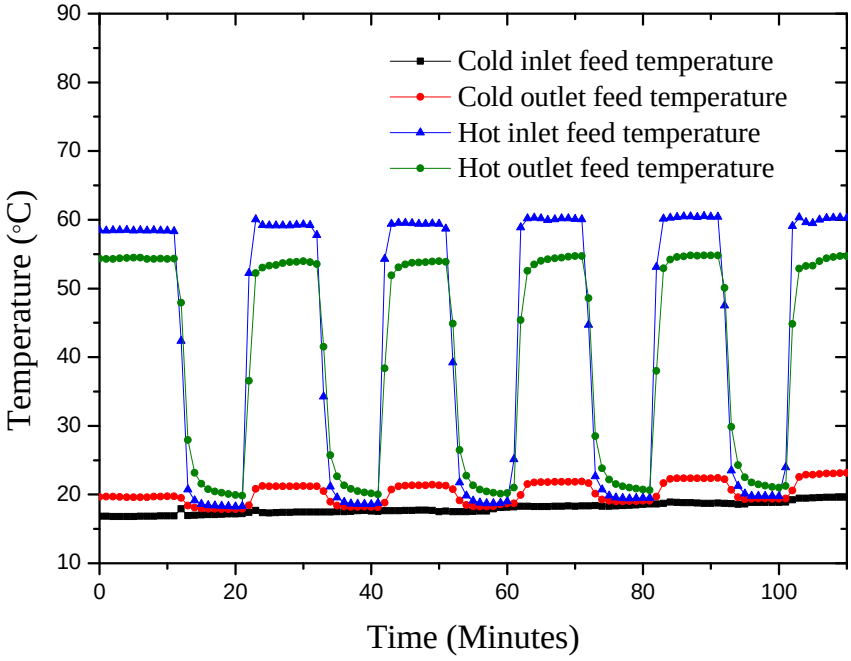

Figure 8.11: Square wave temperature function of the inlet and outlet channels, when the bath was set at 60°C for 10 minute intervals

coil was returned to the heat bath. Figure 8.13 shows the mean increase seen in the conductivity of the distillate during an 'off' interval against the duration of the off interval. In order to establish the mean increase, the difference between the highest and lowest value was calculated for each individual peak and an average was taken.

The increase in conductivity clearly relates to the length of time that the heat source was removed. A greater increase in the distillate conductivity was recorded during longer 'off' intervals. A higher feed temperature during 'on' intervals also leads to a greater increase in conductivity during an 'off' interval. When the feed solution was initially at 60°C and the heat exchanger coil was removed for 20 minutes, a mean increase 10.7 ± 0.9 μS/cm was observed. However when the feed was at 80°C before the heat was removed for the same period of time, the mean increase in conductivity was 31.3 ± 3.1 μS/cm.

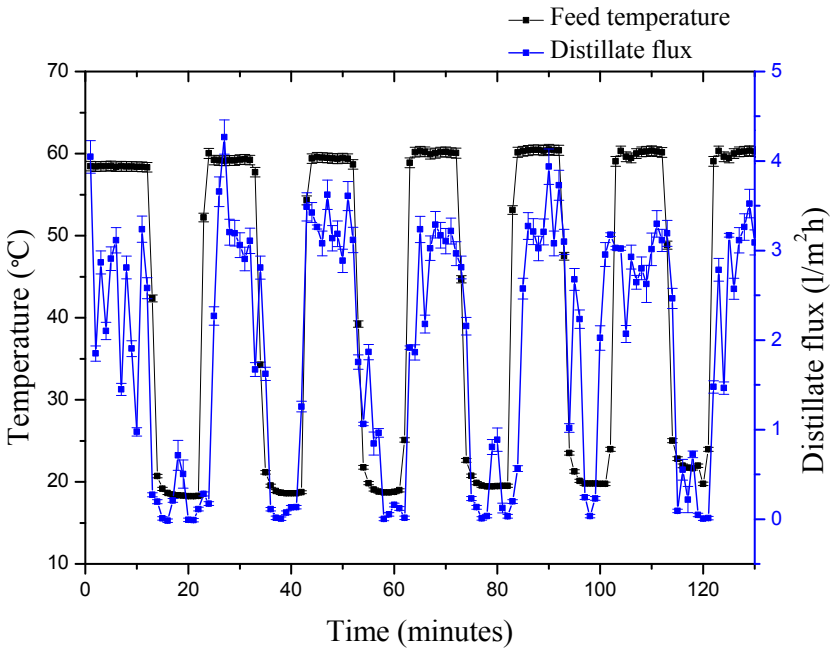

(a) Distillate flux

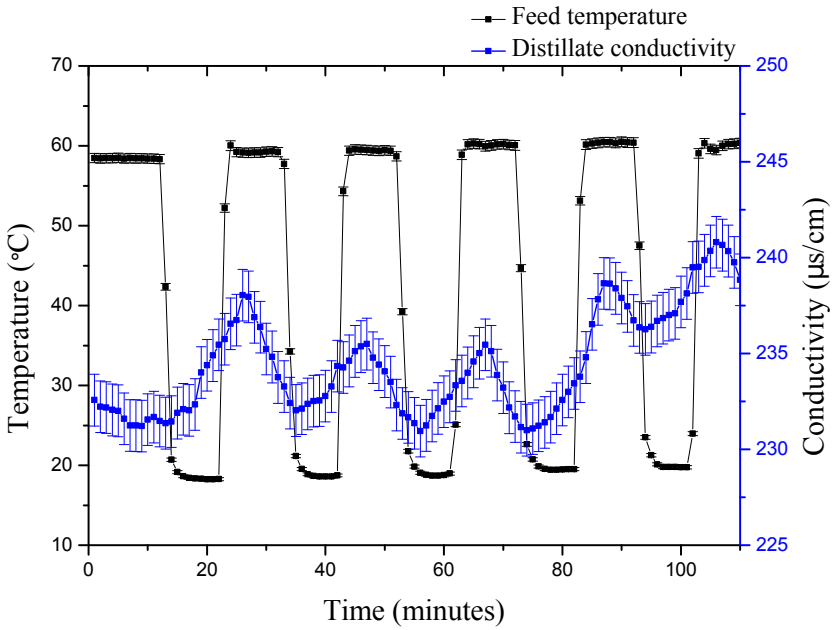

(b) Distillate conductivity

Figure 8.12: Hot inlet seawater temperature 60°C, 10 minute intervals

This effect is thought to be the result of thermal expansion and contraction of the membrane material when it is heated and cooled causing a change in the microstructure of the membrane pores. It was demonstrated that heating the membrane can cause the

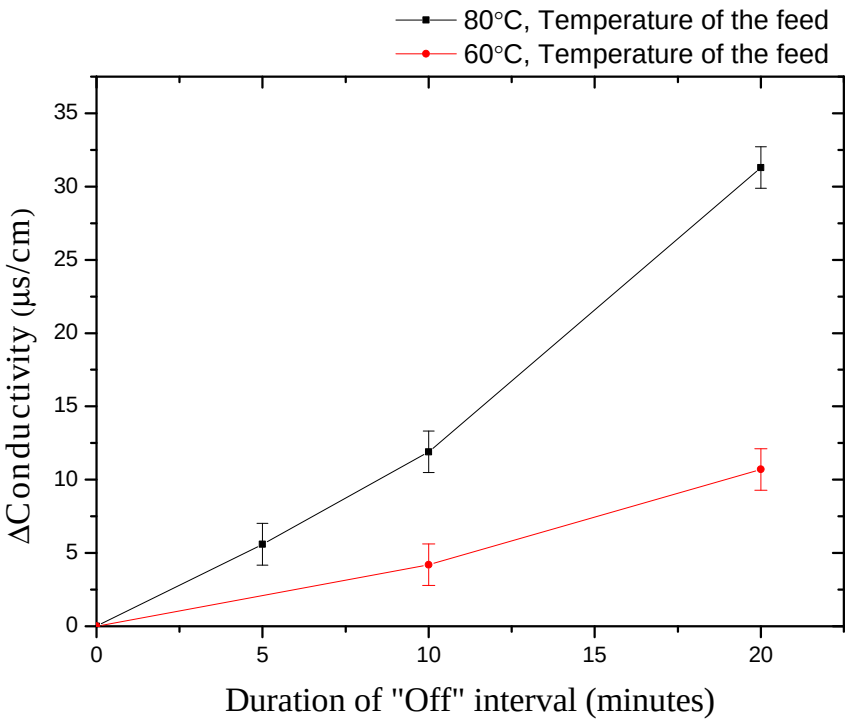

Figure 8.13: Increase in conductivity against the duration of time that the heat source was removed

pore size to increase which will lower the liquid entry pressure (LEP) of the membrane. The increase in the pore size leads to greater vapour diffusion across the membrane, therefore a larger distillate flux. This also affects the quality of the distillate produced. The results in Chapter 6 show that the rate of increase in the pores was greater as well as the overall increase in pore expansion was larger for higher temperatures, shown in figure 6.19.

8.3 Conclusions

Distillate yield and quality are presented for a membrane distillation module operated with simulated feed temperature fluctuations, similar to those expected from a concentrated photovoltaic and thermal energy supply. Solar energy is known to fluctuate largely throughout the day. The fluctuations are particularly pronounced

when using high concentrating optics such as a parabolic dish, as the dish only concentrates direct solar radiation. The inlet feed temperature was varied to cycle as a square wave function with a period of 10, 20 and 40 minutes.

The distillate flux decreased as the feed temperature decreased. However, in all cases a time delay was observed between the decrease in feed temperature and decrease in the distillate flux. This delay was on average 5 minutes and is attributed to the thermal mass of the membrane module.

The distillate conductivity also showed a clear correlation with the feed temperature; as the feed temperature decreased the distillate conductivity increased. The average increase in conductivity during a 20 minute 'off' interval was 31.3 ± 3.1 μS/cm when the feed was maintained at 80°C during an 'on' interval. Whereas the average increase during a 5 minute interval was 7.8 ± 0.8 μS/cm for the same temperature.

In all the results presented a gradual increase in conductivity was observed over the course of several temperature cycles, leading to an overall increase across the duration of the experiment. However this effect was particularly pronounced for the shorter 5 minute intervals. It is concluded that the 5 minute'on' intervals did not provide sufficient time to reheat the membrane and reduce the conductivity to its former value. As a result the conductivity of the distillate increased gradually over the course of several 5 minute cycles. Therefore it was concluded that, although the effect of a single 5 minute interval was not significant, the cumulative effects of several consecutive 5 minute intervals could be.

The increase in conductivity during an off interval was also dependant on the temperature of the feed while the coil was placed inside the heat bath during an 'on' interval. When the feed, and therefore the membrane, was heated to 80°C, the mean increase in conductivity was 31.3 ± 3.1 μS/cm. However when the feed was heated to 60°C, the mean increase in conductivity was only 10.7 ± 0.9 μS/cm. It is suggested that this effect is the result of heating and cooling the module and the subsequent changes in the size of the pores, as the pore size would contract less when cooled from

60°C than when cooled from 80°C.

Chapter 9

Conclusions

The aim of this work is to investigate the effect of temperature on the structure of PTFE membranes used in Membrane Distillation (MD), and therefore determine the influence of intermittent use of the module. The objective was to establish if an MD system was suitable for direct coupling with a solar energy collector, a Concentrated Photovoltaic and Thermal (CPV/T) energy system in particular. Compact remote solar powered MD plants only operate during sunlight hours, the over-night shut down is refereed to as long term intermittency. When directly coupled with a CPV/T energy collector the MD module would experience a fluctuating temperature input due to the 'on/off' nature of direct solar irradiance; this is referred to as short term intermittency. Therefore the effect of both long term and short term intermittent use of an MD module

were investigated.

A lab scale MD module was designed and manufactured. A series of experiments were conducted to establish the steady state operation of the module. A membrane, known as G02, with average pore size of 0.2 μm was tested. The concentration of NaCl remained constant throughout all experiments, at 35 g/l, while the feed flow rate and temperature were varied. Distillate flux increased with increase in feed flow rate and feed temperature. However it was determined that the distillate flux has an exponential relationship with feed temperature, while the distillate flux shows a linear trend with increase in feed flow rate. The maximum distillate flux recorded was 8.5 l/m^{2}h; this was the output from the module when the feed temperature was 80 °C and the feed flow rate was 1.0 l/min. These result were validated with the use of a 1 dimensional mathematical model.

A comparison was made between the steady state operation of two PTFE membranes manufactured by Gore^{TM}, G02 and G04. The G04 membrane has an average pore size of 0.45 μm. It was found that the G04 membranes produced a higher distillate flux than G02 under the same operating conditions. This was attributed to improved mass transfer through the larger pores. However the G04 membrane produced distillate with a higher conductivity. When both membranes were tested with a feed flow rate of 0.6 l/min and feed temperature at the inlet to the hot channel of 80°C, the G02 and G04 membrane produced distillate with a conductivity value of 3.39 μS/cm and 175.35 μS/cm respectively. This is expected as the larger pores in the G04 membrane have a lower liquid entry pressure, and therefore membrane wetting is more likely to occur.

After establishing the steady state operation of the module, experiments were conducted to determine the effects of intermittent use. A study of the effects on temperature on the structure of the membrane was carried out with the use of a Scanning Electron Microscope (SEM). A sample of the G02 PTFE hydrophobic membrane was imaged at room temperature. The image was analysed, the porosity

was determined to be 84% and the modal pore size to be 0.3 μm. Samples were then heated inside of the SEM chamber with the use of a Peltier stage and images were taken over an 80 minute period. The images show that the membrane pore size increased over time owing to expansion of the PTFE material. When heated from 17°C to 80°C over a 60 minute period the size of a pore increased by 43.9%, from 3.729 μm to 5.367 μm. This is a significant increase, therefore it can be concluded that the dependance of pore size on temperature will impact the performance of the membrane as it is heated and cooled.

An increase in pore size will allow for a greater diffusion of vapour across the membrane, resulting in a higher distillate yield. However this can also increase the likelihood of saline liquid entering the pores and crossing over into the distillate stream. This would result in an increase in the distillate conductivity. Therefore an optimum pore size can be determined, one that maximises distillate flux while ensuring conductivity remains within safe limits, even during intermittent use. Therefore it is concluded that when determining the membrane properties the average pore size and pore size distribution when the material is heated to 80°C should be considered, as the results of these investigations show that these properties can vary substantially with temperature.

When a membrane is heated and cooled during intermittent use, the pore size will change and this effect will be apparent in the flux and conductivity of the distillate. To establish the extend of this effect the module was tested with both long term and short term intermittent use.

When investigating the effect of long term intermittency, the system was switched off overnight. The next day it was started up, while all input parameters such as feed temperature and feed flow rate were kept constant over the course of each experiment. The distillate flux and conductivity produced from the module were observed during the first 1.5 hours of operation. The experiment was repeated several times with different feed temperatures, ranging from 60 - 80°C. When the module was operated with a

constant temperature of 80°C at the inlet to the hot channel, the average distillate flux in the first 10 minutes of operation was 6.40 l/m^2h. After 50 minutes the average distillate flux has increased to 7.11 l/m^2h; an increase of 0.71 l/m^2h. The conductivity of the distillate was observed to decrease over time. The greatest decrease was observed when the feed in the hot channel was maintained at 80°C, giving rise to a fall in conductivity from 140.04 μS/cm to 3.78 μS/cm in the first 30 minutes of operation. It is concluded that as the module is heated the membrane pores expand, causing a greater diffusion of pure water vapour through the pores and therefore more distillate is produced. However this expansion in pore size is not so great as to increase the occurrence of membrane wetting; thus, overall, the distillate quality improves.

The energy input from CPV/T system is expected to have 'on/off' characteristics. Therefore if the module were to be directly coupled with a CPV/T collector, it would experience short term periods of heating and cooling; these periods are expected to be between 5 and 20 minutes. To test the effect of short term intermittent use such fluctuations in feed temperature were simulated with the use of a heated water bath. The G04 membrane was used through the duration of these experiments. The average increase in conductivity during a 20 minute 'off' interval was 31.3 $\pm$ 3.1 μS/cm when the feed was maintained at 80°C during an 'on' interval - whereas the average increase during a 5 minute interval was 7.8 $\pm$ 0.8 μS/cm for the same temperature.

It was observed throughout this series of experiments that the process of heating the membrane during an 'on' interval is slower than cooling it down during an 'off' interval. As a result, the distillate conductivity takes longer to return to its previous value when the heat source was reapplied. This effect was particularly evident during the the shorter 5 minute 'on' intervals, as they did not provide sufficient time to reheat the membrane and reduce the conductivity to its former value. As a result the conductivity of the distillate increased gradually over the course of several 5 minute cycles. Therefore it was concluded that although the effect of a single 5 minute interval was not significant, the cumulative effects of several consecutive 5 minute intervals could result in a salt

content within the distillate that is above the taste threshold for drinking water, or even above safe limits for consumption. Given the rapidly fluctuating nature of direct solar radiation such short term intermittency is expected and therefore this effect would be significant for a CPV/T powered MD system.

In summary, this research has established the link between temperature dependent pore size and the changes in distillate flux and conductivity observed when the membrane is heated and cooled during intermittent operation of a module. The performance of the MD system was analysed over a comprehensive range of intermittent conditions in order to assess its suitability for use with a CPV/T solar power source. These results demonstrate that allowing the membrane to cool significantly has a negative effect on the quality of the distillate yield. This effect is particularly pronounced when the membrane is heated and cooled in rapid cycles, as would be the case if a CPV/T power source were used in cloudy conditions.

9.1 Further work

The current research focused on the intermittent use of an MD module, tested with a simulated input from a solar energy system. A study into the effects of temperature on the PTFE membrane material was carried out, the effects of temperature on the membrane pore size were observed. To further this work it is suggested that an in-depth investigation into the transition through the solid to solid transition phases at 19.2°C and 34.5°C be conducted. The membranes could be imaged while on the heating stage inside of the SEM, at intervals of 1 minute.

In the current study, thermal expansion of the membrane pore and a lumped sum heat transfer model were used to infer the temperature of the membrane while inside the SEM chamber. To build upon this work, it is suggested that the SEM experimental setup could be adapted to include a thermocouple, placed into the chamber and attache to the membrane surface. This could be used to take experimental temperature measurements of the top surface of the membrane over time, to determine the rate

at which it heats up. This data would then be compared to the theoretical results from the lumped sum heat transfer model, with the aim of validating the model.

The analysis conducted in the course of this research focused on the relationship between temperature and membrane pore size. However thermal expansion of the PTFE material will also effect membrane characteristics such as thickness and tortuosity (a measure of the pores curvature along the thickness of the membrane), which also effect the membrane performance. The current SEM set-up could be used to measure changes in thickness as the membrane heats, the orientation of the sample would simply be changed. However to understand the change in pore tortuosity as the membrane heats it would require an insight into the 3D structure of the membrane. It is suggested that this could be achieved with the use of Atomic Force Microscopy, AFM. AFM could be used to produce a 3D map of the membrane topography.

The temperature dependance of these membrane characteristics will effect the performance of a system when operated intermittently. To further the understanding of solar powered MD units, it is suggested that a CPV/T system be developed and built. It could then be coupled with the MD unit to build a pilot plant which could be used for outdoor characterisation under a variety of weather conditions.

Various system configurations could then be tested, to determine the ideal set up. A comparison could be made between a single loop configuration were saline feed solution flows through the solar collector and a two loop configuration were the solar collector and MD module are connected by a heat exchanger. Various controls could then be implemented to determine the operational parameters that will maximise the production of the distillate whilst ensuring that it remains within safe limits for drinking water consumption.

Bibliography

[1] World health organisation and UNICEF. Progress on sanitation and drinking water: 2014 update. *United Nations, New York*, page p12, 2014. ⟨⟨ Cited on pages 2, 7. ⟩⟩

[2] United Nations. The millennium development goals report 2013, technical report. ⟨⟨ Cited on page 2. ⟩⟩

[3] Central Gorund Water Board. Ground water quality in shallow aquifers of india. *Technical report, Government of India*, 2010. ⟨⟨ Cited on page 2. ⟩⟩

[4] Bureau of Indian Standards. Drinking water- specification. (second revision IS0 10500), 2012. ⟨⟨ Cited on page 2. ⟩⟩

[5] D. Chakraborti, S. C. Mukherjee, S. Pati, M. K. Sengupta, M. M. Rahman, U. K. Chowdhury, D. Lodh, C. R. Chanda, A. K. Chakraborti, and G. K. Basu. Arsenic groundwater contamination in middle ganga plain, bihar, india: a future danger? *Environmental Health Perspectives*, 111(9):1194, 2003. ⟨⟨ Cited on page 2. ⟩⟩

[6] B. Peñate and L. García-Rodríguez. Current trends and future prospects in the design of seawater reverse osmosis desalination technology. *Desalination*, 284(0):1 – 8, 2012. ⟨⟨ Cited on page 3. ⟩⟩

[7] L. Garcia-Rodriguez. Seawater desalination driven by renewable energies: a review. *Desalination*, 143(2):103 – 113, 2002. ⟨⟨ Cited on page 3. ⟩⟩

[8] M.S. El-Bourawi, Z. Ding, R. Ma, and M. Khayet. A framework for better understanding membrane distillation separation process. *Journal of Membrane Science*, 285(1–2):4 – 29, 2006. ⟨⟨ Cited on pages 3, 9, 10, 11, 14, 68. ⟩⟩

[9] K. W. Lawson and D. R. Lloyd. Membrane distillation. *Journal of Membrane Science*, 124(1):1 – 25, 1997. ⟨⟨ Cited on pages 3, 9, 13, 16, 68, 70, 74, 77, 109, 125, 127, 129. ⟩⟩

[10] D. W. Gore. Gore-tex membrane distillation. *Proceeding of the tenth annual convention of the water supply improvement association*, Honolulu, USA, 1982. ⟨⟨ Cited on page 3. ⟩⟩

[11] D. Winter, J. Koschikowski, and M. Wieghaus. Desalination using membrane distillation: Experimental studies on full scale spiral wound modules. *Journal of Membrane Science*, 375(1–2):104 – 112, 2011. ⟨⟨ Cited on pages 3, 4, 10, 12, 13, 31, 69, 72, 128, 133. ⟩⟩

[12] R. Schwantes, A. Cipollina, F. Gross, J. Koschikowski, D. Pfeifle, M. Rolletschek, and V. Subiela. Membrane distillation: Solar and waste heat driven demonstration plants for desalination. *Desalination*, 323(0):93 – 106, 2013. Membrane Distillation and related Membrane Systems. ⟨⟨ Cited on pages 3, 31. ⟩⟩

[13] F. Banat, N. Jwaied, M. Rommel, J. Koschikowski, and M. Wieghaus. Performance evaluation of the "large smades" autonomous desalination solar-driven membrane distillation plant in aqaba, jordan. *Desalination*, 217(1–3):17 – 28, 2007. ⟨⟨ Cited on pages 4, 32. ⟩⟩

[14] F. Banat, N. Jwaied, M. Rommel, J. Koschikowski, and M. Wieghaus. Desalination by a "compact smades" autonomous solarpowered membrane distillation unit. *Desalination*, 217(1–3):29 – 37, 2007. ⟨⟨ Cited on pages 4, 29, 32. ⟩⟩

[15] A. Cipollina, G. Micale, and L. Rizzuti. Seawater desalination: Conventional and renewable energy processes, green energy and technology. *Springer-Verlag Berlin Heidelberg*, 2009. ⟨⟨ Cited on page 6. ⟩⟩

[16] Department of Economic and Social Affairs. The millennium development goals report. *United Nations, New York*, (p40), 2008. ⟨⟨ Cited on page 7. ⟩⟩

[17] R. Borsani and S. Rebagliati. Fundamentals and costing of {MSF} desalination plants and comparison with other technologies. *Desalination*, 182(1–3):29 – 37, 2005. Desalination and the Environment Desalination and the Environment. ⟨⟨ Cited on page 8. ⟩⟩

[18] G. Micale, A. Cipollina, and L. Rizzuti. Seawater desalination: Conventional and renewable energy processes. *Green Energy and Technology, Springer Berlin Heidelberg*, pp 1-15, 2009,. ⟨⟨ Cited on pages 10, 27, 28. ⟩⟩

[19] P.A. Hogan, Sudjito, A.G. Fane, and G.L. Morrison. Desalination by solar heated membrane distillation. *Desalination*, 81(1–3):81 – 90, 1991. Proceedings of the Twelfth International Symposium on Desalination and Water Re-use. ⟨⟨ Cited on pages 10, 27, 28. ⟩⟩

[20] J. Zhang, N. Dow, M. Duke, E. Ostarcevic, J. Li, and S. Gray. Identification of material and physical features of membrane distillation membranes for high performance desalination. *Journal of Membrane Science*, 349(1–2):295 – 303, 2010. ⟨⟨ Cited on page 10. ⟩⟩

[21] J. G. Knudsen and D. L. Katz. Fluid dynamics and heat transfer. *McGraw-Hill, New York*, 1980. ⟨⟨ Cited on pages 11, 83. ⟩⟩

[22] A. Cipollina, M.G. Di Sparti, A. Tamburini, and G. Micale. Development of a membrane distillation module for solar energy seawater desalination. *Chemical Engineering Research and Design*, 90(12):2101 – 2121, 2012. ⟨⟨ Cited on pages 11, 69, 71, 73, 76, 80, 85. ⟩⟩

[23] S. Bandini, C. Gostoli, and G.C. Sarti. Separation efficiency in vacuum membrane distillation. *Journal of Membrane Science*, 73(2–3):217 – 229, 1992. ⟨⟨ Cited on pages 12, 15. ⟩⟩

[24] M. Mulder. Basic priniciples of membrane technology. *Springer*, 1996. ⟨⟨ Cited on page 12. ⟩⟩

[25] F. A. Banat and J. Simandl. Theoretical and experimental study in membrane distillation. *Desalination*, 95(1):39 – 52, 1994. ⟨⟨ Cited on pages 13, 15. ⟩⟩

[26] T. Y. Cath, V. D. Adams, and A. E. Childress. Experimental study of desalination using direct contact membrane distillation: a new approach to flux enhancement. *Journal of Membrane Science*, 228(1):5 – 16, 2004. ⟨⟨ Cited on pages 13, 77, 78. ⟩⟩

[27] M. Khayet, M.P. Godino, and J.I. Mengual. Theoretical and experimental studies on desalination using the sweeping gas membrane distillation method. *Desalination*, 157(1–3):297 – 305, 2003. Desalination and the Environment: Fresh Water for all. ⟨⟨ Cited on page 15. ⟩⟩

[28] L. F. Greenlee, D. F. Lawler, B. D. Freeman, B. Marrot, and P. Moulin. Reverse osmosis desalination: Water sources, technology, and today's challenges. *Water Research*, 43(9):2317 – 2348, 2009. ⟨⟨ Cited on page 16. ⟩⟩

[29] B. R. Bodell. Distillation of of saline water using silicone rubber membrane. *United states patent*, 3,361,645, 1966. ⟨⟨ Cited on page 16. ⟩⟩

[30] P. K. Weyl. Recovery of demineralised water from saaline waters. *United states patent*, 3, 340, 186, 1967. ⟨⟨ Cited on page 16. ⟩⟩

[31] J. Twiddle and T. Weir. Renewable energy resources. *Taylor and Fancis Ltd*, 2nd Edition, 2006. ⟨⟨ Cited on pages 16, 19. ⟩⟩

[32] S.A. Kalogirou, S. Lloyd, J. Ward, and P. Eleftheriou. Design and performance characteristics of a parabolic-trough solar-collector system. *Applied Energy*, 47(4):341 – 354, 1994. ⟨⟨ Cited on page 17. ⟩⟩

[33] M. Gratzel. Photoelectrochemical cells. *Nature*, 414(6861):338–344, 11 2001. ⟨⟨ Cited on page 17. ⟩⟩

[34] D. M. Chapin, C. S. Fuller, and G. L. Pearson. A new silicon pn junction photocell for converting solar radiation into electrical power. *J. Appl. Phys.*, 25(256), 1954. ⟨⟨ Cited on page 17. ⟩⟩

[35] J. Nelson. The physics of solar cells. *Imperial college press*, 2003. ⟨⟨ Cited on page 18. ⟩⟩

[36] A. Goetzberger and C. Hebling. Photovoltaic materials, past, present, future. *Solar Energy Materials and Solar Cells*, 62(1–2):1 – 19, 2000. ⟨⟨ Cited on page 18. ⟩⟩

[37] W. Shockley and H. J. Queisser. Detailed balance limit of efficiency of pn junction solar cells. *Journal of Applied Physics*, 32(3):510–519, 1961. ⟨⟨ Cited on page 18. ⟩⟩

[38] F. Dimroth, M. Grave, P. Beutel, U. Fiedeler, C. Karcher, T. N. D. Tibbits, E. Oliva, G. Siefer, M. Schachtner, A. Wekkeli, A. W. Bett, R. Krause, M. Piccin, N. Blanc, C. Drazek, E. Guiot, B. Ghyselen, T. Salvetat, A. Tauzin, T. Signamarcheix, A. Dobrich, T. Hannappel, and K. Schwarzburg. Wafer bonded four-junction gainp/gaas//gainasp/gainas concentrator solar cells with 44.7 *Progress in Photovoltaics: Research and Applications*, 22(3):277–282, 2014. ⟨⟨ Cited on page 18. ⟩⟩

[39] T.T. Chow. A review on photovoltaic/thermal hybrid solar technology. *Applied Energy*, 87(2):365 – 379, 2010. ⟨⟨ Cited on page 19. ⟩⟩

[40] S. A. Kalogirou. Solar thermal collectors and applications. *Progress in Energy and Combustion Science*, 30(3):231 – 295, 2004. ⟨⟨ Cited on page 19. ⟩⟩

[41] A. Rabl. Comparison of solar concentrators. *Solar Energy*, 18(2):93 – 111, 1976. ⟨⟨ Cited on page 20. ⟩⟩

[42] J. A. Harris and T. G. Lenz. Thermal performance of solar concentrator/cavity receiver systems. *Solar Energy*, 34(2):135 – 142, 1985. ⟨⟨ Cited on page 21. ⟩⟩

[43] A. Kribus, D. Kaftori, G. Mittelman, A. Hirshfeld, Y. Flitsanov, and A. Dayan. A miniature concentrating photovoltaic and thermal system. *Energy Conversion and Management*, 47(20):3582 – 3590, 2006. Heat Transfer in Components and Systems for Sustainable Energy Technologies: Heat-SET 2005, 5–7 April 2005, Grenoble, France. ⟨⟨ Cited on pages 21, 25. ⟩⟩

[44] P. Bhubaneswari, S. Iniyan, and G. Ranko. A review of solar photovoltaic technologies. *Renewable and Sustainable Energy Reviews*, 15(3):1625 – 1636, 2011. ⟨⟨ Cited on pages 21, 143. ⟩⟩

[45] Azur space solar power GMBH. Concentrator triple juction solar cells. 2014. ⟨⟨ Cited on page 22. ⟩⟩

[46] M. Yamaguchi, T. Takamoto, K. Araki, and N. Ekins-Daukes. Multi-junction iii–v solar cells: current status and future potential. *Solar Energy*, 79(1):78 – 85, 2005. ⟨⟨ Cited on page 22. ⟩⟩

[47] B. Y. H. Liu and R. C. Jordan. The interrelationship and characteristic distribution of direct, diffuse and total solar radiation. *Solar Energy*, 4(3):1 – 19, 1960. ⟨⟨ Cited on pages 23, 144. ⟩⟩

[48] G. Vijayakumar, M. Kummert, S. A. Klein, and W. A. Beckman. Analysis of short-term solar radiation data. *Solar Energy*, 79(5):495 – 504, 2005. ⟨⟨ Cited on pages 23, 145. ⟩⟩

[49] J. S. Coventry. Performance of a concentrating photovoltaic/thermal solar collector. *Solar Energy*, 78(2):211 – 222, 2005. {ISES} Solar World Congress 2003. ⟨⟨ Cited on page 25. ⟩⟩

[50] P. Dupeyrat, H. Helmers, S. Fortuin, and K. Kramer. Recent advances in the development and testing of hybrid pv-thermal collectors. *ISES Solar World Congress, At Kassel, Germany*, 2011. ⟨⟨ Cited on page 25. ⟩⟩

[51] A. Cipollina and G. Micale. Coupling sustainable energy with membrane distillation processes for seawater desalination, proceedings of the 1st international nuclear and renewable energy conference. *Proceedings of the 1st International Nuclear and Renewable Energy Conference (INREC10)*, Amman (Jordan), 21-24 March, 2010. ⟨⟨ Cited on page 26. ⟩⟩

[52] C.T. Kiranoudis, N.G. Voros, and Z.B. Maroulis. Wind energy exploitation for reverse osmosis desalination plants. *Desalination*, 109(2):195 – 209, 1997. ⟨⟨ Cited on page 26. ⟩⟩

[53] E. Tzen and R. Morris. Renewable energy sources for desalination. *Solar Energy*, 75(5):375 – 379, 2003. Solar Desalination. ⟨⟨ Cited on page 26. ⟩⟩

[54] G.E Ahmad and J Schmid. Feasibility study of brackish water desalination in the egyptian deserts and rural regions using {PV} systems. *Energy Conversion and Management*, 43(18):2641 – 2649, 2002. ⟨⟨ Cited on page 26. ⟩⟩

[55] A. Joyce, D. Loureiro, C. Rodrigues, and S. Castro. Small reverse osmosis units using {PV} systems for water purification in rural places. *Desalination*, 137(1–3):39 – 44, 2001. ⟨⟨ Cited on page 26. ⟩⟩

[56] D. Herold and A. Neskakis. A small pv-driven reverse osmosis desalination plant on the island of gran canaria. *Desalination*, 137(1–3):285 – 292, 2001. ⟨⟨ Cited on page 26. ⟩⟩

[57] W. Gocht, A. Sommerfeld, R. Rautenbach, Th. Melin, L. Eilers, A. Neskakis, D. Herold, V. Horstmann, M. Kabariti, and A. Muhaidat. Decentralized desalination of brackish water by a directly coupled reverse-osmosis-photovoltaic-system - a pilot plant study in jordan. *Renewable Energy*, 14(1–4):287 – 292, 1998.

6th Arab International Solar Energy Conference: Bringing Solar Energy into the Daylight. ⟨⟨ Cited on page 26. ⟩⟩

[58] J. Koschikowski, M. Wieghaus, and M. Rommel. Solar thermal-driven desalination plants based on membrane distillation. *Desalination*, 156(1–3):295 – 304, 2003. Joint EDS, {WSTA} and {IWA} conference on Desalination and the Environment Fresh Water for All {UN} International Year of Fresh Water 2003. ⟨⟨ Cited on pages 28, 29. ⟩⟩

[59] Z. Ding, L. Liu, M. S. El-Bourawi, and R. Ma. Analysis of a solar-powered membrane distillation system. *Desalination*, 172(1):27 – 40, 2005. ⟨⟨ Cited on page 28. ⟩⟩

[60] J. Koschikowski, M. Wieghaus, M. Rommel, V. Subiela Ortin, B. Peñate-Suarez, and J. Rosa Betancort Rodríguez. Experimental investigations on solar driven stand-alone membrane distillation systems for remote areas. *Desalination*, 248(1–3):125 – 131, 2009. ⟨⟨ Cited on pages 29, 30. ⟩⟩

[61] J.I. Calvo, A. Hernandez, G. Caruana, and L. Martinez. Pore size distributions in microporous membranes: I. surface study of track-etched filters by image analysis. *Journal of Colloid and Interface Science*, 175(1):138 – 150, 1995. ⟨⟨ Cited on page 33. ⟩⟩

[62] R. B. Saffarini, B. Mansoor, R. Thomas, and H. A. Arafat. Effect of temperature-dependent microstructure evolution on pore wetting in {PTFE} membranes under membrane distillation conditions. *Journal of Membrane Science*, 429(0):282 – 294, 2013. ⟨⟨ Cited on pages 33, 109, 111, 129. ⟩⟩

[63] M. G. Di Sparti. Sviluppo di un'unita' di distillazione a membrana con geometria piana per la dissalazione di acqua di mare. *Universita degli Studi di Palermo Facolta di Ingegneria Corso di Studi in Ingegneria Chimica*, 2010. ⟨⟨ Cited on page 40. ⟩⟩

[64] J. I. Goldstein, D. E. Newbury, P. Echlin, D. C. Joy, C. Fiori, and E. Lifshin. Scanning electron microscopy and x-ray microanalysis. a text for biologists, material scientists and geologists. *kluwer academic*, 1981. ⟨⟨ Cited on page 45. ⟩⟩

[65] R. J. Moffet. Describing the uncertainties in experimental results. *Experimental fluid science*, 1(3-17), 1988. ⟨⟨ Cited on pages 51, 63. ⟩⟩

[66] H. W. Coleman and W. G. Steel. Engineering aplication of experimental uncertainty analysis. *AIAAA Journal*, 33(10):1888–1896, 1995. ⟨⟨ Cited on page 51. ⟩⟩

[67] ASME Journal of Heat Transfer Policy. Policy on reporting uncertainties in experimental measurements and result. ⟨⟨ Cited on page 52. ⟩⟩

[68] K. F. Riley, M. P. Hobson, and S. J. Bence. Mathimatical methods for physics and engineering. *Cambridge press*, 2002. ⟨⟨ Cited on page 52. ⟩⟩

[69] S. J. Kline and F. A. McClintock. Describing uncertainties in single sample experiments. *Mech. Eng.*, 3-8, 1953. ⟨⟨ Cited on page 52. ⟩⟩

[70] R. L. Miller, W. L. Bradford, and N. E. Peters. Specific conductance; theoretical considerations and application to analytical quality control. *United stated geological survey, water supply*, 1988. ⟨⟨ Cited on page 54. ⟩⟩

[71] R. D. Down and J. H. Lehr. Environmental instrumentation and analysis handbook. *Wiley-Interscience.*, 2005. ⟨⟨ Cited on page 55. ⟩⟩

[72] M. Hayashi. Temperature-electrical conductivity relation of water for environmental monitoring and geophysical data inversion. *Environmental Monitoring and Assessment*, Volume 96(Issue 1-3):pp 119–128, August 2004. ⟨⟨ Cited on page 55. ⟩⟩

[73] J. Bendat and A. Piersol. Random data: Analysis and measurement procedures. *Wiley-Interscience.*, 1971. ⟨⟨ Cited on pages 61, 62. ⟩⟩

[74] J. Phattaranawik, R. Jiraratananon, and A. G. Fane. Heat transport and membrane distillation coefficients in direct contact membrane distillation. *Journal of Membrane Science*, 212(1–2):177 – 193, 2003. ⟨⟨ Cited on page 69. ⟩⟩

[75] J.I. Mengual, M. Khayet, and M.P. Godino. Heat and mass transfer in vacuum membrane distillation. *International Journal of Heat and Mass Transfer*, 47(4):865 – 875, 2004. ⟨⟨ Cited on page 69. ⟩⟩

[76] M. Khayet and T. Matsuura. Membrane distillation: Principles and applications. *Elsevier*, chapter 15:437, 2011. ⟨⟨ Cited on page 73. ⟩⟩

[77] L. Martinez-Diez and M. I. Vazquez-Gonzalez. Temperature polarization in mass transport through hydrophobic porous membranes. *AIChE Journal*, 42(7):1844–1852, 1996. ⟨⟨ Cited on page 74. ⟩⟩

[78] C. M. Guijt, I. G. Rácz, T. Reith, and A. de Haan. Determination of membrane properties for use in the modelling of a membrane distillation module. *Desalination*, 132(1–3):255 – 261, 2000. Membranes in Drinking and Industrial Water Production. ⟨⟨ Cited on page 77. ⟩⟩

[79] J. M. Coulson and J.F. Richardson. Chemical engineering design. *Butterworth-Heineman ltd*, 6, 1996. ⟨⟨ Cited on page 82. ⟩⟩

[80] Sharaf Al-Sharif, Mohammed Albeirutty, Andrea Cipollina, and Giorgio Micale. Modelling flow and heat transfer in spacer-filled membrane distillation channels using open source {CFD} code. *Desalination*, 311(0):103 – 112, 2013. ⟨⟨ Cited on page 85. ⟩⟩

[81] M. Shakaib, S.M.F. Hasani, Iqbal Ahmed, and Rosli M. Yunus. A {CFD} study on the effect of spacer orientation on temperature polarization in membrane distillation modules. *Desalination*, 284(0):332 – 340, 2012. ⟨⟨ Cited on page 85. ⟩⟩

[82] Xing Yang, Hui Yu, Rong Wang, and Anthony G. Fane. Analysis of the effect of turbulence promoters in hollow fiber membrane distillation modules by

computational fluid dynamic (cfd) simulations. *Journal of Membrane Science*, 415–416(0):758 – 769, 2012. ⟨⟨ Cited on page 85. ⟩⟩

[83] P. Pitò, A. Cipollina, G. Micale, and M. Ciofalo. A novel tlc based technique for temperature field investigation in md channel. *Proceedings of the International Workshop on Membrane Distillation and Related Technologies*, pages 9–12, 2011. ⟨⟨ Cited on page 85. ⟩⟩

[84] A. Tamburini, P. Pitò, A. Cipollina, G. Micale, and M. Ciofalo. A thermochromic liquid crystals image analysis technique to investigate temperature polarization in spacer-filled channels for membrane distillation. *Journal of Membrane Science*, 447(0):260 – 273, 2013. ⟨⟨ Cited on page 85. ⟩⟩

[85] C. A. Schneider, W. S. Rasband, and K. W. Eliceiri. Nih image to imagej: 25 years of image analysis. *Nature Methods*, 9(7):671–675, 2012. ⟨⟨ Cited on page 89. ⟩⟩

[86] G. Schock and A Miguel. Mass transfer and pressure loss in spiral wound modules. *Desalination*, 64(339-352), 1987. ⟨⟨ Cited on page 90. ⟩⟩

[87] A. Hernández, J.I. Calvo, P. Prádanos, L. Palacio, M.L. Rodríguez, and J.A. de Saja. Surface structure of microporous membranes by computerized sem image analysis applied to anopore filters. *Journal of Membrane Science*, 137(1-2):89–97, 1997. ⟨⟨ Cited on page 94. ⟩⟩

[88] J. A. Brydson. Plastics materials. *Butterworth-Heineman ltd*, Fifth edition:344, 1989. ⟨⟨ Cited on page 98. ⟩⟩

[89] I. Engeln, R. Hengl, and G. Hinrichsen. Thermal expansion and youngs modulus of uniaxially drawn ptfe in the temperature range 100 to 400 k. *Colloid and polymer science*, 262(780-787), 1984. ⟨⟨ Cited on page 98. ⟩⟩

[90] J. Blumm, A. Lindemann, M. Meyer, and C. Strasser. Characterization of ptfe using advance thermal analysis techniques. *International Journal of thermophysics*, 31(1919-1927), 2008. ⟨⟨ Cited on pages 98, 115. ⟩⟩

[91] R. Kirby. Thermal expansion of polytetrafluoroethylene (teflon) from -190 to 300 celsius. *Journal of research of the national bureau of standards*, 57(91), 1956. ⟨⟨ Cited on pages 98, 99. ⟩⟩

[92] M.C. García-Payo, M.A. Izquierdo-Gil, and C. Fernández-Pineda. Wetting study of hydrophobic membranes via liquid entry pressure measurements with aqueous alcohol solutions. *Journal of Colloid and Interface Science*, 230(2):420 – 431, 2000. ⟨⟨ Cited on page 110. ⟩⟩

[93] K. Schneider, W. Hölz, R. Wollbeck, and S. Ripperger. Membranes and modules for transmembrane distillation. *Journal of Membrane Science*, 39(1):25 – 42, 1988. ⟨⟨ Cited on page 110. ⟩⟩

[94] Y. Cengel. Heat tranfer: A practical apporach. *McGraw-Hill*, Chapter 4(page 218-220), 2003. ⟨⟨ Cited on pages 111, 112. ⟩⟩

[95] DuPont Fluoroproducts. Teflon ptfe properties handbook. ⟨⟨ Cited on page 115. ⟩⟩

[96] M. Clark. Transport modelling for environmental engineers and scientists. *Wiley son*, 2nd edition, 2012. ⟨⟨ Cited on page 127. ⟩⟩

[97] E. Guillen-Burrieza, J. Blanco, G. Zaragoza, D. Alarcan, P. Palenzuela, M. Ibarra, and W. Gernjak. Experimental analysis of an air gap membrane distillation solar desalination pilot system. *Journal of Membrane Science*, 379(12):386 – 396, 2011. ⟨⟨ Cited on page 128. ⟩⟩

[98] E. Guillen-Burrieza, R. Thomas, B. Mansoor, D. Johnson, N. Hilal, and H. Arafat. Effect of dry-out on the fouling of {PVDF} and {PTFE} membranes under conditions simulating intermittent seawater membrane distillation (swmd). *Journal of Membrane Science*, 438(0):126 – 139, 2013. ⟨⟨ Cited on page 128. ⟩⟩